



Review article

High entropy alloys – Tunability of deformation mechanisms through integration of compositional and microstructural domains



Rajiv S. Mishra*, Ravi Sankar Haridas, Priyanshi Agrawal

Advanced Materials and Manufacturing Processes Institute, Department of Materials Science and Engineering, University of North Texas, Denton, TX, 76207, USA

ARTICLE INFO

Keywords:

High entropy alloys
Deformation induced twinning
Deformation induced transformation
Mechanical behavior
Hierarchical micromechanisms
High enthalpy states

ABSTRACT

The paradigm shift of alloying approach that led to high entropy alloys (HEAs) is now well established. Although the initial years were dominated by equiatomic approach, recent years have seen expansion in non-equiatomic compositional space that can be termed as complex concentrated alloys (CCAs). These HEAs/CCAs provide opportunities for tunable performance by manipulating deformation mechanisms. Understanding has advanced to the point that certain aspects of core effects (entropy of mixing, lattice distortion, sluggish diffusion, and cocktail effect) can be critically examined. In addition, new aspects of metastability engineering and emergence of a wide range of processing strategies has put this field on an exponential growth path. In this review, we categorize the compositional and microstructural approaches that exhibit potential for a combination of shear induced phase transformation and twinning, thereby expanding beyond the slip based mechanisms. The emerging HEAs give greater flexibility for tailoring transformation-induced plasticity (TRIP) and twinning-induced plasticity (TWIP), which have guided design of next-generation steels over the last 20 years to a new level. For TRIP HEAs, the ductility can be extended to as high as 50% while maintaining a strength exceeding 1 GPa. On the other hand, hierarchical microstructural engineering in $\text{Al}_x\text{CoCrFeNi}$ alloys can lead to over 2 GPa strength and >10% ductility. Observations of evolving c/a ratio in HCP phase of certain HEAs hint at possibility of new micromechanisms. While crack tip twin-bridging has been shown as a key mechanism to extend the toughness, concurrent phase transformation at the crack tip has been shown to push the fatigue endurance limit. Tunability of deformation mechanisms in HEAs is unprecedented as compared to the conventional metallic materials, particularly in compositions that exhibit shear induced transformation. The opportunities can be further enhanced by integrating the compositional and microstructure domains, and these aspects are highlighted in this review. The microstructural tailoring can take advantage of high enthalpy states in metastable HEAs with low stacking fault energy values of $< 40 \text{ mJ m}^{-2}$. The range of microstructural engineering in HEAs include, heterogeneous grain structure, duplex and triplex microstructures with intermetallic phases, twinning engineered microstructure, coherent boundary engineered microstructure, and dual-phase and triple-phase microstructure with solid solution phases.

1. Introduction

Alloying is the foundation of metallic materials for engineering structural applications. The progression of alloying from Bronze Age (3300–1200 BCE) to alloys in twentieth century can be described as linear. The very first alloys were based on experiential observations that mixing two elements results in improvement of properties. Obviously, the current processing-microstructure-properties framework was not established till well into the twentieth century and the dislocation theory was not developed till 1934! The classic evolution of alloying

proceeded within the framework of a matrix and the alloying elements. This solvent-solute paradigm provided the context for all alloy development in the twentieth century. As the metallurgical field matured, the combination of analytical tools and metal science resulted in exceptional structural alloys, most noteworthy among which are superalloys and ultrahigh strength steels. The number of alloying elements in steels and nickel-based superalloys can be as high as ten elements. The number of alloying elements in an alloy rivaled ancient alloys in Indian subcontinent which were used among other things for statues. Two of these ancient alloys were literally made of five elements (mentioned in

* Corresponding author.

E-mail address: Rajiv.Mishra@unt.edu (R.S. Mishra).

Sanskrit as *Panch-dhatu*) and eight elements (mentioned in Sanskrit as *Ashta-dhatu*). The *Ashta-dhatu* were made of gold, silver, copper, lead, zinc, tin, iron and antimony or mercury although the chemistry is not well documented. There are even claims that such alloys were made with elements in equal proportion! Note that most of these elements have low melting temperatures.

The current advent of high entropy alloys (HEA) or alloys with multi-principal elements started with two parallel works by Yeh et al. [1] and Cantor et al. [2]. Just in slightly over 15 years from these initial publications, there are now thousands of publications on synthesis and properties of HEAs. The classic alloying framework established by Hume-Rothery rules [3,4] was completely upended by the new equiatomic alloying approach. Although the initial years were dominated by equiatomic approach, recent years have seen expansion in non-equiatomic compositional space that can be termed as complex concentrated alloys (CCAs). A number of review papers have highlighted the extraordinary opening of alloying space with the new HEA approach [5–15]. A few of those reviews, particularly the recent ones, have focused on the mechanical behavior of the HEAs and CCAs. In their extensive review, Zhang et al. [6] have covered wide range of aspects of HEAs including thermodynamics, alloy preparation, mechanical properties, and deformation mechanisms. Tsai and Yeh [7] have briefed about the phase evolution and mechanical properties in certain common HEA systems. George et al. [14] focused on activation of different deformation mechanisms and their influence on the mechanical properties of HEAs. Li et al. [10] gave a dedicated review on mechanical properties and deformation mechanisms of FCC based HEAs. Sathiayamoorthi and Kim [13] discussed the prospect of creating heterogeneous microstructures in HEAs to overcome strength-ductility trade-off. In this review, we focus on ***the tunability of the deformation mechanisms by integration of compositional and microstructural domains***. In particular, the attempt would be to cast the historical arguments and set a context for mechanism driven exploration. In some ways, it is interesting to cast this discussion as ***THEN*** and ***NOW***. The ***NOW*** then pivots into the ***FUTURE***. In this short review, we have not been able to list all the contributions from various researchers, and we mean no slight and hope the readers will consider the illustrative example-based approach as a means to promote further discussion and exploration. Because of the higher familiarity with our own research in various directions in the last five years, there is an apparent bias to draw the figures from the publications of Mishra and co-workers. All attempts have been made to not let this affect the overall context framing and discussion. So, let us begin with the context setting.

Context #1 – Solid solution in a multi-principal element alloy: The classic framing of the HEAs by Yeh et al. [5] about the role of high entropy stabilizing the solid solution matrix. This is without any doubt a very fundamental alloy physics argument. For this review on tunability of deformation mechanisms, the question relates to uniqueness of deformation mechanisms. Are the “four core effects” demonstrable and quantifiable? Which experimental approaches can provide clear and critical evaluations of these? What should be the expected magnitude of impact of the core effects on properties?

Context #2 Exceptionally large number of potential alloys: “The vast compositional search space for the HEAs.” In the first ten years of research, this was often a curiosity driven discussion, the extremely large combination of alloys that are possible based on the initial criterion of 5 or more equiatomic alloying elements. This approach framed the answer with large number of elements in the periodic table that can be chosen for alloys with five elements. In many ways, the thought was related to the Context #1 in which the primary concern was existence of a solid solution alloy. But now this discussion has evolved to a more qualified context. Will the HEA be interesting or good from properties perspective?

Context #3 Are HEAs any good: Switch from the scientific euphoria related to discovery of new alloy physics to the “So, what it is good for?” question. In the old cliché, this is where the rubber meets the road. After

more than a decade of investments in HEA research, examples of technological implementations are very limited. So, it is quite natural to ask about how the properties of HEAs stack in comparison to conventional engineering alloys. For structural applications, quite clearly, we are only interested in mechanical properties – subject of this review! This brings us to a simple proposition. In a single-phase solid solution alloy, the strengthening mechanisms are quite limited. This has led to *multi-principal element, multi-phase alloys*. We will compare some of the HEA properties with conventional alloys to address this context.

Context #4 Are the deformation mechanisms unique: Some of the core effects directly suggest that the details of the deformation mechanisms in HEAs are likely to be different from the conventional alloys. Many times the observations are more nuanced than we will like, but it is important to frame this discussion properly for meaningful interpretations. Indeed, there are quite a few examples about the mechanisms being different and this is touched upon in this review at various places. A related question is about our ability to tune these micro-mechanisms with compositional and microstructural design!

This review is an attempt to discuss the mechanical behavior of HEAs to shape some future research directions while providing readers some thoughts on these contexts. It is important to compare and contrast the emerging results with well-established approaches and data for engineering alloys. In this regards, two noteworthy ways are using Ashby property maps to compare properties and Olson’s systems approach for alloy design.

1.1. Olson’s systems approach for alloy design

Olson [16] developed a systems approach that formalized the classic processing-structure-property-performance relationships. This systems approach forms the basis for integrated computational materials engineering (ICME) framework that is very attractive for alloy design. Fig. 1 shows a modified systems approach that includes alloy chemistry column I. Incorporating alloy design explicitly for triggering specific mechanisms makes it very attractive for the relatively nascent field of HEAs. In this particular review, we want to emphasize on alloying element selection to alter the stacking fault energy. The connector lines are convenient ways to establish the cause-effect linkages. The processability is taken care by linking alloy chemistry to process attributes. The microstructural tailoring is achieved by linking processing parameters to microstructural evolution. It is important to keep in mind that the microstructural evolution is ***probabilistic*** in nature while the properties for a given microstructure is ***deterministic***. The final set of connectors link properties to performance desired by the component designers.

To understand the connector lines, let us take an illustrative example. A key emerging area of high entropy alloys that exhibit deformation induced phase transformation. For such alloys, the alloy chemistry is designed to lower stacking fault energy. So, the column I box with “elements for stacking fault energy” is linked with a box in column II. If we are using thermo-mechanical processing step, then the connector line connects these two boxes. The thermo-mechanical processing changes the grain size, dislocation substructure, texture, stacking faults, twins, and interphase interfaces. So, the thermo-mechanical box in columns II get connected to all these six boxes under column III. These microstructural features change a number of mechanical properties in column IV. So, connecting lines from each of the six microstructural feature boxes in column III link to specific properties in column IV. For example, each of these six lines will go from column III to the strength box of column IV. Similar argument links all these microstructural lines from column III to ductility box of column IV, and so on. Finally, the property boxes under column IV get linked to the performance box in column V. For this, the design goals have to be translated into minimum acceptable property values. The connector lines from properties to performance complete the materials system chart for a particular alloy for a particular application.

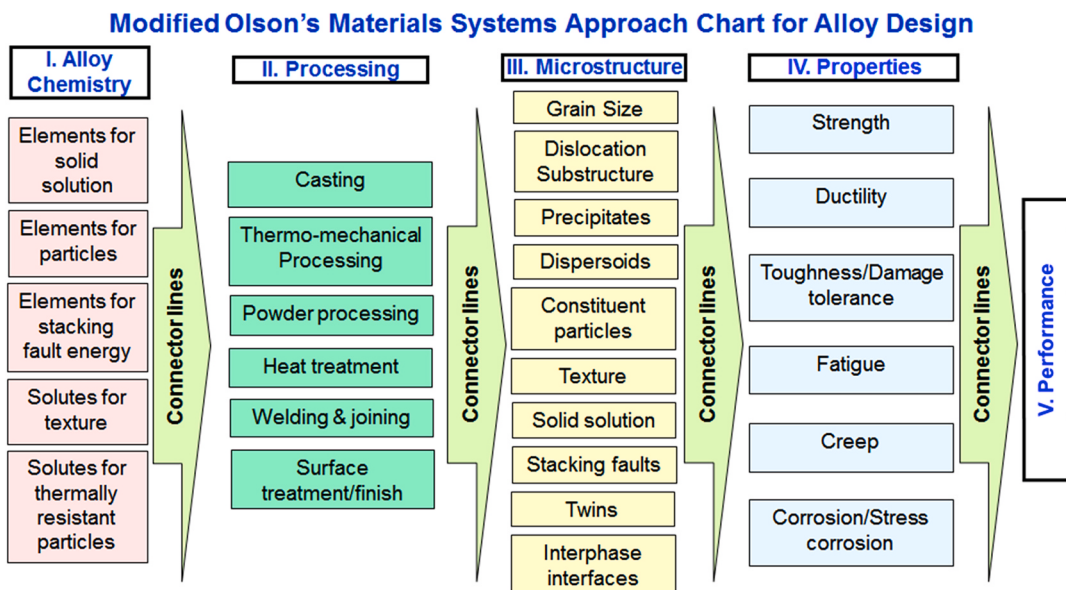


Fig. 1. A modified Olson systems approach to include the alloy chemistry for controlling the microstructural evolution and micromechanisms. This can be a very effective way to incorporate the integrated computational material engineering framework for high entropy alloy design.

1.2. HEA classification

By the definition of HEA, HEAs consist of five or more principal elements and can contain minor elements as well [1,2]. Choice of elements and their enthalpy and entropy of mixing define the phase stability and final microstructure [17]. A more detailed discussion on the factors affecting phase stability and microstructure is provided in a later section

(section 2.1). Classification of HEAs can be based on various categories such as; elements used, crystal structure obtained, phases formed, as well as resulting microstructure. Tsai et al. [7] classified phases in HEAs as terminal phases, intermetallic compounds, and solution phases. Terminal phases are characterized by a single dominating element, intermetallic compounds have stoichiometric composition, and solution phases are based on both simple and complex structures. Additionally,

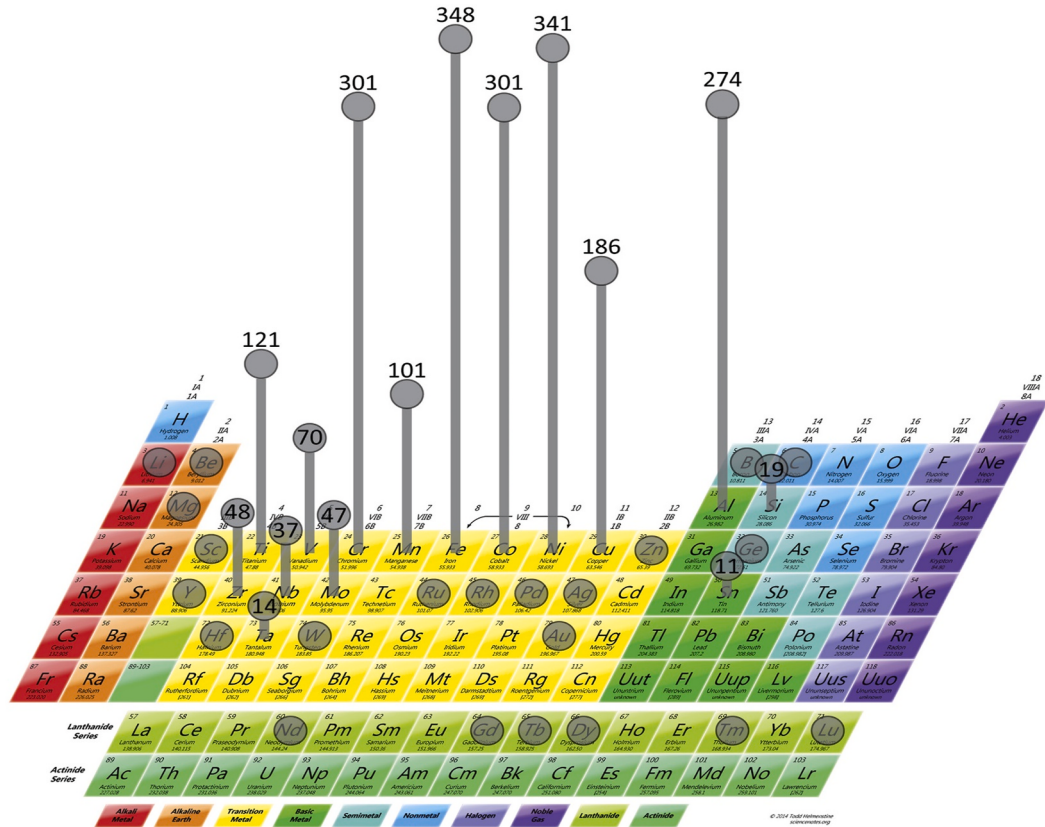


Fig. 2. Statistics of various elements used in multiple HEA compositions reported as per Miracle and Senkov [9].

out of the 118 elements present in the periodic table only 37 elements have been used to generate more than 408 HEA composition reported [9]. Fig. 2 (illustrated in Miracle and Senkov [9]) depicts the statistics of different elements used for manufacturing multiple HEAs reported in literature. Here we summarize different schemes of HEA classification.

1.2.1. Classification based on traditional crystal structure

High entropy effect in HEAs leads to the formation of simple structures, but at times are designed to have multiple phases. Similar to conventional alloys, HEAs are classified on the crystal structure basis as, a) face centered cubic (FCC), b) body centered cubic (BCC), and c) hexagonal closed packing (HCP). FCC is the most explored crystal structure in HEAs so far, while refractory HEAs (RHEAs) are mostly BCC. Only a few HCP HEAs have been explored.

1.2.2. Classification based on constituent elements

Elements used for HEAs include alkali metals, alkali earth metals, transition metals, lanthanides, and non-metals. Al, Co, Cr, Cu, Fe, Mn, Ni, and Ti are the elements used extensively for HEAs. Based on constituent elements, HEAs are classified as, a) 3d transition metals HEAs, b) refractory metal HEAs and, c) other alloy families. Cantor alloy (CoCrFeMnNi) is an example of 3d transition metal HEA. RHEAs based on refractory elemental composition are mainly developed for high temperature applications. Other family of HEAs consist of low density HEAs, complex concentrated brasses and bronzes, and precious metal HEAs.

1.2.3. Classification based on microstructure

Variety of microstructures can be produced in a HEA by altering processing conditions and subsequent heat treatments. Based on microstructure, HEAs can be classified as amorphous, nanocrystalline, single phase, and multi-phase. High entropy bulk metallic glasses (HEBMG) combine the concept of high entropy alloys and bulk metallic glasses (BMG). High configurational entropy in HEAs found beneficial for glass forming tendency and HEBMGs show amorphous microstructure [7], Pd₂₀Pt₂₀Cu₂₀Ni₂₀P₂₀ is an example of HEBMG [18]. Single phase HEAs have conventional structures such as FCC, BCC or HCP; Cantor alloy (CoCrFeMnNi) is an example of single phase FCC HEA.

Multi-phase HEAs are classified as dual phase alloys, precipitation strengthened alloys, precipitation strengthened dual-phase alloys including interstitial containing alloys, and dispersion strengthened alloys [19–21]. Duplex BCC + FCC HEA form for a certain combination of FCC and BCC stabilizing elements, and ordered phases like B2 and L1₂ normally appear along with BCC and FCC phases allowing a rich diversity of microstructural possibilities [22,23]. The concentration of a particular constituent element in an HEA can be varied to produce transition in phases/microstructures. For example, Al_xCoCrCuFeNi is an interesting HEA system, and many studies have explored this HEA system [24,25]. For $x \geq 1.0$ BCC/B2 structure forms, for $0.8 = x \leq 1.0$ BCC/B2+FCC structure forms and $x < 0.8$ results in an FCC structure [26]. It is clear that screening the compositional space for microstructural variants is indeed exceptionally challenging. High throughput compositional screening technique has been developed to accelerate the exploration of desirable composition for HEAs. For example, Shukla et al. [27] studied effect of variation of Cu on the microstructure and mechanical property of transformation induced plasticity (TRIP) HEA Fe₄₀Mn₂₀Co₂₀Cr₁₅Si₅ (CS-HEA). CS-HEA has epsilon HCP (ϵ) phase dominated microstructure but the addition of Cu stabilizes gamma FCC (γ) phase. Fig. 3 shows the microstructural evolution with the addition of Cu. Furthermore, Agrawal et al. [28] studied effect of V addition in the γ stabilized TRIP HEA and observed the nucleation of alpha BCC (α) phase.

1.2.4. Classification based on density

Material selections for applications such as aerospace and automobile industries are dictated by specific material properties (property/density); higher specific properties result in better structural performance. On the basis of the density, HEAs are divided into three categories; lightweight HEAs, medium weight HEAs and heavy weight HEAs.

- Lightweight HEAs – Among conventional alloys, Ti, Al, and Mg based alloys are classified as lightweight alloys. The cut-off density value is 5–5.5 g/cc. Only a few HEAs have been reported in this category [29–34].
- Medium weight HEAs – Most of the literature on HEAs belong to this category of alloys. HEAs based on 3d transition elements fall in this

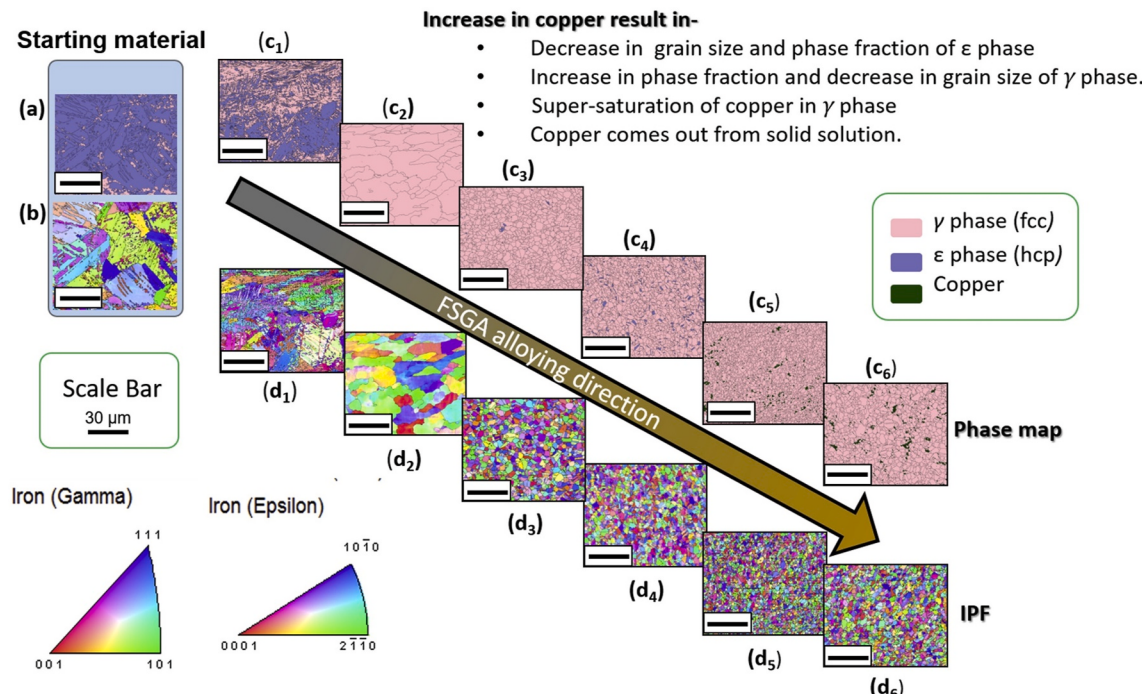


Fig. 3. Microstructure evolution with the addition of Cu in a TRIP CS-HEA (Shukla et al. [27]).

category and CoCrFeMnNi alloy can be treated as medium weight HEAs. The cut off value of density for this category of alloys is 8.5 g/cc.

- Heavy weight HEAs – the refractory element containing HEAs or RHEAs fall in this category.

1.2.5. Classification based on deformation mechanism

Recently, much attention has been given to trigger different deformation mechanisms in HEAs in order to attain better and balanced mechanical properties. For achieving so, stacking fault energy (SFE) of the alloy is varied by controlling the chemical composition. Introduction of deformation twinning has resulted in excellent hardening and ductility in HEAs. Similarly, Li et al. [35] introduced transformation induced plasticity (TRIP) in HEAs via engineering the metastability of the parent austenitic phase. Based on the observed deformation mechanism, HEAs are classified as, (a) Twinning induced plasticity (TWIP) HEAs, and (b) TRIP HEAs. Activation of any of these deformation mechanisms provides concurrent enhancement of strength-toughness-fatigue-ductility [36–40]. Table 1 summarizes the details of different HEAs according to various schemes of classification mentioned above from relevant literature.

2. Core effects in high entropy alloys

Before going into details of mechanical properties and deformation mechanisms in high entropy alloys, for the sake of completeness, an introduction to the core effects pertaining to HEAs is important. HEAs benefits of following core effects.

- High-entropy effect,
- Severe lattice-distortion effect,
- Sluggish-diffusion effect,
- Cocktail effect, and
- Short-range order effect.

Among the available review papers on HEAs [5–15], the concepts of first four core effects were explained in detail, whereas Li et al. [10] explained the possibility and consequences of short-range order that exist among certain principal elements in HEAs. Although existence of all the core effects has not been proven with confidence, a knowledge of the core effects is necessary to understand why this class of alloys is different from classical alloying concepts.

2.1. High-entropy effect

Yeh et al. [1], in their pioneering work, introduced the prefix “high entropy” to multi-component alloy system mixed in equi-molar or near equi-molar proportion, which resulted in a solid solution with rather simple crystal structures defying the possibility of multiple phase formation in such complex composition. They attributed this unprecedented formation of simple solid solution in a multi-component system to high entropy of mixing which exists in multi-component alloy system, thus stabilizing the solid solution phases over the intermetallic compounds. Yeh et al. [1] defined high entropy alloy as a multicomponent system of five or more principal elements mixed in equimolar or near-equimolar proportion. However, they added that proportion of each element can be in the span of 5–35 at.% in order to spread out the alloy design space. Boltzmann’s hypothesis relates the configurational entropy and the mixing complexity as follows [61,62],

$$\Delta S_{conf} = k \ln w, \quad (1)$$

where k is the Boltzmann’s constant and w is the possible ways of mixing the available energy. Eq. (1) can be modified to relate the configuration entropy of solid solution formation from a pool of n elements having X_i mole fraction as follows,

$$\Delta S_{conf} = -R \sum_{i=1}^n X_i \ln X_i, \quad (2)$$

where R is the universal gas constant, 8.314 J/K mol. Eq. (2), when applied to equimolar systems results in the following expression.

$$\Delta S_{conf} = R \ln n \quad (3)$$

Using Eq. (3), for equimolar multicomponent alloy system having elements varying from 3 to 7, ΔS_{conf} are obtained as 1.1R, 1.39R, 1.61R, 1.79R, and 1.95R, respectively. Fig. 4a depicts the variation of $\Delta S_{conf}/R$ with the number of principal elements and indicates the increase in ΔS_{conf} with increase in the number of principal elements. According to Richard’s rule, the entropy change per mole during fusion of a metal at the melting point, $\Delta S_f = \Delta H_f/T_m \sim R$, where ΔH_f is the enthalpy change per mole and T_m is the melting point temperature. In comparison to $\Delta S_f \sim R$ for metals, a three component equimolar alloy has a larger $\Delta S_f = 1.1R$. Apart from the configurational entropy, other contributing factors to entropy such as vibrational, magnetic dipole and electronic randomness will further enhance the entropy of mixing [61]. In a binary system of atoms A and B, possibility of formation of A-B bonds is high when the value of $\Delta H_{mix} < 0$, resulting in intermetallic phases. Yeh et al. [1] pointed out that for strong intermetallics, ΔS_f is comparable to the configurational entropy in multicomponent alloy system having five or more elements. Intermetallics are characterized by low configurational entropies where a stoichiometric composition results in zero configurational entropy. Hence, high mixing entropies in multicomponent alloy system lowers the free energy of mixing (Eq. (4)) by a factor of 1.5 or more, thereby stabilizing the solid solution phases rather than brittle intermetallic phases. Classification of various alloy systems as per Murty et al. [63] is as follows: Low entropy alloys ($\Delta S_f \leq R$); Medium entropy alloys ($R < \Delta S_f \leq 1.5R$) and High entropy alloys ($\Delta S_f > 1.5R$) (Fig. 4b).

$$\Delta G_{mix} = \Delta H_{mix} + T\Delta S_{mix} \quad (4)$$

Although the high entropy effect has been used to explain the stability of solid solution phase, question arises on how often the multi-component systems stabilize into solid solution. Otto et al. [64] carried out a detailed investigation regarding the possibility of formation of solid solution in different HEAs having 5 elements in equimolar proportion so that the configurational entropy change is similar. They considered CoCrFeNiMn (Cantor alloy) as the base and explored the effect of Ti, Mo, V and Cu on the phase stability of the alloy as replacement; all the elements have approximately the same size and electronegativity. Except Cantor alloy, all other alloy systems developed multiple phases, which suggests that high entropy of mixing alone cannot dictate the solid solution formation by counteracting the driving forces for secondary phase formation in multi-component systems (Fig. 5 a-f). They also pointed out that the enthalpy of formation also plays a significant role in minimizing the Gibb’s free energy. An important observation is that, if an HEA has elements which tend to form intermediate phases when alloyed in a binary composition, there are chances of multiple phase formation in multi-component HEAs in which those elements are part of. Through CALPHAD analysis, variation in difference in entropy (S_D), enthalpy (H_D), and Gibb’s free energy (G_D) of formation of binary equilibrium compositions with corresponding energies of ideal solid solution as a function of elemental selection was analyzed (Fig. 5 g-l). Replacing Cr with Mo and V resulted in a reduction in S_D and H_D for all binary compositions except Mo-Mn (Fig. 5g-h). However, G_D values were lower for Mo and V compositions compared to their Cr counterparts (Fig. 5i). Such a reduction in S_D and G_D results in elemental segregation leading to formation of secondary phases in binary composition as opposed to solid solution phase formation in binary compositions of Cantor alloy. Hence, tendency to form secondary phases in binary compositions gets reflected in their quinary equiatomic counterparts as well (Fig. 5a-f). Replacing Ni with Cu resulted in an interesting microstructure with two FCC solid solutions (Fig. 5b).

Table 1

Classification of different HEAs reported in literature as per multiple schemes mention in section 1.

HEA	Processing condition	Crystal structure	Constituent elements	Microstructure	Density (g/cc)	Deformation mechanism	Ref.
Al _{0.3} CoCrFeNi	Bridgeman solidification	FCC	3d transition metal HEAs	Single Crystal (<001>)	–	Slip deformation	[41]
	Casting	FCC + L1 ₂	3d transition metal HEAs	Spherical nanoprecipitates of L1 ₂ in FCC matrix	–	Dislocation-precipitate interaction	[42]
	As cast + aging (700 °C/72 hrs)+water quench	FCC + L1 ₂	3d transition metal HEAs	Platelets of L1 ₂ in FCC matrix	–	Dislocation-precipitate interaction	[42]
	As cast + aging (900 °C/72 hrs)+water quench	FCC + B2+L1 ₂	3d transition metal HEAs	Ordered B2 structure and rod shaped L1 ₂ in FCC matrix	–	Dislocation-precipitate interaction	[42]
Al ₈ Co ₁₇ Cr ₁₇ Cu ₈ Fe ₁₇ Ni ₃₃ (at.%)	Casting	FCC + L1 ₂	3d transition metal HEAs	Discontinuous L1 ₂ precipitates in FCC matrix	–	Dislocation-precipitate interaction	[43]
	As cast+700 °C/5 hrs + air cooling	FCC + L1 ₂ +carbides	3d transition metal HEAs	Discontinuous L1 ₂ precipitates in FCC matrix with grain boundary Cr carbides	–	Dislocation-precipitate interaction	[43]
	As cast+1150 °C/5 hrs + water quenching	FCC + L1 ₂	3d transition metal HEAs	Discontinuous L1 ₂ precipitates (smaller size) in FCC matrix	–	Dislocation-precipitate interaction	[43]
Al _{0.3} CrCuFeNi ₂	Casting	FCC	3d transition metal HEAs	FCC matrix with interdendritic segregation of Cu	–	–	[44]
	Cast + annealed (700 °C for 50 hrs)	FCC + L1 ₂	3d transition metal HEAs	Cuboidal L1 ₂ precipitates in FCC matrix with interdendritic segregation of Cu	–	–	[44]
	Cast + cold rolled (CR) (20%)+solution annealed (SA) (1000 °C/3 hrs)	FCC	3d transition metal HEAs	Equiaxed grain microstructure	–	–	[44]
	Cast + CR (20%)+SA (1000 °C/3 hrs)+IA (700 °C/50 hrs)	FCC + L1 ₂	3d transition metal HEAs	Homogeneously distributed precipitates (0.005 μm ²) in FCC matrix	–	–	[44]
	Cast + CR (20%)+SA (1000 °C/3 hrs)+IA (800 °C/20 hrs)	FCC + L1 ₂	3d transition metal HEAs	Homogeneously distributed precipitates (0.025 μm ²) in FCC matrix	–	–	[44]
	Cast + CR (20%)+SA (1000 °C/3 hrs)+IA (900 °C/20 hrs)	FCC + L1 ₂	3d transition metal HEAs	Homogeneously distributed precipitates (0.19 μm ²) in FCC matrix	–	–	[44]
	Casting	FCC + FCC	3d transition metal HEAs	–	–	–	[45]
Al _{0.5} CoCrCuFeNi	Cast+1000 °C/6 h + CR 84%	FCC + L1 ₂	3d transition metal HEAs	Homogeneously distributed precipitates in FCC matrix	–	–	[46]
	Cast+1000 °C/6 h/ Water quenched + CR 84% + 900 °C/5 h	FCC + FCC	3d transition metal HEAs	FCC phase (grain size 1 μm) and Cu rich FCC phase (grain size 2 μm)	–	–	[47]
	Cast + CR 43%	FCC	3d transition metal HEAs	Dendritic structure	–	Slip deformation	[48]
	Cast + CR 43% + 700 °C/24 hrs	BCC + FCC + L1 ₂	3d transition metal HEAs	Dendritic structure, dendritic region has FCC structure and interdendritic has mixed FCC and BCC structure	–	Slip deformation	[48]
Al _{0.5} CrCuFeNi ₂	Cast + CR 43% + 900 °C/24 hrs	BCC + FCC + L1 ₂	3d transition metal HEAs	Polygrained microstructure with FCC structure, inter/intra-granular BCC particle and needle like L1 ₂ precipitates observed	–	Slip deformation	[48]
	Cast + CR 43% + 1100 °C/24 hrs	FCC + L1 ₂	3d transition metal HEAs	Polygrained microstructure with FCC structure and small amount of ordered FCC phase	–	Slip deformation	[48]
	Casting	BCC + FCC1+FCC2	3d transition metal HEAs	Dendritic microstructure with BCC matrix, interdendritic FCC with high Cu content as compared to intradendritic	–	Slip deformation	[49]
	Cast+960 °C/50 h/a-b-c forged at 950 °C	BCC + FCC1+FCC2+σ	3d transition metal HEAs	Recrystallized BCC structure with two FCC phases and a σ phase	–	Slip deformation	[49]
CoCrFeMnNi	Casting	FCC	3d transition metal HEAs	Single phase FCC microstructure	–	Slip deformation and twining	[50]
	Cast+1200 °C/48 h + CR87% + 800/1 h	FCC	3d transition metal HEAs	Single phase FCC microstructure with annealing twins, grain size - 4.4 μm	–	Slip deformation and twining	[50]
	Cast+1200 °C/48 h + CR87% + 1000/1 h	FCC	3d transition metal HEAs	Single phase FCC microstructure with annealing twins, grain size - 50 μm	–	Slip deformation and twining	[50]
		FCC			–		[50]

(continued on next page)

Table 1 (continued)

HEA	Processing condition	Crystal structure	Constituent elements	Microstructure	Density (g/cc)	Deformation mechanism	Ref.
	Cast+1200 °C/48 h + CR87% + 1150/1 h		3d transition metal HEAs	Single phase FCC microstructure with annealing twins, grain size - 155 µm		Slip deformation and twining	
CoCrFeNi	Cast+1000 °C/24 h + CR-80% + 1100 °C/1 h	FCC	3d transition metal HEAs	Single phase FCC with grain size 60–80 µm	–	Slip deformation	[51]
	Cast+1000 °C/24 h + Hot rolled 92% @1000 °C	FCC	3d transition metal HEAs	Recrystallized microstructure with equiaxed grains of size 11 µm and annealing twins	–	Slip deformation and twining	[52]
Al _{0.4} Hf _{0.6} NbTaTiZr	Cast + HIP (1200 °C/ 207 MPa/2 h) + 1200 °C/24 h	BCC	RHEA	Single phase BCC with equiaxed grains of grain size 140 ± 10 µm	9.05	Slip deformation	[53]
AlMo _{0.5} NbTa _{0.5} TiZr	Cast + HIP (1400 °C/ 207 MPa/2 h) + 1400 °C/24 h	BCC + B2	RHEA	Polycrystalline BCC matrix with 75 ± 5 µm grain size and second phase grain boundary precipitates	7.4	Slip deformation	[53]
NbTiV ₂ Zr	Cast + HIP (1200 °C/ 207 MPa/2 h) + 1200 °C/24 h	BCC1+BCC2+BCC3	RHEA	Three phase microstructure with slightly different composition	6.34	Slip deformation	[54]
NbTiVZr	Cast + HIP (1200 °C/ 207 MPa/2 h) + 1200 °C/24 h	BCC	RHEA	BCC matrix with a grain size of 600 µm	6.52	Slip deformation	[54]
CrNbTiZr	Cast + HIP (1200 °C/ 207 MPa/2 h) + 1200 °C/24 h	BCC + FCC	RHEA	Dual phase microstructure with 65% BCC and 35% FCC phase	6.67	Slip deformation	[54]
CrNbTiVZr	Cast + HIP (1200 °C/ 207 MPa/2 h) + 1200 °C/24 h	BCC + FCC	RHEA	Dual phase microstructure with 39% BCC and 61% FCC phase	6.57	Slip deformation	[54]
NbTaTiV	Casting	BCC	RHEA	Single phase BCC with equiaxed dendrite like grains	9.17	Slip deformation	[55]
MoNbTaW	Casting	BCC	RHEA	Single phase dendritic BCC microstructure with gran size of 200 µm	13.75	Slip deformation	[56]
VMoNbTaW	Casting	BCC	RHEA	Single phase dendritic BCC microstructure with gran size of 80 µm	12.36	Slip deformation	[56]
Al _{0.25} NbTaTiV	Casting	BCC	RHEA	Single phase BCC equiaxed dendritic like grains	8.8	Slip deformation	[55]
Al _{0.5} NbTaTiV	Casting	BCC	RHEA	Single phase BCC equiaxed dendritic like grains	8.46	Slip deformation	[55]
AlNbTaTiV	Casting	BCC	RHEA	Single phase BCC equiaxed dendritic like grains	7.89	Slip deformation	[55]
CrHfNbTiZr	Casting	BCC + Laves	RHEA	Dendritic structure with Cr rich FCC laves phases at the grain boundary	8.24	Slip deformation	[57]
HfNbTiVZr	Casting	BCC	RHEA	Dendritic BCC with HfV2 interdendritic phase with a grain size of 13 µm	8.06	Slip deformation	[57]
Al _{0.3} NbTa _{0.8} Ti _{1.4} V _{0.2} Zr _{1.3}	Cast + HIP (1200 °C/ 207 MPa/2 h) + 1200 °C/24 h	BCC	RHEA	Equiaxed grains with size of 180 µm, grain boundary decorated with bright and dark nanoparticles	7.78	Slip deformation	[58]
Al _{0.5} NbTa _{0.8} Ti _{1.5} V _{0.2} Zr	Cast + HIP (1200 °C/ 207 MPa/2 h) + 1200 °C/24 h	BCC1+BCC2	RHEA	Equiaxed grains with size of 100 µm, fine basket-weave structure of two phases inside the grains	7.42	Slip deformation	[58]
Al _{0.3} NbTaTi _{1.4} Zr _{1.3}	Cast + HIP (1200 °C/ 207 MPa/2 h) + 1200 °C/24 h	BCC1+BCC2	RHEA	Equiaxed grains with size of 200 µm, fine basket-weave structure of two phases inside the grains	8.18	Slip deformation	[58]
AlNb _{1.5} Ta _{0.5} Ti _{1.5} V _{0.2} Zr _{0.5}	Cast + HIP (1400 °C/ 207 MPa/2 h) + 1400 °C/24 h	BCC	RHEA	Equiaxed grains with size of 2000 µm, grain boundary second phase as a thick layer of 220 nm	6.88	Slip deformation	[58]
Fe ₅₀ Mn ₃₀ Co ₁₀ Cr ₁₀ (at.%)	Cast + HR50% + 1200/ 5 h + Friction stir processing (FSP) (350 RPM)	FCC + HCP	3d transition metal HEAs	Dual phase microstructure with 90% FCC and 10% HCP (6.5 µm grains)	–	Transformation induced plasticity	[36]
	Cast + HR50% + 1200/ 5 h + FSP (650 RPM)	FCC + HCP	3d transition metal HEAs	Dual phase microstructure with 92% FCC and 8% HCP (5.2 µm grains)	–	Transformation induced plasticity	[36]
	Cast + HR50% + 1200/ 5 h	FCC + HCP	3d transition metal HEAs	Dual phase microstructure with 13% FCC and 87% HCP (100 µm grains)	–	Transformation induced plasticity	[36]
Fe ₄₀ Mn ₂₀ Co ₁₀ Cr ₁₅ Si ₅ (at. %)	Cast + FSP (RPM = 350)	FCC + HCP	3d transition metal HEAs	Dual phase microstructure with 5% FCC and 95% HCP	–	Transformation induced plasticity	[38]
	Cast + FSP (RPM = 150)	FCC + HCP	3d transition metal HEAs	Dual phase microstructure with 65% FCC and 35% HCP	–	Transformation induced plasticity	[38]
		FCC + HCP			–	(continued on next page)	[38]

Table 1 (continued)

HEA	Processing condition	Crystal structure	Constituent elements	Microstructure	Density (g/cc)	Deformation mechanism	Ref.
Fe ₄₂ Mn ₂₈ Co ₁₀ Cr ₁₅ Si ₅ (at. %)	Cast + FSP (Double pass, RPM = 350 and 150)	FCC + HCP	3d transition metal HEAs	Dual phase microstructure with 31% FCC and 69% HCP	–	Transformation induced plasticity	[59]
	Casting		3d transition metal HEAs	Dual phase microstructure with 94% FCC and 6% HCP (100 µm grains)		Transformation induced plasticity	
	Cast + FSP (Multipass)		3d transition metal HEAs	Dual phase microstructure with 88% FCC and 12% HCP (1.3 µm grains)		Transformation induced plasticity	
Fe ₃₉ Mn ₂₀ Co ₁₀ Cr ₁₅ Si ₅ Al ₁ (at.%)	Casting	FCC + HCP	3d transition metal HEAs	Dual phase microstructure with 10% FCC and 90% HCP (120 µm grains)	–	Transformation and twinning induced plasticity	[60]
	Cast + FSP (double pass)	FCC + HCP	3d transition metal HEAs	Dual phase microstructure with 83% FCC and 17% HCP (0.79 µm grains)	–	Transformation and twinning induced plasticity	[60]

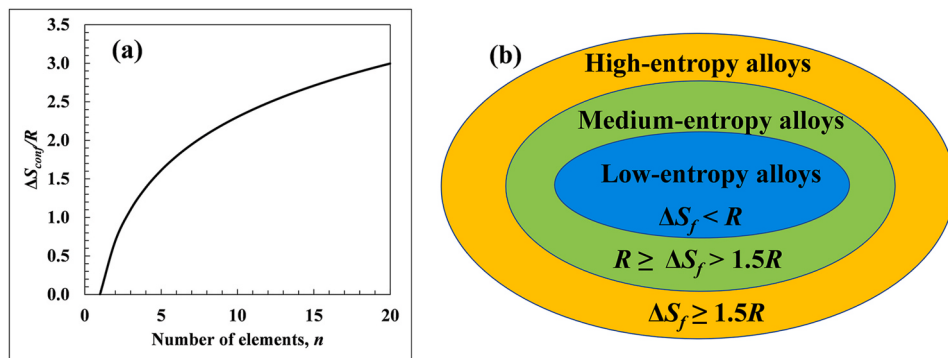


Fig. 4. (a) Variation of configurational entropy (ΔS_f) with respect to number of principal elements in the alloy (n), and (b) division of alloy world according to Murty et al. [63].

Although, addition of Cu resulted in a decrease in S_D in all three binary compositions except Mn-Cu (Fig. 5j-k), G_D values were observed to be positive (Fig. 5l). Addition of Cu did not form any stable intermetallic, Cu got separated from Co, Cr, and Fe resulting in the formation of two FCC solid solutions. Further, they critically emphasized that only those alloys which result in true solid solution can be considered as *high entropy alloys*, whereas all other alloy systems which results in multiple phases should be designated as *multi-component alloys*. However, as we will cover later, this distinction is lost in most discussion. Particular noteworthy is development of multi-phase even in Cantor alloy or Al_xCoCrFeNi alloys with thermomechanical processing and aging [23,65].

2.2. Severe lattice distortion effect

When elements having different atomic radii are mixed together to form a solid solution, it is obvious that the otherwise continuous and smooth lattice in a pure metal gets distorted. Since HEAs comprise of five or more elements in equimolar or near-equimolar proportion, the extent of lattice distortion is severe. Yeh et al. [66] observed a reduction in the peak intensity in XRD pattern when the number of constituent elements is gradually increased in sequence in a CuNiAlCoCrFeSi system (Fig. 6a). In general, similar trend in peak reduction is observed in crystalline materials due to thermal effects at high temperature as well as when subjected to severe plastic deformation. However, at the same temperature and XRD measurement conditions in the absence of severe plastic deformation, the reason for peak reduction is attributed to highly distorted and roughened atomic planes which results in severe X-ray scattering and thus weakening the diffraction signals when reaching the detector. Fig. 6(b-d) illustrate the effect of variation in atomic size of constituent elements, atomic randomness and lattice distortion on X-ray diffractions and peak intensities. In order to quantify the peak intensity

reduction due to severe lattice distortion, Yeh et al. [66] introduced a modification factor in addition to the Debye-Waller temperature factor (M^T) to obtain the combined XRD structure factor as follows,

$$\bar{F}_{h k l}^{T,D} = F_{h k l} \exp(-M^T - M^D) \quad (5)$$

where $F_{h k l}$ is the XRD structure factor on $(h k l)$ lattice plane at absolute temperature and zero lattice distortion, $\bar{F}_{h k l}^{T,D}$ is the structure factor when the effect of temperature and lattice distortion is incorporated, M_T is the thermal vibration correction factor and M_D is the lattice distortion correction factor. Illustration of Eq. (5) is represented in a pictorial format in Fig. 6d. High strength in BCC HEAs [67–69], slower kinetics [1,5,70], higher hardness [63,71], reduction in electrical and thermal conductivities, lesser temperature influence on these properties, and tensile brittleness observed in HEAs is also attributed to severe lattice distortion effect [63,71].

High solid-solution strengthening observed in HEAs can be explained based on severe lattice distortion. CoCrFeMnNi (Cantor alloy) is here considered as the basis for discussion of lattice distortion effect in which the atomic size of the constituent elements is comparable. Addition of Al atom results in higher lattice distortion in Al_xCoCrFeNi alloy system due to larger atomic size of Al [72]. Fig. 7a illustrates the effect of additional elements on lattice distortion from pure Ni to a senary HEA. The basis of solid-solution strengthening in conventional alloys rely on the dislocation interaction near distorted lattice sites occupied by solute atoms; the magnitude of solid-solution strengthening depends of the atomic size mismatch between the matrix and solute, as well as the modulus mismatch. However, in HEAs, due to equimolar or near-equimolar proportion of elements, the matrix-solute concept appears to be invalid. In HEAs, one has to expect lattice strain in each and every unit cell because of atomic size mismatch of constituent elements. Each and

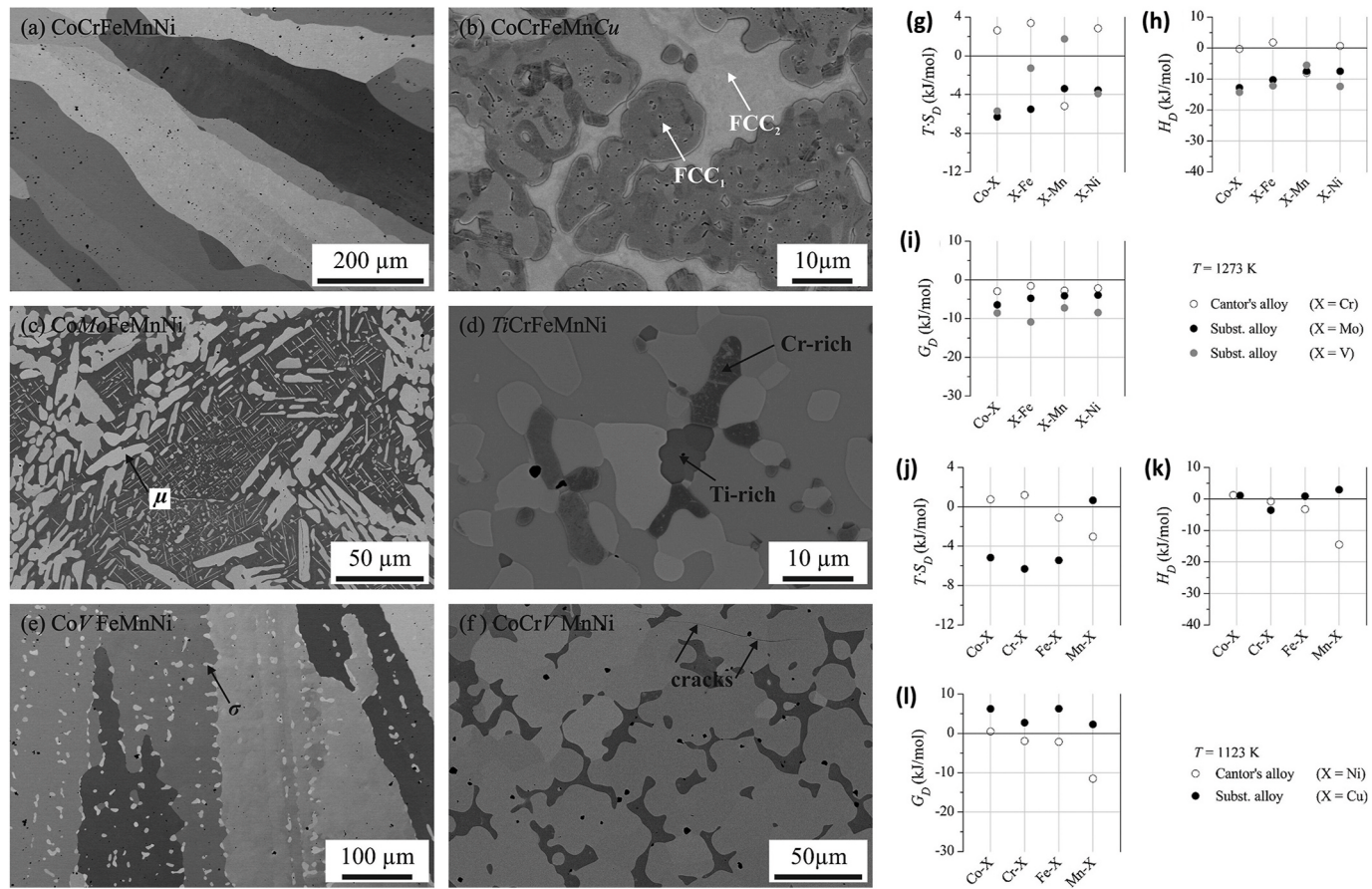


Fig. 5. Backscatter SEM micrographs showing the microstructure of alloys after annealing. (a) CoCrFeNiMn, (b) CoCrFeMnCu, (c) CoMoFeMnNi, (d) TiCrFeMnNi, (e) CoVFeMnNi, (f) CoCrVMnNi, (g–i) changes in deviation in entropy ($T.S_D$), enthalpy (H_D) and Gibb's free energy (G_D) for all binary compositions of Cantor alloy when Cr is replaced with Mo and V, (j–l) changes in deviation in entropy ($T.S_D$), enthalpy (H_D) and Gibb's free energy (G_D) for all binary compositions of Cantor alloy when Ni is replaced with Cu [64].

every bond in the unit cell can be subjected to either elastic tension or compression. This causes hindrance to dislocation motion across the lattice when compared to an ideal lattice. Effect of lattice distortion on dislocation line energy was discussed in detail by Komarasamy et al. [73]; its schematic is shown in Fig. 7(b–e).

Another impact of lattice distortion is its influence on stacking fault energy (SFE). Lattice distortion in HEAs leads to a decrease in activation energy required for dislocation nucleation (Fig. 7h). This further implies that dislocation nucleation is easier and hence results in low SFE. For example, addition of Al in pure Cu resulted in a decrease in SFE [75]. However, the activation volume of dislocation reduces due to roughened atomic planes as a result of lattice distortion. Mishra et al. [74] reported a drastic reduction in activation volume in coarse grained Al_{0.1}CoCrFeNi when compared to other conventional coarse-grained alloys (Fig. 7i). Hence, the swept volume of dislocation reduces for a specific increment in stress. This implies that, although the dislocation nucleation and generation of stacking faults are easier in HEAs, its motion through the distorted lattice is difficult. Addition of Al, which has a higher atomic size, results in more lattice distortion and hence retards the dislocation motion (Fig. 7(f–g)). Experimental and computational evidences of reduction in SFE have been reported in HEAs [51]. Fig. 8(a–b) show the reduction trend of SFE in equiatomic CoCrFeMnNi HEA when compared to pure Ni [51]. Also, SFE of non-equiatomic Cr₂₆Mn₂₀Fe₂₀Co₂₀Ni₁₄ is significantly lower as compared to the equiatomic Cantor alloy, although the non-equiatomic HEA has a lower configurational entropy than the equiatomic HEA. This is an important consideration in further design of HEAs, particularly with major and minor elements to manipulate the lattice distortion.

Potential to engineer SFE in HEAs has further impact on hardening mechanisms such as deformation induced twinning and transformation [76]. Twinning occurs in FCC systems when stacking faults forms on every three consecutive {111} planes whereas martensitic embryo formation occurs when the stacking fault forms in every other {111} plane [77]. Komarasamy et al. [76] have postulated that formation of stacking faults and twins will be energetically favorable due to an increase in energy state of FCC as a result of lattice distortion. This framework to reduce the SFE by increasing the lattice distortion of HEAs/CCAs is shown in Fig. 8c. This can be further extended to HEAs exhibiting transformation during deformation. Galindo-Nava and Rivera-a-Díaz-del-Castillo [77] have analyzed the data for austenitic steels to correlate the transition in mechanism with stacking fault energy. Twinning is observed in alloys for which $SFE < 30 \text{ mJ m}^{-2}$, whereas martensitic transformation is achieved when $SFE < 18 \text{ mJ m}^{-2}$. Lower SFE in HEAs enables the propensity of twinning and transformation. Thus, capability to engineer the SFE by varying the alloying compositions to introduce lattice distortion enables one to design multicomponent alloy system with introduction of deformation induced twinning and transformation resulting in combination of high strength and ductility.

2.3. Sluggish diffusion effect

Diffusion in metals is the process of material transport achieved by local atomic migration from one lattice site to another which is stochastic in nature [78–80]. Additionally, vacancy exchange mechanism of diffusion is governed by the concentration and movement of

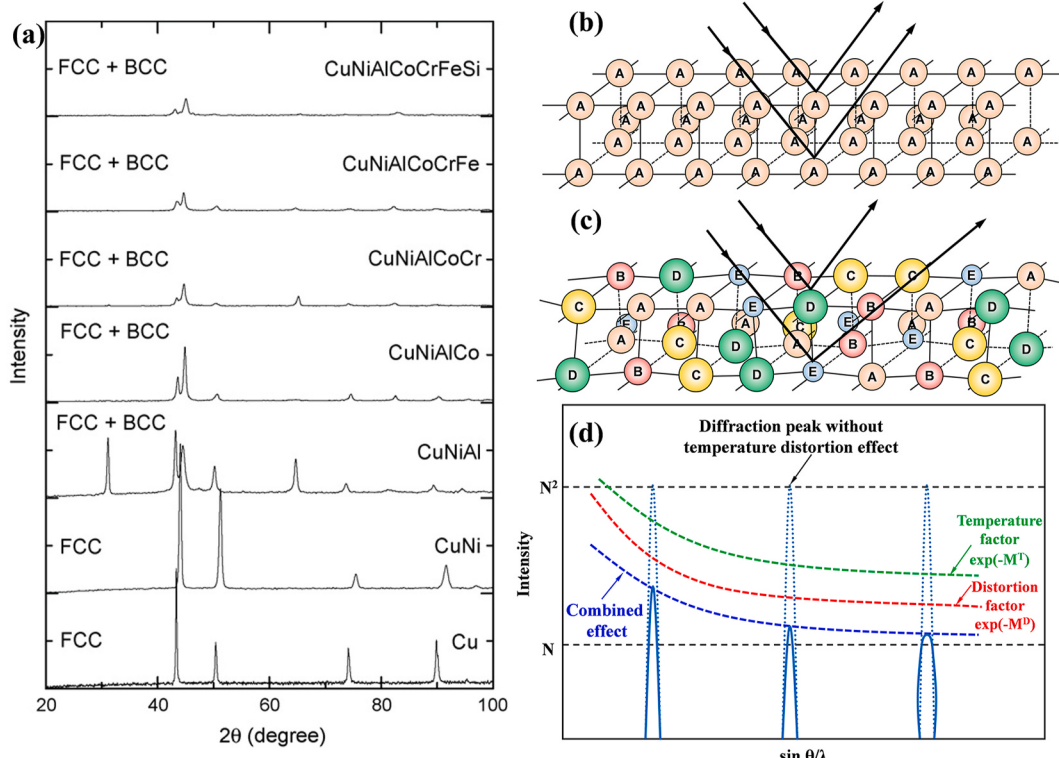


Fig. 6. (a) Reduction in the peak intensities in XRD patterns with sequential increment in elements for Cu–Ni–Al–Co–Fe–Cr–Si alloy, (b) schematic showing Bragg diffraction in a perfect crystal lattice, (c) schematic showing Bragg diffraction in a distorted lattice with multiple elements, and (d) effect of distortion effect over temperature effect in XRD diffraction pattern [66].

vacancies. Tsai et al. [81] reported that the diffusion coefficient of each element in CoCrFeMnNi alloy is lower than that in pure metals (Fig. 9). Also, the diffusion coefficient increases with increase in the number of elements in the matrix. Tsai and Yeh [7] considered two aspects to explain the sluggish diffusion in HEAs. Firstly, the randomness of lattice occupancy of constituent elements results in dissimilar neighborhoods. Hence, the neighboring elements before and after an atomic jump into a proximal vacancy will be different. Additionally, since the atomic sizes are different for each neighboring element, there will be variation in bonding and local lattice site energy. Based on the neighboring element at the new location, the lattice site can be either a low energy site or high energy site. Low energy sites act as a trap for the diffused atom which locks the element at its new location, whereas high energy sites may cause the atom to jump back to its original location. Whichever the case is, a low diffusion rate is the effect. Sluggish diffusion in HEAs is the result of variation in lattice potential energy (LPE) from site to site which depends on the total interaction energy. With the help of a quasi-chemical model, Tsai et al. [81] reported almost 50% higher LPE fluctuation in CoCrFeMn_{0.5}Ni alloy compared to FeCrNi ternary alloy (Fig. 10a). Higher LPE fluctuations results in more sluggish diffusion since the lower energy sites act as traps for atoms and thereby hindering their subsequent migration. Secondly, due to variation in the diffusion rate of each element in HEA, their relative diffusion activity varies. For microstructural activities such as phase transformation and grain growth, a coordinated activity of all elements is needed. However, rate of such phenomena will be dictated by the most inactive element in the composition.

Sluggish diffusion can be explained further with the help of Fig. 10 (b–d). Fig. 10b shows a 2-D arrangement of lattice points in a dilute alloy (2% solute) with two vacancies. Five different ways of vacancy migration is possible as denoted in Fig. 10b; on a special note, exchange 3 dissociates the vacancy from the solute atom, whereas exchange 4 associates the vacancy with the solute atom. When the solute atom

percentage is increased to 18%, the vacancy migration conditions are varied (Fig. 10c). Movement of vacancies to sites A, B, C, and E results in an increase in vacancy–atom bond to 2 whereas other possible vacancy movements does not change the vacancy–atom bonds. Due to variation in vacancy–atom binding energy, the relocation of vacancy to a new location is energetically different. Fig. 10d expands the above concept to a multi-element system. Adjacent lattice points to a vacancy are occupied by different atoms. Difference in intrinsic diffusivity and the vacancy bond energy for each element together with the variation in interaction energy makes the vacancy jump more coordinated than random resulting in a sluggish diffusion in HEAs.

2.4. Cocktail effect

Cocktail effect was first proposed by Ranganathan [82] with a general intuition that a multicomponent alloy system can have synergistic properties of individual components resulting in unexpected properties to the HEA. Yeh [83] described *cocktail effect* as “*the overall effect form composition, structure, and microstructure*” directly influencing the final physical and mechanical properties of the alloy. Lu et al. [84] defined cocktail effect as “*the synergistic effect resulted from mutual interactions among composing elements, which would bring excess quantities to the average values simply predicted by the mixture rule*”. But Tsai et al. [7] emphasized that the above argument cannot always stand true. For example, one expects addition of a lighter alloy such as Al into an alloy system of CuCoCrFeNi would make the alloy soft. However, hardness value increases with increase in Al content partly due to the formation of hard BCC phase and partly due to higher cohesive forces between Al and other constituent elements (Fig. 11a) [1]. Removing Cu from the former alloy system resulted in a reduction in overall hardness, as well as narrowed the dual phase region in Al_xCoCrFeNi HEA (Fig. 11b) [85]. Further, severe lattice distortion also adds to property enhancement. For example, experimentally observed hardness for Cantor alloy and

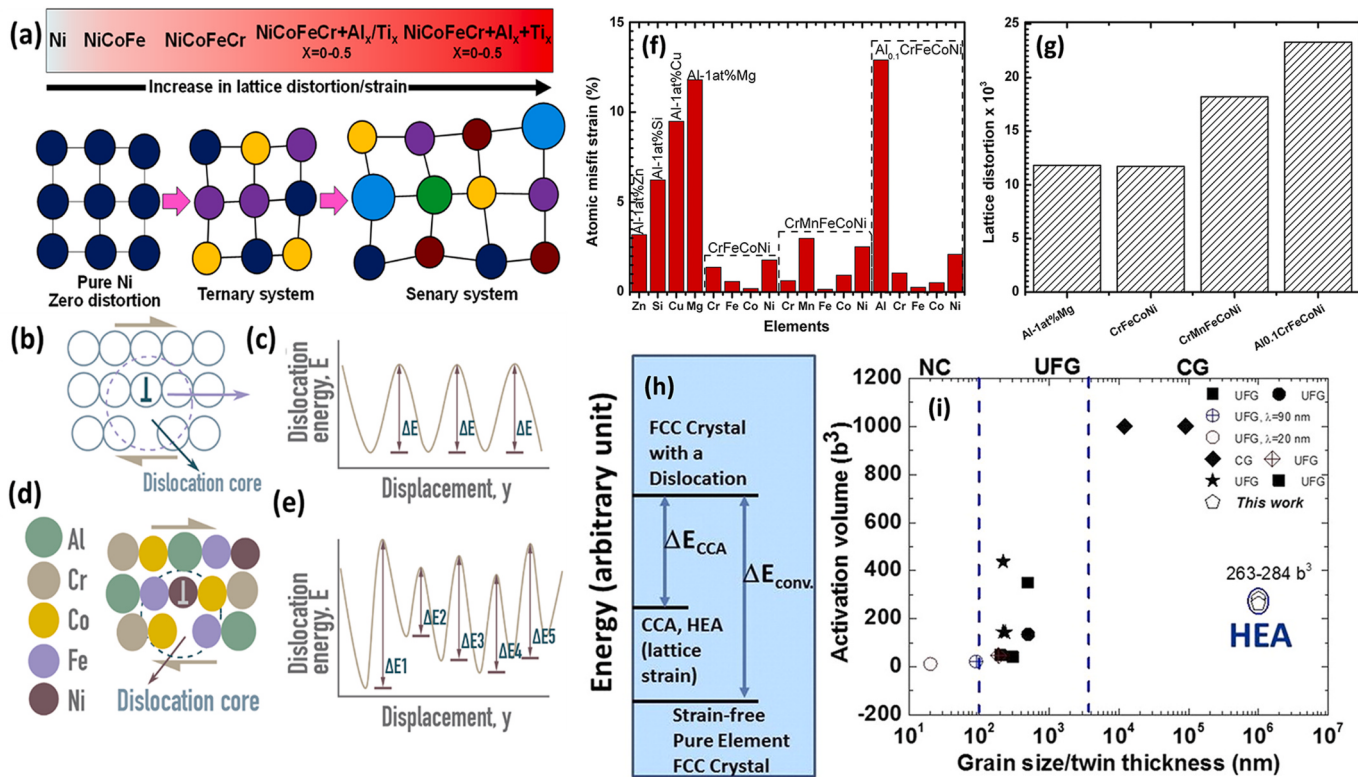


Fig. 7. (a) Schematic of lattice distortion due to addition of multiple elements with different atomic size, (b) atomic arrangement around a dislocation in a pure metal and corresponding dislocation line energy during motion in (c), (d) atomic arrangement around a dislocation in a multicomponent alloy and corresponding energy fluctuation while in motion in (e) [73], (f) atomic misfit strain in conventional single phase FCC binary alloys, CoCrFeNi, CoCrFeNiMn, and Al_{0.1}CoCrFeNi HEAs, (g) increase in lattice distortion due to addition of Al in Al_{0.1}CoCrFeNi HEA compared to other single phase HEAs, (h) schematic showing the energy requirement for dislocation nucleation in HEA compared to conventional alloys, and (i) reduction in activation volume in Al_{0.1}CoCrFeNi HEA when compared to other conventional FCC alloys [74].

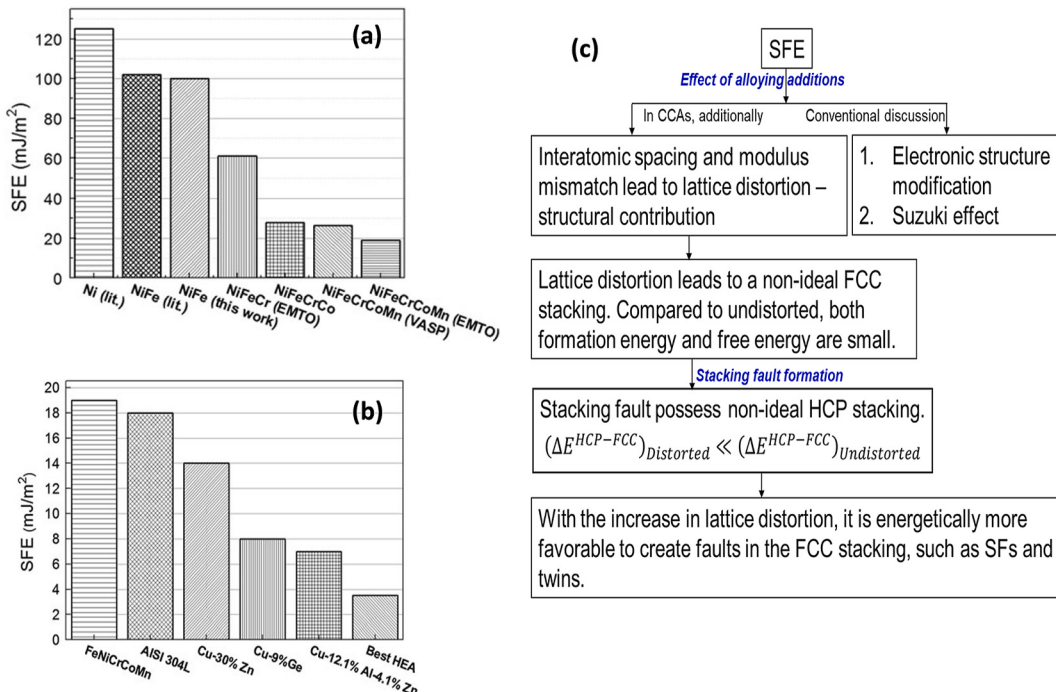


Fig. 8. (a) Stacking-fault energy (SFE) of equimolar FCC metals from pure Ni to CrMnFeCoNi HEA, (b) SFEs of equiatomic CrMnFeCoNi and non-equiatomic Cr₂₆Mn₂₀Fe₂₀Co₂₀Ni₁₄ HEAs, as compared with other low SFE alloys [51], and (c) overall framework for the reduction in SFE via lattice distortion core effect in the case of CCAs [76].

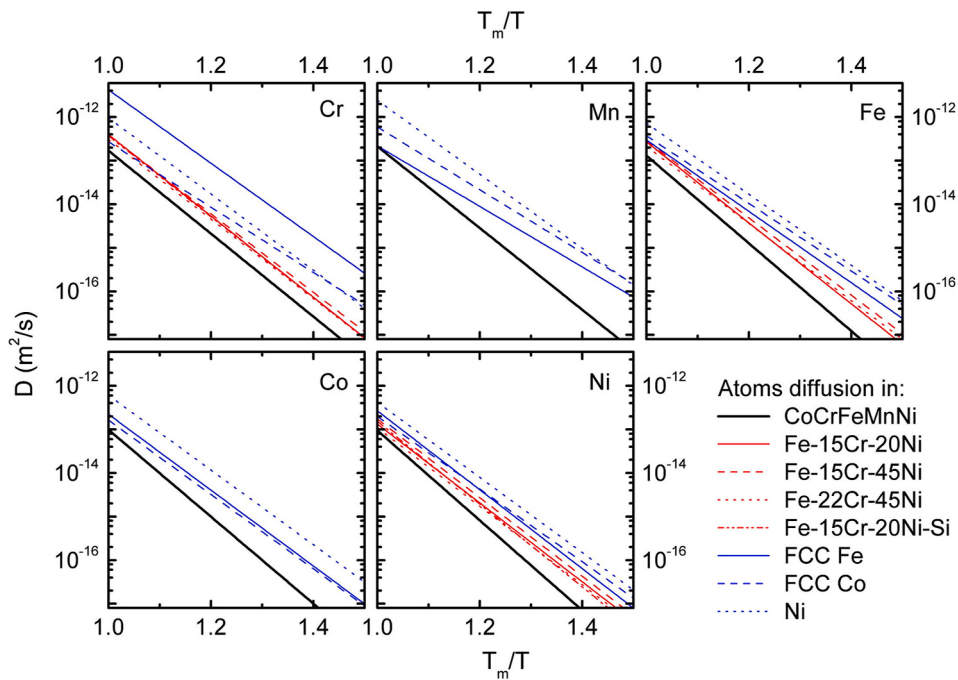


Fig. 9. Reduction in the value of diffusion coefficient for different elements in CoCrFeNiMn HEA when compared to other FCC matrices [81].

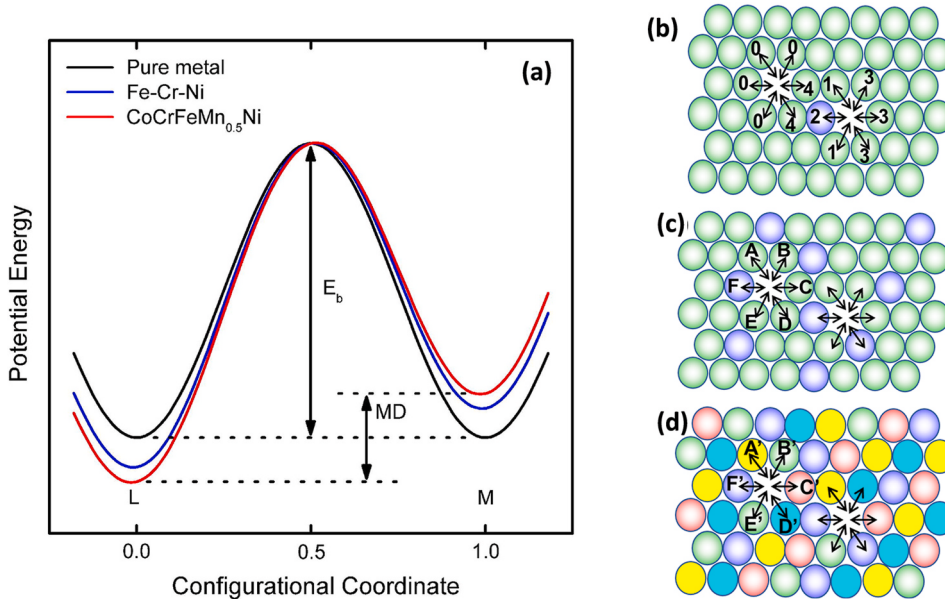


Fig. 10. (a) Higher mean difference in the lattice potential energy (LPE) during Ni atomic migration in HEA compared to other FCC matrices [81], 2D lattice representation of different jump possibilities in (b) dilute alloy having 2% solute, (c) binary alloy having 18% solute, and (d) quinary HEA with 18–20% of each constituent elements (adapted from Ref. [78]).

MoNbTaVW refractory HEA is much higher than the value obtained using rule of mixtures [63]. Additionally, combination of high specific strength, ductility, corrosion property, fatigue, and wear resistance have been reported [63]. In a recent work, Shukla et al. [86] have shown that AlCoCrFeNi_{2.1} eutectic HEA has shown excellent fatigue properties along with good tensile strength after cold rolling and subsequent heat treatment owing to the presence of a hierarchical microstructure and embedded precipitates. In another example, Mishra et al. [87] have illustrated how the stability of γ (f.c.c. phase) and ϵ (h.c.p. phase) in a Fe-Mn-Co-Cr-Si metastable HEA alloy system can be dramatically altered with minor addition of alloying elements such as Cu or Al. The microstructure in Fe₄₀Mn₂₀Co₂₀Cr₁₅Si₅ HEA is ϵ -phase dominant at

ambient temperature, whereas minor addition of Cu in Fe_{38.5}Mn₂₀-Co₂₀Cr₁₅Si₅Cu_{1.5} HEA stabilized the γ -phase at ambient temperature which subsequently deforms by TRIP. Liu et al. [39] have reported excellent fatigue property for this alloy, one of the best reported so far, along with excellent strength and ductility. Nene et al. [88] have reported excellent corrosion resistance for the same HEA. Fe_{38.5}Mn₂₀-Co₂₀Cr₁₅Si₅Cu_{1.5} TRIP HEA thus illustrates how a minor addition of a soft metal like Cu could substantially change the microscopic aspects as well as the physical and mechanical properties of the alloy. This reinforces the strength of combining major and minor alloying elements [74]. In another example illustrating the influence of thermo-mechanical processing pathways on the mechanical

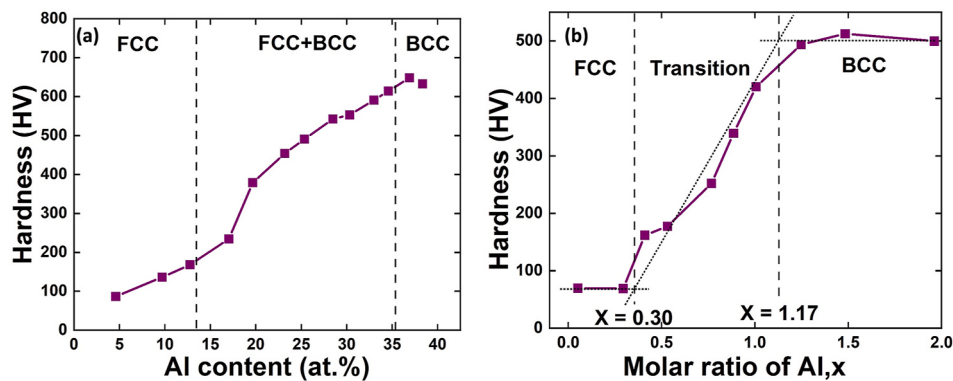


Fig. 11. (a) Variation in hardness and phase as a function of Al content in $\text{Al}_x\text{CoCuCrFeNi}$ HEA [1], and (b) reduction in hardness in Cu-free $\text{Al}_x\text{CoCrFeNi}$ HEA as well as reduction in the span of the transition zone [85].

characteristics of HEA, Gwalani et al. [24] have shown that the tensile yield strength of $\text{Al}_{0.3}\text{CoCrFeNi}$ HEA can be tuned from 160 MPa to as high as 1.8 GPa, an enormous ten-fold increase, which is exceptional in any other alloy system. Thus, possibility of wider exploration of compositional space along with flexibility in selection of compositions enables excellent cocktail effects in HEAs. Cocktail effect points towards non-linear and unexpected property accomplishment in HEAs owing to unusual microstructures and elemental compositions. This concept is more abstract than others, and careful analysis is needed to highlight the synergistic improvement in properties and ways in which the enhancement goes beyond the conventional linear expectation.

2.5. Short-range order effect

As explained before, HEAs are characterized by a single random solid solution with multiple principal elements. Still, questions arise on how regular the random solid solution is stabilized in the entire material. Local fluctuations in chemistry may result in precipitation and segregation of secondary ordered phases in the matrix [26,89–95]. Chemical short range order (CSRO) has significant impact on the mechanical properties of the material. Initial computational studies have proven the possibility of tuning the deformation mechanism via variation in local SRO. Ding et al. [96] has shown with the help of DFT simulations that SFE is tunable from -43 to 30 mJ m^{-2} and from -28 to 66 mJ m^{-2} for intrinsic and extrinsic stacking faults in CoCrNi medium entropy alloy (MEA), respectively, with an increase in the degree of the local chemical order. Experimentally observed value for SFE in CoCrNi MEA based on separation of dislocation partials is $22 \pm 4 \text{ mJ m}^{-2}$ [97]. Computational study on CSRO and experimentally obtained value for SFE in CoCrNi MEA suggest the presence of higher degree of local CSRO. Additionally, variation in local CSRO has direct correlation with the activation energy for FCC to HCP phase transformation which supports the experimental observation of HCP substructure formation in CoCrNi MEA at higher strain levels [98].

Zhang et al. [99] have proved experimentally with the help of neutron total scattering and EXAFS techniques the presence of local SRO where Cr atoms have shown preferential bonding with Co and Ni atoms. Recently, Zhang et al. [100] studied the existence of SRO in CoCrNi HEA using energy filtered TEM imaging and its impact on SFE and mechanical properties of the alloy as a function of thermomechanical processing. Presence of SRO in annealed material justified higher SFE, and yield strength of the material when compared to the water quenched material which lacks any SRO. Studies on the effect of SRO on the mechanical properties and dislocation interaction in HEAs show an emerging trend in the recent past [101–108]. Computational study by Sobieraj et al. [101] in Cr-Ta-V-W system revealed a strong chemical ordering between Cr and V and suggested that reducing concentration of either of the elements could substantially reduce the order-disorder transition

temperature. Reverse Monte-Carlo simulations by Nygard et al. [102] demonstrated the presence of local SRO between Ti and Nb atoms which formed FCC super cells in TiNb alloy. Fernandez-Caballero et al. [104] have also reported strong SRO between Ta–Mo pairs which supported the presence of B2 phase in the BCC based HEA.

3. Strengthening mechanisms in HEAs

As mentioned in Contexts #3 and #4, with the advent of HEAs, the excitement developed that the new concepts in HEAs will lead to impressive mechanical properties. Ashby's materials selection for mechanical design approach highlights five primary design considerations, namely, stiffness-limiting, strength-limiting, toughness-limiting, fatigue-limiting, and creep-limiting designs. Among these, other than the stiffness-limiting design, all others rely on strengthening mechanisms. Indeed, HEAs have been reported to show superior mechanical properties; high strength-ductility combination [37,38,40,59], ultra-high fracture toughness [109], and excellent fatigue resistance [39,110]. Strengthening in any metal or alloy is related to the resistance to dislocation motion and any barrier that impedes the motion of dislocations in a material provides strengthening to it. Mechanisms of strengthening are generally dependent on the crystal structure and microstructure of the material. Best known mechanisms of strengthening are; solid solution, dislocation density, grain size, precipitation, dispersion, order, twinning, and transformation. The strengthening mechanisms that are available in a single phase FCC or BCC HEAs are solid solution strengthening and grain size strengthening. Chemical ordering, crystallographic structures, and interstitial solutes affect the solid solution strengthening mechanism. Decreasing the stacking fault energy below a critical value triggers twinning and transformation, leading to additional interfacial strengthening. In this section, we discuss different strengthening mechanisms in HEAs.

3.1. Solid solution strengthening

Addition of solute atoms in a solvent matrix enhances the mechanical response of the matrix. As HEAs contain 5 or more principal alloying elements, this is one of the primary strengthening mechanism in HEAs. Depending upon the size of the solute atoms in comparison to the solvent atoms, solute atoms can either occupy substitutional sites or interstitial sites. If the size of the solute atoms is roughly similar to that of solvent, then the solute atoms occupy lattice sites of the solvent and it is called substitutional solid solution. Whereas if the size of the solute atoms is much smaller than the solvent atoms, they occupy interstitial sites and it is called interstitial solid solution. Strengthening in any alloy due to substitutional solute atoms is different from strengthening due to interstitial ones. The distortion field created by substitutional solutes is spherical which provides relative strengthening (strengthening per unit

concentration) of about $G/10$, where G is the shear modulus [111]. However the distortion field created by interstitial solute atoms is non spherical and it provides relative strengthening of about $3G$ [111]. Carbon, hydrogen, nitrogen, oxygen, and boron are common interstitial solute atoms. The atomic size of the elements of 3d transition metals HEAs (for example, CoCrFeMnNi) is comparable and mostly form substitutional solid solution.

To strengthen a material, solute atoms should act as a barrier for dislocation motion; in order to do so, solute atoms interact with the dislocations by the following micromechanisms:

- Elastic interaction – this interaction between the solute atom and dislocation is directly related to the misfit of the solute atoms. Substitutional solute atoms interact with edge dislocations only whereas interstitial solute atoms interact with both edge and screw dislocations.
- Modulus interaction – if the shear modulus of a solute atom is different from the matrix then the presence of solute locally alters the modulus. Change in shear modulus affects the strain field of the dislocation.
- Stacking fault interaction – Preferential solubility of solute atoms results in local segregation and reduction in stacking fault energy. Such a phenomena increases separation of the partials thereby causing difficulty in motion of extended dislocations. This aspect has a compounding effect as partial separation distance impacts the ability of dislocations to overcome other obstacles in the lattice.
- Electrical interaction – Difference in the valency of solute atoms from the matrix results in electrical charge accumulation around the solute atoms. Interaction of such charge centers with the dislocations with electrical dipoles contributes to strengthening.
- Short range order interaction – chemical ordering or clustering of atoms provides strengthening to the alloy as extra work is needed for the dislocation motion.
- Long range order interaction – when a dislocation passes through long range arrangement of dissimilar atoms, it dissociates into two pairs separated by anti-phase boundary (APB). The rate of strain hardening is higher in ordered alloys than in disordered alloys.

One or more of these factors constitute to the solid solution strengthening in an alloy. Concentrated solid solution alloys like CoCr-FeMnNi exhibits high mechanical strength due to solid solution strengthening and high ductility due to presence of a homogeneous microstructure [50,109]. Similarly, Senkov et al. [112] studied solid solution strengthening in a TaNbHfZrTi RHEA which has single phase BCC microstructure. Following empirical relations (Eqs. (6) and (7)) were used to calculate the interaction force (f_m) and yield strength (σ_y) of the alloy using atomic size and modulus mismatches between the solute and solvent atoms [113,114],

$$f_m = Gb^2[\delta_G + \beta\delta_a] \quad (6)$$

$$\sigma_y = AG\delta^{\frac{4}{3}}c^{\frac{2}{3}} \quad (7)$$

where G is shear modulus, b is Burgers vector, δ_G is modulus misfit parameter and δ_a is atomic size misfit parameter, c is concentration, β and A are constants. Estimated value of yield strength is 18% higher than the experimental one. These empirical relations are developed for conventional alloys in which the concentration of matrix element exceeds 60–70%, might not be ideal for HEAs. The most widely used model for HEAs is developed by Varvenne et al. [115]. They presented a theory that accounts for the strength of random alloy with n -components based on solute-dislocation interaction energy. Substitutional solute atoms are considered as compositional fluctuations with respect to matrix and interaction of these fluctuations with a dislocation provides strengthening. According to this model the dislocation adopts a wavy configuration at regions of favorable solute fluctuations with a segment length

of ζ_c and amplitude w_c which are determined by energy minimization principles. This bow out describing pinning of a dislocation is a compromise of the two energy contributions. Unpinning of a dislocation is a thermally activated process and this theory gives the expression for zero temperature flow stress (τ_{y0}) and activation energy barrier for the dislocation motion (ΔE_b).

$$\tau_{y0} = 0.051\alpha^{-\frac{1}{3}}\bar{\mu}\left(\frac{1+\bar{v}}{1-\bar{v}}\right)^{\frac{2}{3}}f_\tau(w_c)\cdot\left[\frac{\sum_n c_n \cdot \Delta V_n^2}{b^6}\right]^{\frac{2}{3}} \quad (8)$$

$$\Delta E_b = 0.274\alpha^{\frac{1}{3}}\bar{\mu}b^3\left(\frac{1+\bar{v}}{1-\bar{v}}\right)^{\frac{2}{3}}f_{\Delta E}(w_c)\cdot\left[\frac{\sum_n c_n \cdot \Delta V_n^2}{b^6}\right]^{\frac{1}{3}} \quad (9)$$

where $\alpha, f_\tau(w_c)$ and $f_{\Delta E}(w_c)$ are constants with the value 0.123, 0.35 and 5.7, respectively, typically for HEAs. n is the alloy elements at the overall composition c_n , and ΔV_n is the misfit volume of the n species within the effective matrix. $\bar{\mu}$ and \bar{v} are shear modulus and Poisson's ratio of the alloy, respectively.

At a temperature T and strain rate $\dot{\epsilon}$, flow stress (τ_y) is calculated as;

$$\tau_y = \tau_{y0} \cdot \left(1 - \left(\frac{kT}{\Delta E_b} \ln \frac{\dot{\epsilon}_0}{\dot{\epsilon}}\right)^{\frac{2}{3}}\right) \quad (10)$$

Uniaxial yield stress (σ_y) for an equiaxed FCC polycrystal can be obtained by multiplying the flow stress by Taylor factor,

$$\sigma_y(T, \dot{\epsilon}) = 3.06 \tau_y(T, \dot{\epsilon}) \quad (11)$$

Bracq et al. [116] compared the results predicted using above equations with the experimental ones for 28 different HEAs. The elements considered for the HEA are Co, Cr, Fe, Mn, and Ni and the composition of the elements varied for the different alloys. In case of Fe and Co, the evolution of predicted strength with at.% agreed well with the experimental nanohardness results as shown in Fig. 12.

In case of Cr, a plateau is observed near equiatomic quinary alloy composition due to increase in $\bar{\mu}$ and decrease in δ with higher at.% of Cr. Similarly, LaRosa et al. [117] in their review article, presented the variation in strength of CoCrFeMnNi HEA with temperature and compared it with the predicted values. The results indicated good agreement in the predicted and experimental values especially at intermediate temperatures, as shown in Fig. 13a-c.

This model can be used to predict the effect of minor addition of solutes in HEAs. Varvenne et al. [118] predicted the effect of Al addition on the strength of HEAs, which greatly agreed with the experimental results. The theory suggested the larger strengthening in CoFeCrNiAl_x alloys with addition of Al solutes as compared to CoFeCrNiMnAl_x alloys, consistent with experiments.

Solid solution strengthening is one of the important strengthening mechanisms for HEAs and the models that are developed for predicting the strength of an alloy can be very helpful in designing new alloys.

3.2. Grain boundary (Hall-Petch) strengthening

Crystallographic orientation changes when crossing from one grain to another across the boundary, which in turn poses a resistance to the dislocation motion in any material. Smaller grain sizes decreases the mean obstacle spacing that impede dislocation motion, hence grain size refinement can be an effective strengthening mechanism. The relationship between the yield strength and grain size is given by the classic Hall-Petch equation [119,120],

$$\sigma_y = \sigma_0 + \frac{k_y}{d^{\frac{1}{2}}} \quad (12)$$

where σ_y is yield strength, σ_0 is lattice friction stress, k_y is strengthening coefficient and d is average grain diameter. Eq. (12) indicates that the strength increases with decrease in grain size. However, the effectiveness of grain boundary strengthening is higher for alloys with higher

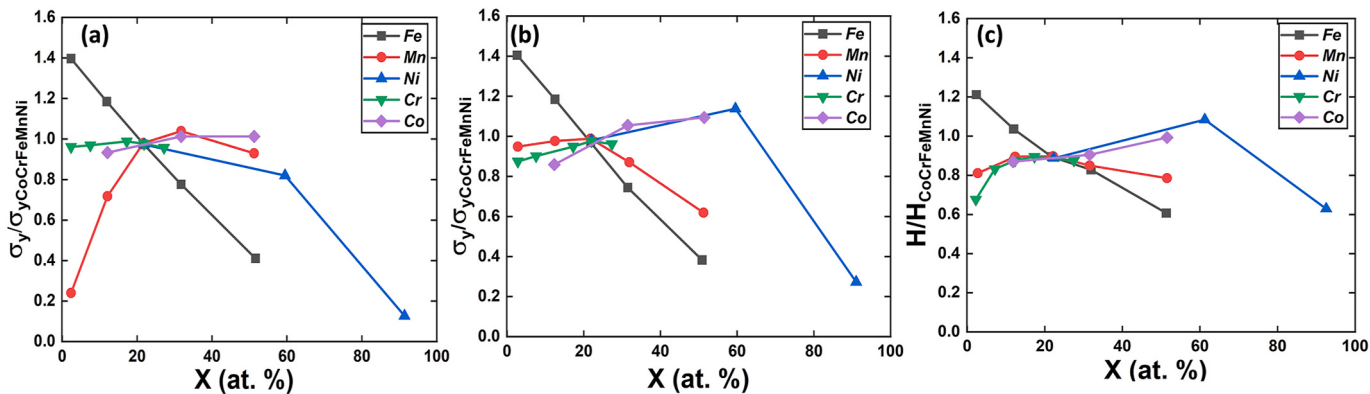


Fig. 12. (a) and (b) Normalized yield strength with respect to $\sigma_{y(CoCrFeMnNi)}$ predicted using Eqs (8)–(11), (a) misfit volumes calculated using atomic volumes obtained from Ref. [116], (b) atomic volumes obtained from Ref. [115], and (c) normalized hardness results with respect to hardness value of CoCrFeMnNi from the nano-indentation tests [116].

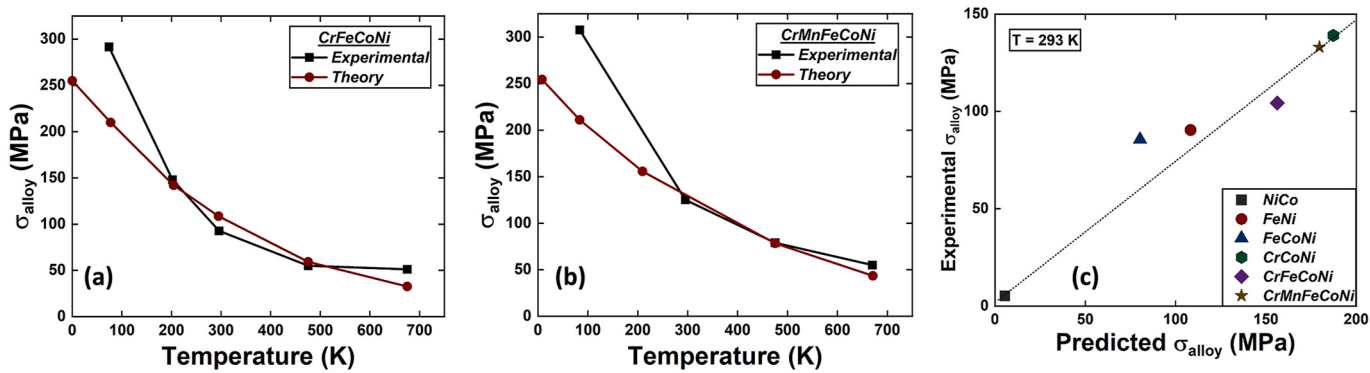


Fig. 13. (a) and (b) Variation in the yield strength with temperature for CrFeCoNi and CrMnFeCoNi HEAs, respectively, and (c) comparison between theoretically and experimentally predicted yield strength for different HEAs [117].

values of k_y . Hall-Petch equation is applicable to other kind of boundaries as well, such as phase boundary, martensite plates, and twins. This equation generally breaks down for very fine grain sizes (≤ 50 nm or so) as the pile up concept no longer applies below a certain grain size [121, 122].

There are various studies available that demonstrated Hall-Petch strengthening in HEAs. Initially, effect of grain refinement was studied on Cantor alloy. Otto et al. [50] performed quasi static tensile test on Cantor alloy with three different grain sizes (4.4 μm , 50 μm , and 155 μm). The Hall-Petch slope (k_y) at room temperature was found to be 494 MPa $\mu\text{m}^{-1/2}$ which is comparatively higher than normal FCC metals

(90–230 MPa $\mu\text{m}^{-1/2}$ [123]). Moreover, it was also observed that the Hall-Petch slope for the Cantor alloy is relatively insensitive to temperature below 873 K, it is 538 MPa $\mu\text{m}^{-1/2}$ at 77 K to 421 MPa $\mu\text{m}^{-1/2}$ at 873 K [50]. Addition of alloying elements on grain boundary strengthening of Cantor alloy has also been studied. Boron addition retards grain growth and provides strengthening for a given grain size [124]. Similarly, addition of C in Cantor alloy improved the value of Hall-Petch slope to 935.25 MPa $\mu\text{m}^{-1/2}$ [125].

Wu et al. [126] studied Hall-Petch strengthening in binary, ternary and quaternary counterparts of Cantor alloy. They observed that the Hall-Petch slope is related to SFE of the respective alloy, and increase in

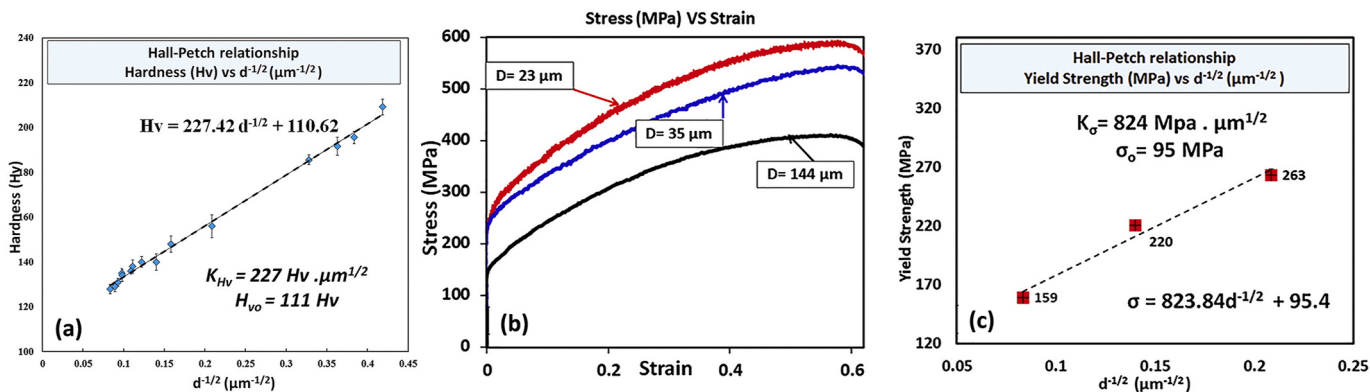


Fig. 14. (a) Vickers hardness as a function of grain size for Al_{0.3}CoCrFeNi HEA, (b) tensile stress-strain plot for Al_{0.3}CoCrFeNi HEA for three different grain sizes, and (c) yield strength as a function of grain size (taken from Ref. [127]).

SFE reduces the Hall-Petch slope. The change in Hall-Petch slope with the addition of alloying elements is as follows: pure Ni (slope = 34 HV $\mu\text{m}^{-1/2}$), Ni-Co (slope = 167 HV $\mu\text{m}^{-1/2}$), Fe-Ni (slope = 113.4 HV $\mu\text{m}^{-1/2}$), Ni-Co-Cr (slope = 131.1 HV $\mu\text{m}^{-1/2}$), Ni-Fe-Co (131 HV $\mu\text{m}^{-1/2}$) and Fe-Ni-Co-Cr (slope = 165 HV $\mu\text{m}^{-1/2}$). Gwalani et al. [127] studied effect of aging time and temperature on the strength of a single phase FCC $\text{Al}_{0.3}\text{CoCrFeNi}$ HEA. Fig. 14 (a and b), respectively, show the variation of Vickers microhardness and tensile strength with the grain size indicating classic Hall-Petch grain size dependence. Addition of Al to Fe-Ni-Co-Cr improved the Hall-Petch slope from 165 HV $\mu\text{m}^{-1/2}$ to 227 HV $\mu\text{m}^{-1/2}$. Effect of grain size on the tensile strength was also evaluated for grain sizes of 23 μm , 35 μm , and 144 μm of a FCC $\text{Al}_{0.3}\text{CoCrFeNi}$ HEA. Tensile yield strength increased from ~ 160 MPa to ~ 260 MPa and the Hall-Petch plot is shown in Fig. 14 (c). The Hall-Petch slope calculated for $\text{Al}_{0.3}\text{CoCrFeNi}$ HEA was 824 MPa $\mu\text{m}^{-1/2}$ [127] whereas for a friction stir processed $\text{Al}_{0.1}\text{CoCrFeNi}$ HEA it was found to be 371 MPa $\mu\text{m}^{-1/2}$ [128].

Sriharitha et al. [129] studied the effect of Al addition in a spark plasma sintered (SPS) $\text{Al}_x\text{CoCrCuFeNi}$ HEA. Although the hardness is improved with Al addition, the contribution from grain size strengthening was not considerably affected. Kang et al. [130] observed very high Hall-Petch slope for compressive yield strength of SPS WN₆MoTaV HEA, 1462–1774 MPa $\mu\text{m}^{-1/2}$, however the strength of the alloy is mainly governed by solid solution strengthening. Hall-Petch slope for HfNbTaZrTi HEA is observed to be 270 MPa $\mu\text{m}^{-1/2}$ which is much lower than other HEAs although its friction stress is much higher [131].

3.3. Precipitation strengthening

Rich compositional variability of HEAs provide tremendous opportunity to play around and produce desired microstructure which can manipulate resultant properties. Activation of different strengthening mechanisms by varying composition or thermomechanical treatment is a major advantage of HEAs. Precipitates in a ductile matrix are a very effective and common source of alloy strengthening. Precipitates are formed by controlled aging of the alloy at temperatures lower than solution temperature at which solubility of precipitate forming alloying elements is limited, after solution heat treatment of the alloy. Strengthening as a result of precipitation depends on distribution of precipitates in the matrix, volume fraction of precipitates, precipitate size, and spacing between precipitates. When dislocations interact with precipitates, they can either cut the particles or bypass them by looping. When the particles are small, the dislocation shears them. Shearing of precipitates provides strengthening to the material via coherency strains, SFE mismatch between particle and matrix, presence of ordering in particles, modulus mismatch, addition of new interfaces, and difference in Peierls stress in the precipitate and matrix.

However, above certain precipitate size shearing become difficult and dislocations start bypassing the precipitate by looping mechanism. Stress required to advance the dislocation between precipitates separated by a distance λ is given by (referred as the Orowan stress),

$$\tau_0 = \frac{Gb}{\lambda} \quad (13)$$

Precipitation hardened Ni based superalloys are best examples for precipitation strengthening, the microstructure of which consists of FCC γ phase matrix and a high volume fraction of L1₂ γ' precipitates. The γ' phase provides superb resistance against shearing via lattice dislocation movement, and thus remarkable strength at high temperature. Initially, main focus of HEAs was to emphasize single phase solid solution but recently to enhance structural properties and high temperature performance, development of multiphase HEAs has been embraced (refer to Contexts #3 & #4).

The concept of precipitation strengthening in Ni based superalloys has been extended to HEAs. Addition of Ti, Mo and Nb in $\text{Al}_{0.3}\text{CoCrFeNi}$ and CoCrFeNi show enhanced strength by forming precipitates.

Addition of Mo resulted in a change in microstructure from single phase FCC CoCrFeNi to (Cr,Mo) – rich σ in FCC matrix [132]. With increase in Mo content from 0 to 0.85 (molar ratio), yield stress improved from 136 MPa to 929 MPa. Addition of Nb in the single phase FCC CoCrFeNi resulted in eutectic alloy composed of ductile FCC phase and a hard Laves phase with fine laminar structure [133]. Compressive strength of the material increased from 2025 MPa to 2505 MPa when Nb content is increased from 0.25 to 0.8 (molar ratio).

Gwalani et al. [127] studied microstructural evolution and corresponding mechanical properties with different thermomechanical processing in $\text{Al}_{0.3}\text{CoCrFeNi}$ HEA. Homogenized microstructure revealed single phase FCC microstructure whereas aging at 550°C for 150 h indicated presence of L1₂ precipitates and aging at 700°C for 50 h resulted in B2 precipitates. Enhanced yield strength has been observed for aged samples due to the presence of ordered precipitates as compared to homogenized one. Niu et al. [134] observed formation of nanosized B2 precipitates in $\text{Al}_{0.5}\text{CoCrFeNi}$ after heat treatment which in as-cast condition exhibited a mixture of FCC and BCC crystal structure. Yield strength of the material increased from 355 MPa for as-cast to 834 MPa for heat treated HEA. Tong et al. [135]. Addition of Ti in CoCrFeNi indicated strong affinity of Ti towards Ni due to presence of high enthalpy of mixing and hence aging of the alloy resulted in Ni and Ti rich precipitates at the grain boundaries as well as grain interior. As compared to parent FeCoCrNi, the yield strength of the alloy increased by 160%. Strengthening calculation shows that formation of (NiCo)₃Ti precipitate and solid solution strengthening due to Ti contributed to the strength enhancement. Similarly, addition of Ti and Al in single phase FCC FeCoNiCr HEA and subsequent thermomechanical processing led to nucleation of L1₂ Ni₃(Ti,Al) precipitates [19]. After processing, the alloy showed over 1 GPa yield strength and strengthening calculation revealed that precipitation strengthening was the major strengthening mechanism.

Variation of Al in Al–Co–Cr–Fe–Ni HEA can affect the phase stability; increase in Al concentration can change the dominant phase from FCC to BCC. Ma et al. [136] varied the alloying elemental concentration in order to vary the phase stability in Al–Ni–Co–Cr–Fe HEA. They reported that phase stability is closely related to the valence electron configuration. The microstructure varied from dual phase FCC + BCC/B2 to single phase BCC/B2 with a decrease in valence electron configuration. Additionally, the BCC phase in the microstructure was always accompanied by B2 precipitates. Strengthening due to B2 precipitates was determined by the lattice misfit between BCC and B2. When the lattice misfit was 0.4%, maximum strength was obtained due to presence of coherent cuboidal precipitates. Dasari et al. [137] subjected an $\text{Al}_{0.5}\text{Co}_{1.5}\text{CrFeNi}_{1.5}$ HEA to different thermomechanical treatments, which resulted in wide ranging microstructures. Homogenization at 1150°C for 6 h resulted in single phase FCC, and subsequent annealing at 750°C for 50 h gave FCC with L1₂ precipitates. On the other hand, 60% cold rolling and subsequent annealing at 750°C for 50 h resulted in FCC with B2 precipitates. Single phase FCC showed yield strength of 180 MPa with a ductility of 62%, FCC + L1₂ gave yield strength of 360 MPa with ductility of 48%, and FCC + B2 resulted in yield strength of 790 MPa and ductility 20% which indicates that development of ordered phases in the matrix improves the strength at the expense of ductility.

Thermomechanical treatment of $\text{Al}_{0.3}\text{CoFeNi}$ HEA results in the formation of complex four phase (FCC + L1₂+B2+BCC) microstructure, which provides a high yield strength of 1490 MPa with a ductility of 12% [22]. Moreover, cold worked and annealed $\text{Al}_{0.3}\text{CoCrFeNi}$ HEA contained a $\Sigma 3$ twin boundaries which provides nucleation sites for ordered B2 precipitates in FCC grains [138]. Uniformly distributed B2 precipitates at the grain boundaries, deformation bands and twins along with $\Sigma 3$ twin boundaries provide strengthening to the alloy.

It is important to emphasize that the situation of precipitation strengthening is more complex in HEAs as compared to conventional alloys. Let us consider impact of precipitate evolution in Ni-base superalloys and contrast that with $\text{Al}_{0.3}\text{FeCoCrNi}$ HEA. When a Ni-base

superalloy is aged, the supersaturated γ matrix transitions to $\gamma+\gamma'$ microstructure. The γ' is an ordered ($L1_2$ structure) Ni_3Al phase, where Ni and Al sub-lattices can be substituted by other alloying elements present in the alloy. The key thing here is that for a given Ni-base superalloy composition, a particular type of $L1_2$ precipitates out and the crystal structure as well as the composition of the precipitate is fixed. However, in the $Al_{0.3}FeCoCrNi$ HEA, depending on the prior thermo-mechanical processing path and choice of aging temperature, one can obtain $L1_2$ or $B2$ or σ (or a combination) precipitate. Note that $L1_2$ is a Ni_3Al type precipitate, $B2$ is a $NiAl$ type precipitate and σ is a $FeCr$ type precipitate. This is very significant as the SFE of the matrix changes with the type of precipitate. The $Al_{0.3}FeCoCrNi$ HEA exhibits twinning in solid solution condition. If $L1_2$ or $B2$ precipitates out, the remaining matrix SFE is likely to decrease. Whereas if σ precipitates out the impact will be opposite. So, the evaluation of strengthening requires extra careful analysis in these HEAs!

3.4. Martensite strengthening

Diffusionless shear type martensitic transformation upon quenching in steels is one of the most common strengthening mechanism in iron-based systems. Martensitic structure provides strong barrier to dislocation motion. There are two structural contributions to the high strength; martensitic plate structure with a unique habit plane with parallel twins within the plates and block martensite containing high dislocation density. Compositional flexibility in HEAs provide opportunity to explore martensite strengthening as one of the strengthening mechanisms for HEAs. Zhang et al. [139] reported formation of lath martensite in $FeCoNiCrCuTiMoAlSiB_{0.5}$ HEA fabricated by laser cladding. Rapid solidification during laser cladding and boron interstitial are the two possible causes for martensite nucleation. High dislocation density in the lath structure provides strengthening to the alloy, hardness of the alloy is reported as 11.3 GPa. In a $TiZrHfAlNb$ HEA, the microstructure is characterized by metastable β phase and martensitic α'' phase, presence of which enabled excellent strength to the alloy. Additionally, the alloy exhibited superelastic behavior due to reversible martensitic transformation [140]. Li et al. [141] in their pioneer work utilized the compositional flexibility in HEAs by varying the Mn content to introduce dual phase HEAs which undergo strain induced martensitic transformation under deformation thereby improving the strength and ductility of the alloy. Nene et al. [38,59] explored the compositional space available for HEAs through minor addition of elements such as Cu, Al, and Si to engineer the stability of martensitic (ϵ , HCP) phase. Further experimental and computational analysis revealed that non-basal $<cc+a>$ pyramidal slip and twining in the martensitic phase provided extensive strength, work hardening, and ductility to the alloy. Detailed exploration of martensitic transformation induced plasticity and related deformation mechanisms are performed in a later section.

4. Deformation mechanisms in HEAs

In section 3, the effect of alloy composition, principal element selection and the thermomechanical processing on lattice distortion and subsequent solid solution strengthening has been discussed. Excellent strength and work hardening behavior shown by HEAs are attributed to their superior solid solution strengthening as a result of excessive lattice distortion due to the presence of multiple principal elements. A general question arises, how monotonic is the increase in solid solution strengthening and subsequent yield strength with a monotonic increase in number of principal elements from ternary to quinary and senary compositions? Upfront thoughts when regarding extend of lattice distortion with addition of more elements cause one to speculate that the yield strength may increase with an increase in number of elements. However, recent studies on the effect of number of alloying elements revealed negligible dependency of yield strength from quaternary $CoCrFeNi$ to quinary $CoCrFeNiMn$ HEAs [52]. Also, it has been reported

that the equimolar ternary $CoCrNi$ MEA has the highest strength when compared to its equimolar quaternary and quinary counterparts with elements Co, Cr, Fe, Mn and Ni [142]. Additionally, the observed strength difference in all three equimolar quaternary HEAs suggests that the selection of principal elements also matters. For example, equimolar $CoCrFeNi$ exhibited more strength than $CoFeNiMn$ alloy [142]. Hence, high entropy of mixing in multicomponent alloys facilitates solid solution strengthening by overcoming the enthalpy of formation of secondary phases, whereas, proper selection of principal elements in the multicomponent system governs the strength properties of the alloy by optimizing the lattice distortion and volume misfits in the lattice structure. This section tries to explain the effect of alloying composition on dislocation activation and its propagation as well as propensity of other deformation modes such as twinning and deformation induced transformation in HEAs.

4.1. FCC based HEAs

Although the HEA compositional pool at present is really vast, major exploration has been carried out in the equimolar FCC based $CoCrFeNiMn$ Cantor alloy which has served as a model system [2,125, 143–153]. Hence, Cantor alloy is taken as an illustrative example for the current discussion. Yield strength of Cantor alloy increases from ~200 MPa at room temperature to ~400 MPa at 77 K and it reduces to ~100 MPa at 1073 K (grain size ~50 μm) [50,154]. Additionally, Cantor alloy also behaves in accordance with Hall-Petch effect where the flow stress increases from ~225 MPa for 100 μm grain size to ~800 MPa for ultrafine grained alloy at room temperature [155]. Also, the yield strength for the coarser alloy showed improvement by ~120% and the ductility improved by ~37% when the temperature is reduced from room temperature to 77 K. Extensive research have been carried out to understand the deformation mechanisms in FCC based HEAs in order to explain the mechanical response as a function of microstructure, composition and temperature. An attempt is made in the following sections to explore the thermally activated deformation mechanisms in FCC based HEAs which directly associate to the mechanical response.

4.1.1. Dislocation mediated plasticity via slip

Early study on dislocation generation in Cantor alloy by Otto et al. [50] revealed that the initial stages of plastic deformation is characterized by planar dislocation glide of $\frac{1}{2}[1\ 1\ 0]$ dislocations on {1 1 1} slip planes in all microstructures considered (grain size varies from 4.4 to 155 μm) and temperatures (77–873 K). Additionally, presence of stacking faults in the material suggested the dissociation of the dislocations into $\frac{1}{6}[1\ 1\ 2]$ Shockley partials. Laplanche et al. [154] investigated the evolution of dislocation in $CoCrFeNiMn$ alloy at 77 K and 293 K and observed that the initial deformation is characterized by formation of dislocation pileups, whereas at larger strain levels, the dislocations reorganize themselves into cell structures. Of special emphasis, negligible variation was observed in dislocation density at 77 K and 293 K, suggesting that the dislocation evolution is independent of temperature, although twinning was visible at liquid nitrogen temperature. Similar observations on dislocation evolution in Cantor alloy was reported by Zhang et al. [156] using in situ TEM experiments where deformation mechanisms were observed in the vicinity of a crack tip. Continuous nucleation and annihilation of stacking faults ahead of crack tip revealed ease of propagation of the partials through the matrix. On further straining, the undissociated $\frac{1}{2}[1\ 1\ 0]$ dislocations start to move.

However, the motion of undissociated dislocations were significantly sluggish than the partial dislocation motion thereby resulting in close-packed dislocation arrays. Such slow moving full dislocation arrays impeded the easy motion of the partial dislocation which

subsequently enhanced the work hardenability of the alloy. Additionally, microscopic analysis of dislocation network on preferred {1 1 1} plane after single crystal micropillar compression tests in CoCrFeNiMn alloy by Okamoto et al. [157] revealed presence of smoothly curved dislocations without any preferred line direction which suggests lack of anisotropy on the mobility of screw and edge dislocations. Low SFE suppressed the generation of cross-slip of screw dislocation which is evident from the planarity of dislocation pile up on {1 1 1} plane.

The temperature dependency on yield stress, dislocation evolution, and work hardening was further investigated by analyzing evolution of activation volume at different temperature and plastic strain levels using load relaxation experiments [154,158,159]. Activation volume changed from $\sim 30 b^3$ at 77 K to $\sim 360 b^3$ at 293 K at the yield stress [154]. Also, rate of decrease in activation volume with plastic strain is relatively lower at 77 K than at 293 K. Lower dislocation activation volume and its rate of decrease with strain rate can be directly correlated to higher strength and work hardenability in CoCrFeNiMn HEA at lower temperature. Additionally, activation volume reduced with increase in plastic strain at all temperatures; the behavior is in accordance with the trend in forest dislocation accumulation with strain, thereby reducing the activation volume of dislocation. Good agreement of the trend in activation volume with Cottrell-Stokes law, as in common solid solution strengthened FCC alloys, indicates that the structural intricacies and compositional complications have not resulted in any intrinsic deformation mechanisms typical for HEAs. Earlier, Wu et al. [158] studied the effect of thermally activated process on deformation mechanisms in equiatomic HEAs ranging from binary to quinary alloys which are the subsets of CoCrFeNiMn equiatomic HEA. They applied the Labusch strengthening model [160,161] to multicomponent alloys as in Refs. [162–164], neglecting the Hall-Petch effect and thermal effects. A qualitative agreement between the athermal contribution to yield strength and the Labusch strengthening factor, L , suggested the dominant contribution of solid solution strengthening mechanisms in equiatomic HEAs rather than lattice friction effects. Comparatively larger activation volumes reported by Wu et al. [158] for quinary to ternary equiatomic compositions ($\sim 7 b^3$ – $\sim 28 b^3$ at 77 K and $\sim 47 b^3$ – $\sim 77 b^3$ at 293 K) also suggest that the dominant deformation mechanism cannot be of kink-pair interactions which rather needs lower activation volumes (~ 1 – $5 b^3$). Labusch model considered the evolution of plastic deformation by motion of non-straight dislocations and local bowing of dislocation lines due to thermally activated processes. Analyzing the activation volumes and the yield strength of different equiatomic alloys,

Wu et al. [158] suggested that alloys with large activation volume (e.g. binary compositions) are characterized by long range bowing of dislocation lines, whereas those alloys with small activation volumes (ternary and quaternary compositions) may cause local fluctuations along the dislocation lines due to local lattice distortions, as illustrated in Fig. 15a-b. Smith et al. [165] used HAADF STEM imaging to determine the dissociation distance of 60° mixed dislocations piled up near an annealing twin boundary. An interesting observation is the huge variation in the partial dissociation distance which varied between ~ 1 nm and ~ 8 nm with a mean and standard deviation values of 4.82 nm and 1.93 nm. Such a drastic variation in the dissociation distance led to the concept of a “local SFE” in HEAs. However, high-resolution EDX analysis performed on the sample confirmed uniform distribution of all constituent elements in the matrix and nullified the effect of local short-range order on partial separation. Further, embedded-atom-method (EAM) was used in a ternary NiFeCr alloy to understand the local fluctuations in partial separation as compared to pure Ni and a weak Ni–Fe alloy. Irregularity in the separation distance confirmed larger variation in “local SFE” in NiFeCr when compared to pure Ni and weak Ni–Fe solid solution which further confirmed the experimental observations (Fig. 15c).

Study on another single phase FCC Al_{0.1}CoCrFeNi HEA by Xu et al. [166] revealed the presence of $\frac{1}{2}[1\bar{1}0]$ full dislocations as well as dissociated Shockley partials with a Burgers vector of $\frac{a}{6}[1\bar{1}2]$ on {1 1 1} slip plane, for which the SFE was experimentally determined between 6 and 21 mJ m⁻². Additionally, presence of extensive immobile dislocations in the form of Lomer locks (due to interaction of two complete dislocation on different slip planes) and Lomer-Cottrell locks (due to interaction of dislocation partials on different slip planes) inhibited dislocation movement and resulted in excellent strain hardening and ductility in the alloy as they act as Frank-Read sources for dislocation nucleation as well as twin nucleation (Fig. 16). Similar to the observation on dislocation dissociation separation by Smith et al. [165], a variation in separation distance was also observed between the dislocation partials in Al_{0.1}CoCrFeNi HEA (~ 5 nm– ~ 34 nm). Such a variation is attributed to the nature of the dislocation; a pure screw dislocation (dislocation character angle = 0°) has a lower separation distance (~ 10 nm) whereas a pure edge dislocation is wider (~ 34 nm) although such higher separation distance is surprising in FCC alloys with lower SFE (Fig. 16(b–c)).

Ding et al. [167] studied the effect of replacing Mn in Cantor alloy with Pd in the microstructure and corresponding dislocation evolution.

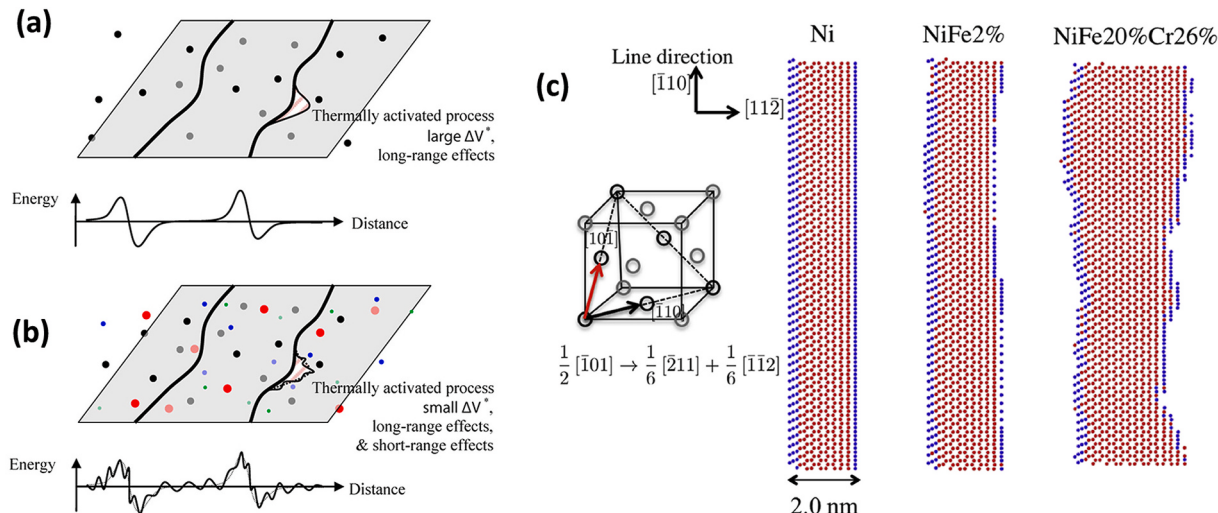


Fig. 15. (a) Schematic of long-range bowing of dislocation in alloys having large activation volume (ΔV^*), (b) influence of local short-range stress fields resulting in local fluctuations over the long range effect of dislocation motion [158], and (c) variation in partial separation distance in NiFe₂₀%Cr₂₆ alloy when compared to pure Ni and dilute NiFe alloy [165].

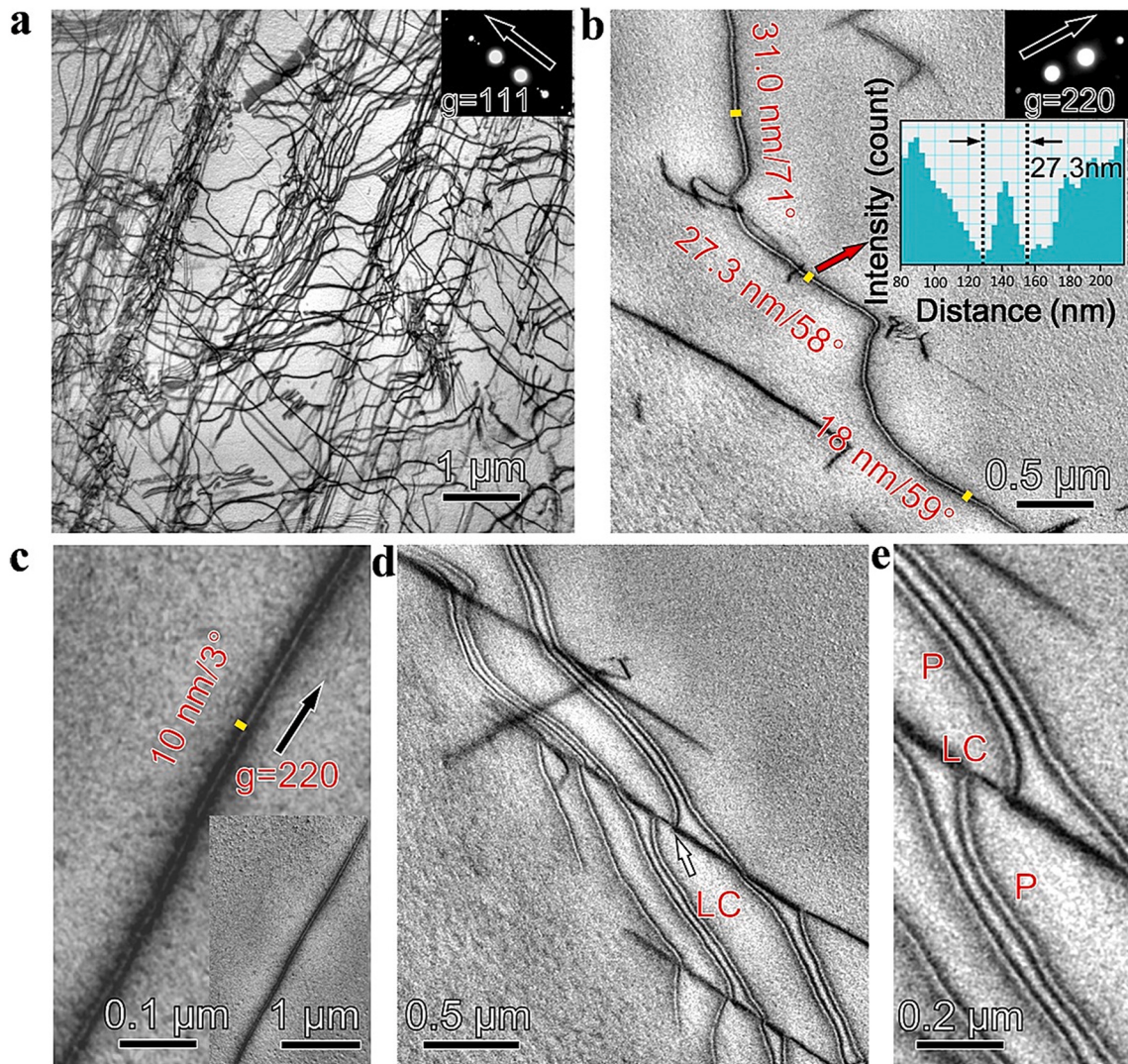


Fig. 16. (a) Transmission electron micrograph indicating the dislocation network in $\text{Al}_{0.1}\text{CoCrFeNi}$ HEA, (b) variation in dissociation widths of partial dislocation along with the character angles, (c) a dissociated dislocation with a narrow dissociation width at very low character angle, (d) and (e) presence of Lomer-Cottrell junctions formed as a result of dislocation activity on two $\{1\ 1\ 1\}$ planes [166].

Addition of larger and more electronegative Pd atoms has completely disturbed the elemental distribution in the matrix which resulted in local elemental inhomogeneity and larger lattice strains. Reflection of such a local inhomogeneity was observed in the deformation mechanism as well. Unlike Cantor alloy, the plastic deformation in CoCrFeNiPd alloy was characterized by full $\frac{1}{2}[1\ 1\ 0]\{1\ 1\ 1\}$ dislocations. SFE obtained from dislocation core width measurement was obtained as 66 mJ m^{-2} , almost twice as that of Cantor alloy. Additionally, the dislocation glide was also sluggish due to higher lattice strains involved which resulted in pinning of dislocations. Higher resistance in the primary slip plane caused the screw dislocations to undergo extensive cross-slip which enhanced the strength, work hardening, and ductility in the alloy.

4.1.2. Twinning induced plasticity (TWIP)

Excellent properties in HEAs can be achieved by triggering strain accommodating mechanisms other than dislocation mediated slip. Mechanical twinning is one such method of strain accommodation [168]. Deformation twinning in FCC metals and alloys improved the work hardening rate and ductility, hence twinning is favored for excellent mechanical performance. Extensive research has been carried out in FCC metals and alloys on twin nucleation and its interaction with slip

systems [169–172]. Progression of deformation mechanism in FCC crystals under deformation depends on SFE of the metal/alloy [77,173, 174]. Several mathematical models were also proposed to predict twin nucleation and twinning mechanism in FCC crystals [77,169,175–180]. This section provides explanation about how twinning as a strain accommodation mechanism is favored in HEAs as well as the dependence of microstructural parameters on twinning.

Propensity of mechanical twinning in alloys of structural importance can be achieved by carefully controlling the SFE of the alloy. In the model proposed by Allain et al. [181] for steels, mechanical twinning occurs when the SFE lies in the range $12\text{--}35 \text{ mJ m}^{-2}$. However, based on various experimental results, Galindo-Navarro and Rivera-Díaz-del-Castillo [77] reported that twinning is probable when SFE lies between 18 mJ m^{-2} and 30 mJ m^{-2} (Fig. 17a). For austenitic steels having $\text{SFE} < 18 \text{ mJ m}^{-2}$, strain induced martensitic transformation and twinning can exist in synergy at larger plastic strains [173,182,183]. Although the mechanism of martensitic and twinning embryo formation is similar and relates to stacking fault formation through the dissociation of $\frac{1}{2}[1\ 1\ 0]\{1\ 1\ 1\}$ full dislocation into $\frac{1}{6}[1\ 1\ 2]\{1\ 1\ 1\}$ Shockley partials, the sequence of stacking faults on $\{1\ 1\ 1\}$ planes differs. Twin embryo forms when stacking faults overlap on three successive $\{1\ 1\ 1\}$ planes as

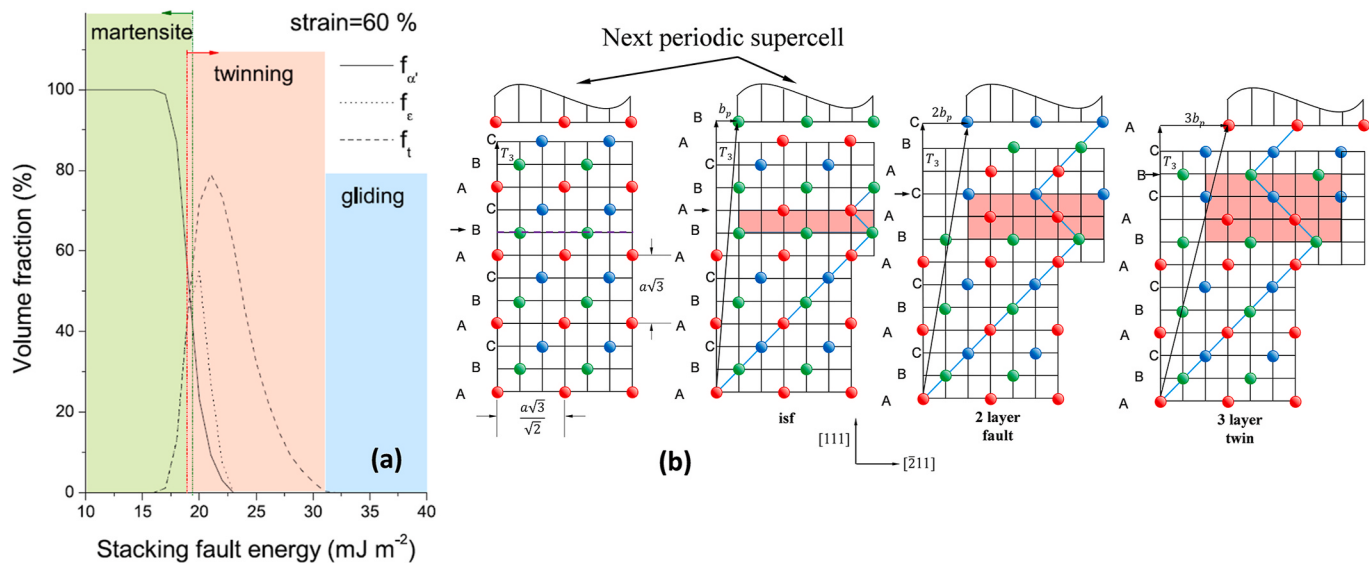


Fig. 17. (a) Variation in the volume fraction of α' , ϵ and twinning for different stacking fault energies at $\varepsilon = 60\%$ [77]), and (b) progression of dislocation mechanism resulting in a twin embryo when stacking faults are formed on three consecutive atomic layers [184].

indicated in Fig. 17b [77,184]. Relatively low SFE reported in high entropy alloys [51,97,185–188] confirms the possibility of twinning under large plastic deformation.

Several attempts have been made to predict the critical stress for twinning (τ_{tw}) in FCC based metals/alloys [169,189–192]. Initial works assumed that the critical twinning shear stress (τ_{tw}) is dependent only on the intrinsic SFE (γ_{isf}) as per the following approximation (Eq. (14)) and the twinning stress is equivalent to the stress required for generation of a dislocation pileup or Lomer-Cottrell lock [189,192],

$$\tau_{tw} \sim K \frac{\gamma_{isf}}{b_{tw}}, \quad (14)$$

where b_{tw} is the Burger's vector of the Shockley partial. Kibey et al. [184] developed a multi-scale approach based on the twin energy pathways wherein the twinning stress is obtained by optimizing the total energy associated with dislocation configuration leading to twin nucleation with respect to width of the twin nucleus (d_{tw}) and number of $\{1\ 1\ 1\}$ layers within the twin nucleus ($N = 3$). The closed form solution is complex; however, the functional form is given by,

$$\tau_{tw}(d) = \tau(\gamma_{isf}, \gamma_{tsf}, \gamma_{us}, \gamma_{ut}, G_{\{111\}}, N, d), \quad (15)$$

where γ_{us} is the stacking fault nucleation barrier, γ_{tsf} is the single layer SFE, γ_{ut} is the twin nucleation barrier, γ_{tsf} is the coherent twin boundary energy, and $G_{\{111\}}$ is the in plane shear modulus. Later, Wong et al. [179] proposed an energy based approach and defined the twinning stress as the stress at which the total energy of the dislocation configuration for twin embryo formation reaches a saddle point. They described the critical twinning stress as follows,

$$\tau_{tw} = \frac{\gamma_{sf}}{3b_{tw}} + \frac{3Gb_{tw}}{L_{tw}}, \quad (16)$$

where L_{tw} is the length of the sessile Shockley partial. An important aspect is that the critical twinning stress is proportional to SFE of the metal/alloy, lower the SFE higher is the probability of deformation twinning. However, very low SFE will lead to martensitic transformation, the aspect that will be discussed later.

Laplanche et al. [185] studied the evolution of twinning in CoCr-FeNiMn alloy at cryogenic (77 K) as well as room temperatures (293 K). At 77 K, the work hardening rate was observed to remain constant after an axial strain of 7.4%, whereas at 293 K, the work hardening rate kept

on reducing with strain (Fig. 18a-b). The constant work hardening rate at 77 K was attributed to extensive nano-twinning occurring in the grains which further results in dynamic Hall-Petch strengthening as a result of creation of multiple new interfaces (Fig. 18c). The newly formed twin boundaries act as barriers to dislocation motion by reducing the mean free path of dislocation, thus resulting in sustained work hardening in the material. At room temperature (293 K), twinning was visible only at larger deformation near to fracture. However, the critical stress for twinning, determined as ~ 720 MPa, was independent of temperature. Similarly, intersected deformation twins were also observed in CoCrFeNiMn alloy after severe asymmetric rolling [150]. Comparative study on deformation mechanism in CoCrNi MEA and CoCrFeNiMn HEA reported some interesting results on the progression of deformation mechanisms at cryogenic temperature (77 K) as well as room temperature (293 K) [97]. In both the alloys, initial deformation stage was characterized by dislocation glide of $\frac{1}{6}[1\ 1\ 2]$ partial dislocations through the dissociation of $\frac{1}{2}[1\ 1\ 0]\{1\ 1\ 1\}$ dislocation on $\{1\ 1\ 1\}$ glide plane. The average Shockley partial separation was determined to be ~ 8 nm in CoCrNi alloy whereas the average partial separation was ~ 5.25 nm in CoCrFeNiMn HEA, which suggested that the MEA has a lower SFE (~ 22 mJ m^{-2}) when compared to the HEA (~ 30 mJ m^{-2}). Hence, wider separation of partials in MEA could restrict cross-slip and promote dislocation glide during early deformation stage. Critical twinning stress was determined to be more or less similar for both the alloys; ~ 790 MPa for MEA and ~ 720 MPa for HEA. However, higher yield strength in MEA when compared to HEA at both room temperature and cryogenic temperature facilitated nano-twinning during early stages of deformation ($\sim 5\%$ at 77 K and 11.5% at 293 K). Further studies on CoCrFeNiMn alloy under deformation also confirmed the presence of nano-twinning [144,193–195]. Liu et al. [186] studied the evolution of twinning and subsequent texture in CoCrFeNiMn alloy at cryogenic temperature. In line with the results of Laplanche et al. [185], the constant hardening rate after the initial drop was attributed to nano-twin formation inside the grains. Deformation twins were developed inside the preferentially oriented $\{1\ 1\ 1\}$ grains parallel to the tensile loading axis (TA), the density of which intensified with plastic deformation resulting in a weak $\{1\ 1\ 5\}$ texture along the tensile axis. Kireeva et al. [194] extensively studied the orientation dependence of twinning evolution in CoCrFeNiMn single crystals. Although the Schmid's law was fulfilled, grain orientation has significant effect on the

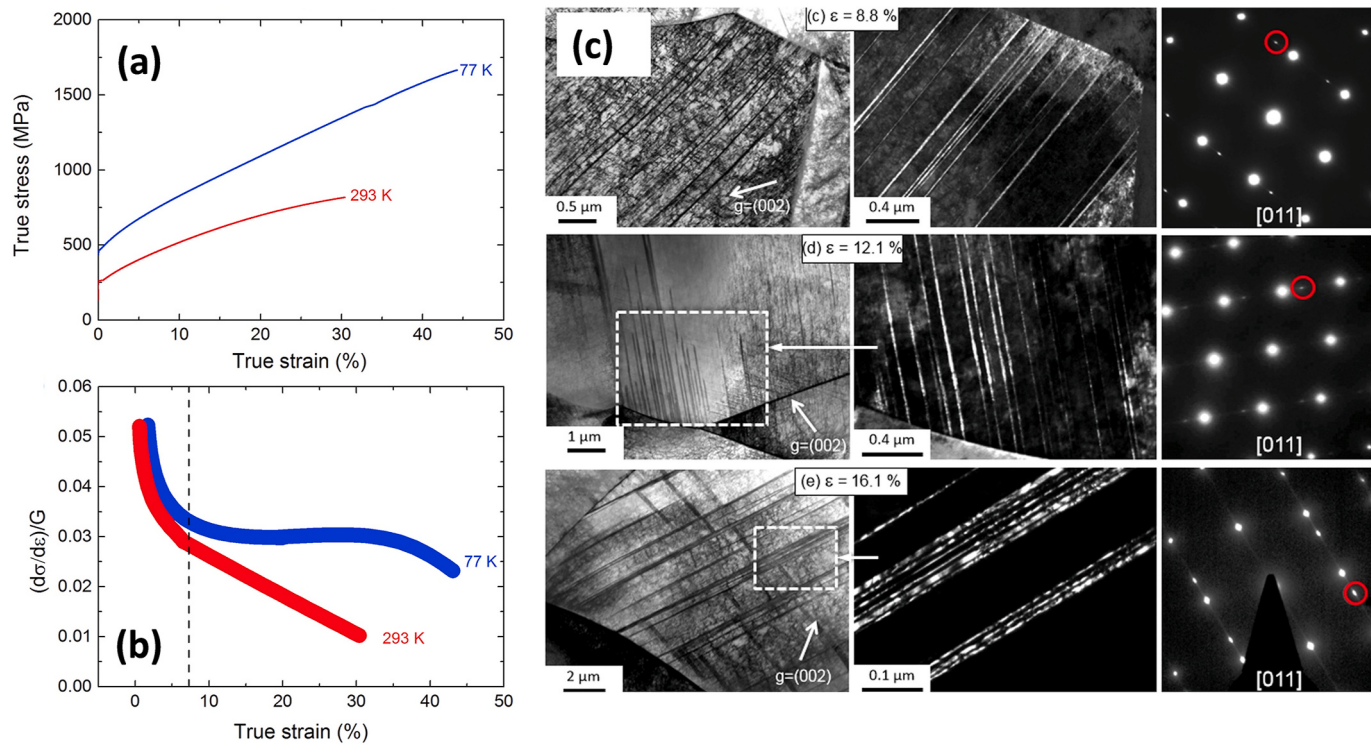


Fig. 18. (a) True stress-strain response of CoCrFeNiMn alloy at cryogenic (77 K) and room temperatures (293 K), (b) work hardening curves normalized with shear modulus corresponding to the curves in (a), and (c) presence of nano-twinning observed in the alloy at cryogenic temperature [185].

onset of twinning. It was observed that twinning initiated at 5% strain in $[1\bar{1}1]$ oriented crystal, whereas presence of twinning was identified only after a strain of 27% in $[1\bar{2}3]$ oriented crystal, at room temperature. Additionally, no proof of deformation twinning was observed in $[001]$ oriented crystal. However, at cryogenic temperature (77 K), evidence of deformation twinning was observed in single crystal oriented along $[001]$ [194]. Unlike the results of Laplanche et al. [185] and Liu et al. [186], Joo et al. [193] reported the progression of deformation twins in CoCrFeNiMn HEA at room temperature before the onset of necking after cold rolling and homogenization. Similar results on twin formation was also reported in Ref. [195] after rolling. Grains oriented along $<111>/TA$ favored deformation twinning rather than those grains oriented along $<001>/TA$ and $<101>/TA$. Sun et al. [196] studied the effect of grain refinement on deformation twinning in FCC based metallic materials increases with a reduction in grain size which can be expressed using the following equation [197],

$$\sigma_{tw} = m \frac{\gamma_{sf}}{b_{tw}} + \frac{k_T}{\sqrt{d}}, \quad (17)$$

where m is the Taylor factor, k_T is the Hall-Petch constant for twinning, and d is the grain size. Once the grain size falls in the ultrafine-grained regime, plastic deformation progressed with lack of deformation twinning, whereas deformation twinning prevailed in coarse grained alloy. Such a behavior is in accordance with deformation behavior in other common FCC metals [176,197–199] where deformation twinning capability reduced with grain refinement. Fig. 19 shows the predicted twinning stress according to Eq. (17) for CoCrFeMnNi HEA which reveals that the critical twinning stress is higher than the flow stress for grain size $<2 \mu\text{m}$. Impact of deformation twinning on fatigue crack growth behavior in Cantor alloy was also explored. Development of nano-twinning in the plastic zone ahead of crack tip enhanced the fatigue crack growth resistance in CoCrFeNiMn HEA as reported in Refs. [200,201].

Apart from the Cantor alloy, deformation twinning was also

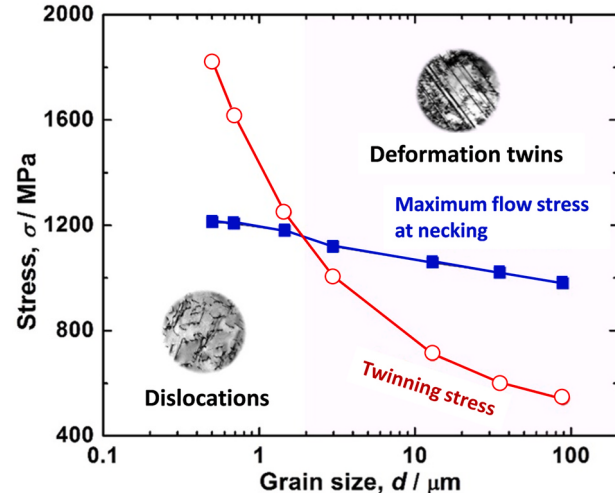


Fig. 19. Twinning stress predicted using Eqn. (17) and experimentally observed maximum flow stress as a function of grain size for CoCrFeMnNi HEA [196].

observed in other single phase FCC solid solution HEAs which is achieved by tuning SFE by minor elemental additions [25,202–209]. Wu et al. [202] studied the evolution of deformation mechanisms in $\text{Al}_{0.1}\text{CoCrFeNi}$ with a heterogeneous microstructure having a network of fully recrystallized and non-recrystallized grains. Presence of deformation twins was observed in the non-recrystallized grains at a strain level of 5.6%, whereas twinning was delayed in the recrystallized grains. Activation of twinning mechanism along with the presence of a heterogeneous microstructure resulted in excellent strength and ductility in the alloy. Further, a decrease in grain size resulted in a low twinning activity with increased twin spacing and reduced twin thickness [203]. Unlike Cantor alloy, observation of deformation twins in both tension

and compression modes in $\text{Al}_{0.1}\text{CoCrFeNi}$ HEA could lead one to speculate that Al addition reduced SFE of the alloy in accordance with reduction in SFE observed in Cu with addition of Al [210] and in high Mn steels [211]. Kumar et al. [204] studied the effect of strain rate on deformation of $\text{Al}_{0.1}\text{CoCrFeNi}$ HEA and reported the presence of secondary nano-twins in the sample deformed at high strain rate whereas the sample deformed at quasi-static strain rate lacked secondary twinning. Gangireddy et al. [205,206] analyzed the effect of processing pathway through cold rolling and subsequent annealing in $\text{Al}_{0.1}\text{CoCrFeNi}$ HEA and reported that the retained deformation twins after cold rolling enabled excellent strength and ductility in the alloy. Similar enhancement in strength and ductility was also observed in $\text{Al}_{0.3}\text{CoCrFeNi}$ and $\text{Al}_{0.7}\text{CoCrFeNi}$ HEAs due to invocation of deformation twinning at larger strains [25,207–209]. Enhanced strength and work hardening observed in $\text{FeMn}_{30}\text{Co}_{10}\text{Cr}_{10}\text{C}_{0.5}$ interstitial HEA is also attributed to twinning in the FCC matrix along with martensitic phase transformation [212]. Deng et al. [213] developed a non-equiautomatic HEA $\text{Fe}_{40}\text{Mn}_{40}\text{Co}_{10}\text{Cr}_{10}$ HEA which showed excellent strength and work hardening ability comparable to high strength TWIP steels. Unlike equiautomatic Cantor alloy, activation of twinning at room temperature implies a lower stacking fault energy which enabled excellent hardening and ductility. Similarly, room temperature twinning was also observed after cold rolling in a VCrMnFeCoNi senary alloy [214]. Moreover, these

twinning were retained at room temperature, whereas additional twins were developed under deformation at cryogenic temperature. Zhang et al. [156] reported the presence of nano-twinning in the extended nanofibers that bridges the crack faces in the vicinity of crack tip which led to extrinsic resistance to crack propagation (Fig. 20). Recently, Sinha et al. [215] reported that twinning developed in the vicinity of a notch resulted in excellent hardening and improved the notch strength in $\text{Al}_{0.1}\text{CoCrFeNi}$ HEA compared to IN625, SS304 and Ti6Al4V alloys. In metastable HEAs having low SFE, which undergoes martensitic transformation under plastic strain, presence of deformation twinning in the transformed martensitic phase has been reported [216]. Twinning in transformed martensitic phase enables excellent work hardening and ductility in the metastable HEAs. However, detailed description of those mechanisms will be discussed in the next section. To conclude, careful selection of elemental composition while designing multicomponent alloys by reducing the SFE can trigger twinning as an additional strain accommodation mechanism, thereby enhance the work hardening, ductility and fracture resistance in those alloys even at room-temperature.

4.1.3. Transformation induced plasticity (TRIP)

Enabling strain induced martensitic transformation resulted in emergence of a new class of high performing steels called TRIP steels

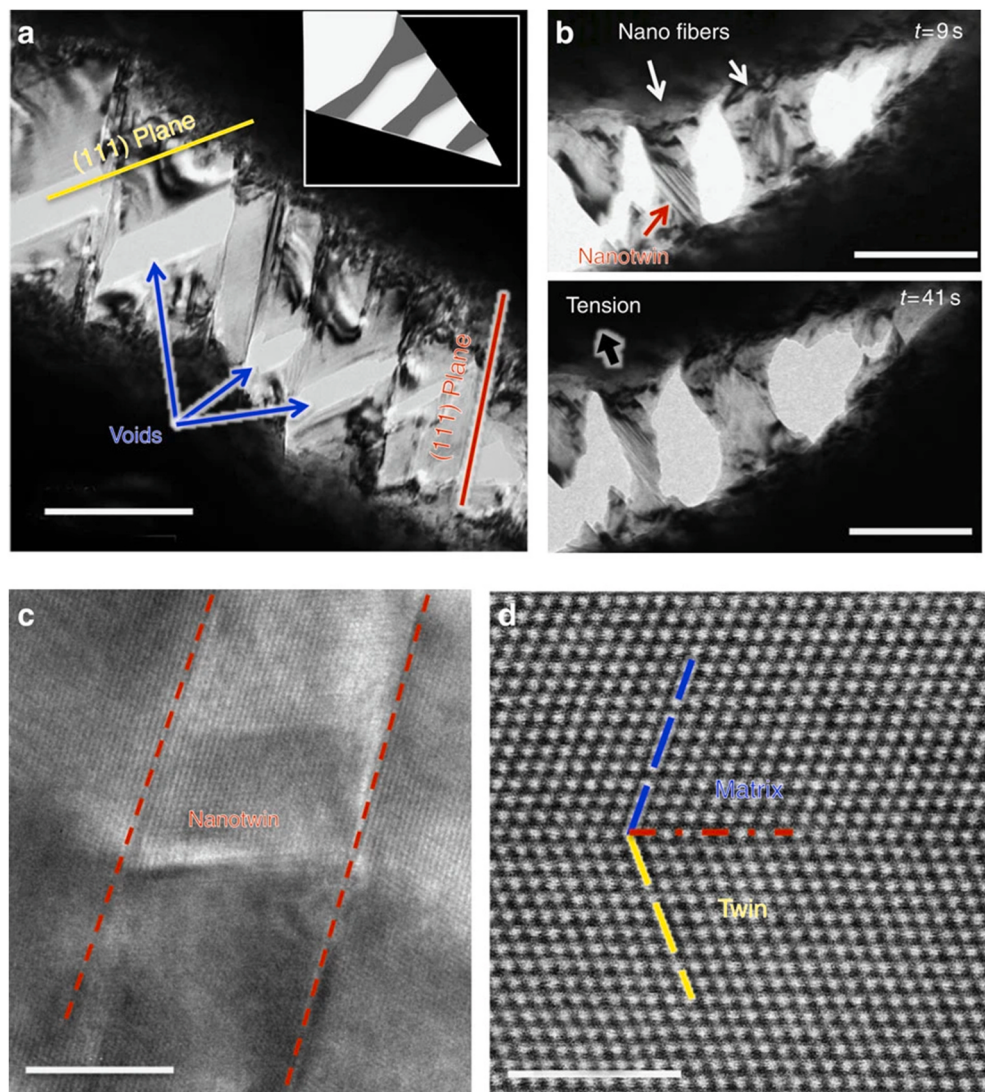


Fig. 20. (a–b) TEM images showing the presence of nano-twins in the nanofibers bridging the two faces of the crack tip when loaded under tension [156].

[217–228]. In TRIP steels, plastic straining is accommodated through transformation of retained austenite (γ) to ϵ (HCP) phase and α (BCC) phase under plastic deformation. Typical TRIP steels include austenitic ferrous alloys such as Fe–Ni–C, Fe–Mn–C, as well as some multiphase carbon steels with metastable retained austenite dispersed in a ferrite or martensite matrix. High strength and ductility achieved in TRIP steels inspired the materials research community to investigate the possibility of TRIP effect in HEAs.

TRIP HEAs have shown excellent combination of strength, ductility, hardness, fatigue and corrosion properties, reiterating the importance of cocktail effect in HEAs [35,39,59,88]. As shown in Fig. 17a, TRIP is activated in alloys having SFE $< 18 \text{ mJ m}^{-2}$. Transition of HEA composition from equiatomic regime to non-equiatomic regime gives the potential to control the deformation mechanisms by triggering TWIP and TRIP. Li and Raabe [229] have shown that careful alloy design strategy can be utilized to obtain strong and ductile HEAs by controlling the phase metastability as well as the progression of deformation mechanisms. An overview of such a strategy is shown in Fig. 21. Early evidence of TRIP in HEAs was reported when Li et al. [35] demonstrated that reducing the Mn content in $\text{Fe}_{80-x}\text{Mn}_x\text{Co}_{10}\text{Cr}_{10}$ HEA could change the mode of deformation from dislocation mediated plasticity (45 at.% Mn) to TWIP (40 at.% Mn) and further to TRIP (35 at.% Mn). The strength and ductility of $\text{Fe}_{50}\text{Mn}_{30}\text{Co}_{10}\text{Cr}_{10}$ TRIP HEA had improved by $\sim 140\%$ and $\sim 50\%$, respectively, compared to the single phase $\text{Fe}_{37}\text{Mn}_{45}\text{Co}_9\text{Cr}_9$ alloy. The initial stacking faults present in the FCC γ phase developed into a narrow HCP structure which on further deformation transformed to ϵ HCP platelets. Controlled annealing was later implemented to vary the grain size and initial ϵ phase fraction; a lower average FCC grain size and a higher volume fraction of ϵ phase led to improvement in both strength and ductility of the alloy [230]. Thermo-mechanical processing of $\text{Fe}_{50}\text{Mn}_{30}\text{Co}_{10}\text{Cr}_{10}$ TRIP HEA via friction stir processing (FSP) homogenized the microstructure which resulted in a fine-grained γ -dominant microstructure and improved the strength and ductility by $\sim 35\%$ and $\sim 15\%$, respectively, compared to the as-homogenized condition [36].

Nene et al. [38,59,60,88] further designed various TRIP HEAs based on the Gibbs's free energy change required for $\gamma \rightarrow \epsilon$ martensitic transformation and engineered the metastability of γ phase by adding minor elements such as Si, Cu and Al. The alloy design was based on the concept that transformation is favored when the metastability of the γ phase is high. Previous studies demonstrated that reducing Mn content and increasing Cr content in the alloy increases the metastability of the parent γ phase [183,231]. Furthermore, addition of Si also improves the

metastability of γ phase [231]. Based on the above insights, $\text{Fe}_{42}\text{Mn}_{28}\text{Co}_{10}\text{Cr}_{15}\text{Si}_5$ HEA was developed which has a metastable γ -dominant microstructure [59]. Additional thermo-mechanical processing led to extremely high strength of 1.15 GPa. Metastability based alloy design approach was further carried out to design other TRIP HEAs which showed excellent mechanical properties [38,60,88]. Thermomechanical processing via FSP enabled microstructural control in $\text{Fe}_{40}\text{Mn}_{20}\text{Co}_{20}\text{Cr}_{15}\text{Si}_5$ TRIP HEA where the initial phase fraction could be controlled by accurate selection of FSP parameters [38]. A hotter run (350 rpm) resulted in a ϵ -dominant microstructure whereas a colder run (150 rpm) resulted in a γ -dominant microstructure. Such a variation in the microstructure indicates the strain, strain rate, and temperature driven phase stability of the alloy. Unlike conventional alloys where an improvement in strength is achieved at the expense of ductility, $\text{Fe}_{40}\text{Mn}_{20}\text{Co}_{20}\text{Cr}_{15}\text{Si}_5$ showed a reversed strength-ductility behavior (Fig. 22a-b) which was attributed to the microstructural flexibility achieved upon thermo-mechanical processing. When 1.5 at.% Cu was added at the expense of Fe ($\text{Fe}_{40-x}\text{Mn}_{20}\text{Co}_{20}\text{Cr}_{15}\text{Si}_5\text{Cu}_{1.5}$), a γ -dominant microstructure was obtained irrespective of the processing condition which substantiates that Cu addition improved the stability of γ phase [88]. In addition to high strength (~ 1.1 GPa) and ductility ($\sim 42\%$) observed in $\text{Fe}_{38.5}\text{Mn}_{20}\text{Co}_{20}\text{Cr}_{15}\text{Si}_5\text{Cu}_{1.5}$ HEA, improved corrosion resistance was an added advantage. When minor amount of Al (1.0 at.%) was added to the $\text{Fe}_{40}\text{Mn}_{20}\text{Co}_{20}\text{Cr}_{15}\text{Si}_5$ HEA at the expense of Fe, the resulting alloy system showed an unexpected phase transformation response upon annealing (Fig. 22c), where the final phase fraction upon annealing dramatically changed with annealing temperature and time. Such a variation was attributed to the alteration of matrix metastability upon inter-competing precipitation and grain growth mechanisms where Al-rich precipitates precipitated out during annealing [60].

Sinha et al. [232] investigated the microstructure evolution in $\text{Fe}_{38.5}\text{Mn}_{20}\text{Co}_{20}\text{Cr}_{15}\text{Si}_5\text{Cu}_{1.5}$ HEA upon annealing after FSP and cold rolling with an interesting observation of phase reversion from $\epsilon \rightarrow \gamma$ phase upon controlled single step annealing after cold rolling. Similar phase reversal (bidirectional TRIP) observed in $\text{Fe}_{50}\text{Mn}_{30}\text{Co}_{10}\text{Cr}_{10}$ HEA was attributed to the near-zero positive value of SFE resulting in local variation in heating and micro mechanisms [233]. However, with a two-step annealing process, full recrystallization was achieved with a γ -dominant microstructure and led to grain growth upon further holding time. The mechanism of phase reversal was attributed to the formation of intrinsic stacking faults by vacancy accumulation during the recovery stage which acted as nucleation sites for martensitic ϵ phase [234]. Due to thermo-mechanical processing, the alloy upon FSP underwent

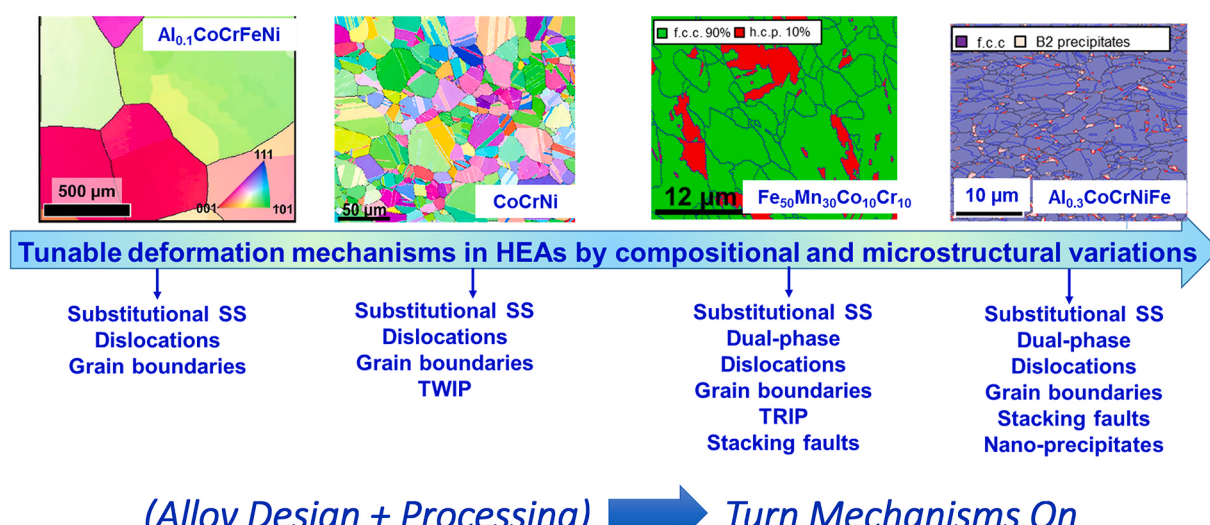


Fig. 21. Overview of deformation mechanisms that can be triggered by tuning the alloy composition in HEAs; from dislocation mediated plasticity to TWIP and further to TRIP (Adapted from Li and Raabe [229]).

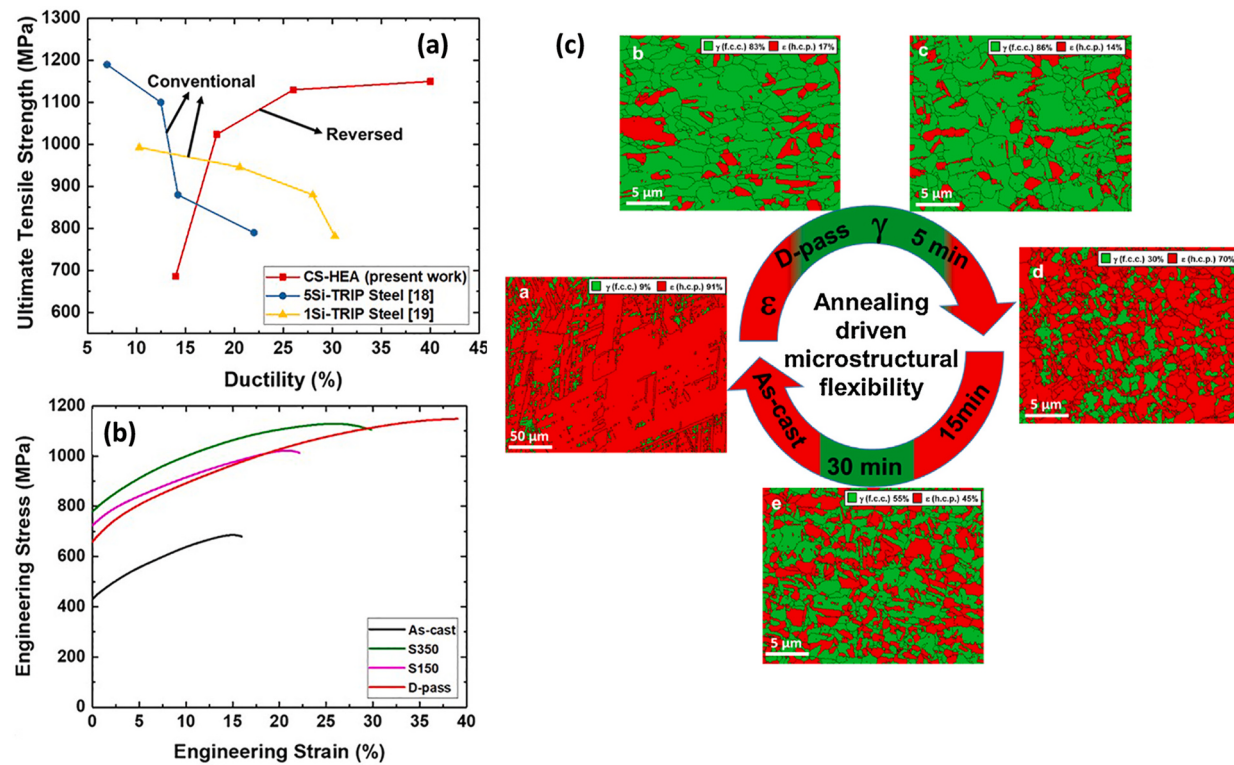


Fig. 22. (a) Reversed strength-ductility response obtained for $\text{Fe}_{40}\text{Mn}_{20}\text{Co}_{20}\text{Cr}_{15}\text{Si}_5$ TRIP HEA after FSP, compared to TRIP steels and (b) tensile stress-strain response of $\text{Fe}_{40}\text{Mn}_{20}\text{Co}_{20}\text{Cr}_{15}\text{Si}_5$ TRIP HEA as a function of FSP parameters (Nene et al. [38]), and (c) annealing-driven phase evolution in $\text{Fe}_{39}\text{Mn}_{20}\text{Co}_{20}\text{Cr}_{15}\text{Si}_5\text{Al}_1$ TRIP HEA at 650°C (Nene et al. [60]). (D-pass: Double pass FSP).

dynamic recrystallization due to synergetic effects of temperature, strain rate, and strain that resulted in a fine γ -dominant microstructure. However, cold rolling (strain controlled) resulted in a ϵ -dominant

microstructure with high dislocation accumulation. Hence, annealing of material after FSP led to further recrystallization and grain growth without changing the phase fraction, whereas direct annealing of

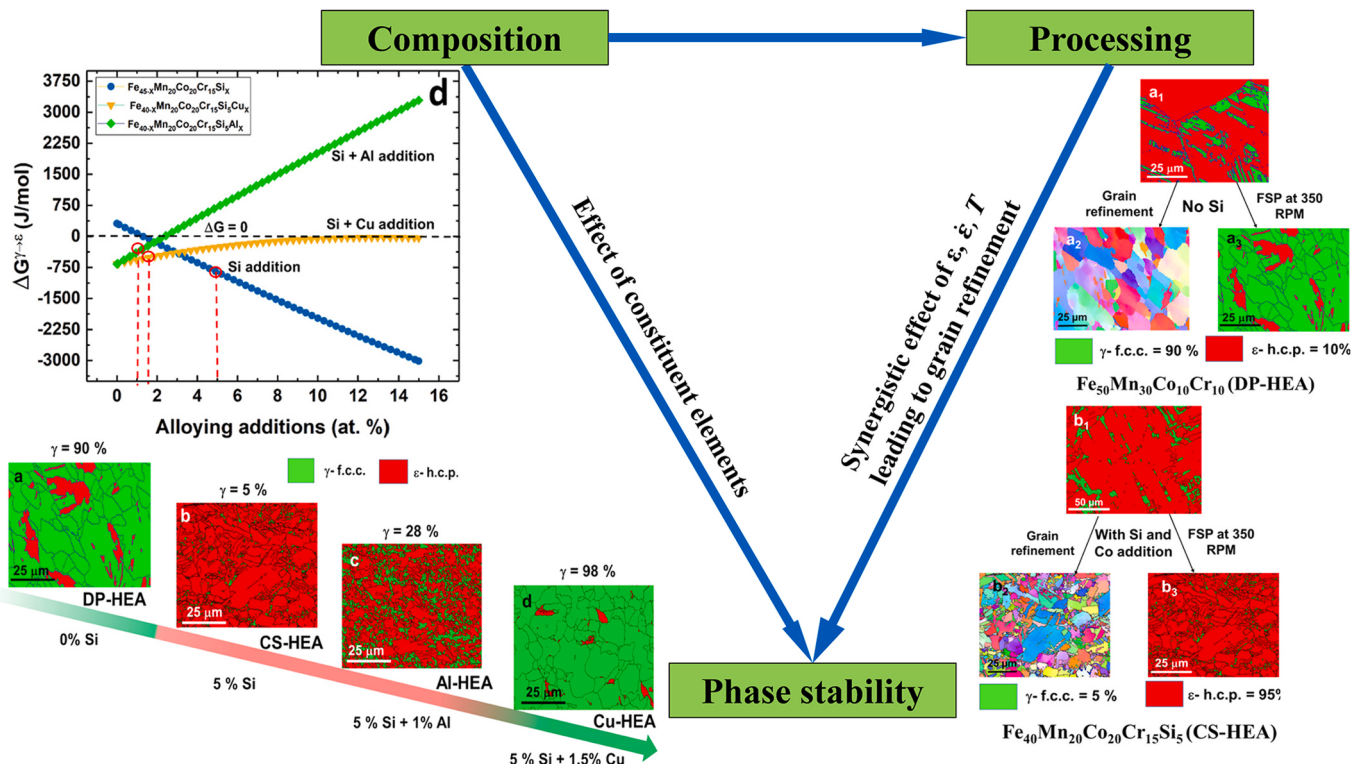


Fig. 23. Overview of composition-processing-phase-stability driven microstructural evolution in TRIP HEAs (adapted from Nene et al. [235]).

cold-rolled sample underwent phase evolution based on the extent to which recovery and recrystallization have set in. Above observations on microstructural evolution as a function of phase metastability driven alloy chemistry by addition of ϵ -phase stabilizers and subsequent thermomechanical processing with synergistic action of temperature, strain and strain rate gave rise to the concept of ‘composition-processing-phase stability’ governed microstructural flexibility in TRIP HEAs [235]. An overview of the concept is shown in Fig. 23.

Excellent work hardening due to TRIP facilitates the application of TRIP HEAs in fatigue applications. A γ -dominant ultrafine microstructure enabled excellent fatigue strength in $\text{Fe}_{38.5}\text{Mn}_{20}\text{Co}_{20}\text{Cr}_{15}\text{Si}_5\text{Cu}_{1.5}$ and $\text{Fe}_{42}\text{Mn}_{28}\text{Co}_{10}\text{Cr}_{15}\text{Si}_5$ TRIP HEAs [39,110]. Addition of Cu and subsequent FSP improved the stability of γ phase and thereby delayed the fatigue crack propagation due to excellent work hardening ahead of

crack tip through martensitic transformation, which led to exceptional fatigue strength of ~ 0.62 UTS, the best fatigue strength reported so far in HEAs [39,236]. However, the low cycle fatigue tests (LCF) in $\text{Fe}_{50}\text{Mn}_{30}\text{Co}_{10}\text{Cr}_{10}$ TRIP HEA reported lack of hardening, although the material showed extensive martensitic transformation under cyclic loading [237]. Additionally, lack of interaction of deformation mechanisms was observed and planarity of slip revealed partial reversibility of deformation mechanisms.

Sinha et al. [216] further studied the deformation mechanisms activated in the FCC and HCP phases in various TRIP HEAs. Intrinsic c/a ratio defines the activation of various deformation modes in ϵ (HCP) phase and it varied with the alloy chemistry. The c/a ratio was observed to vary as a function of processing condition and extent of deformation in all TRIP HEAs investigated [216]. Recently, Haridas et al. [238] have

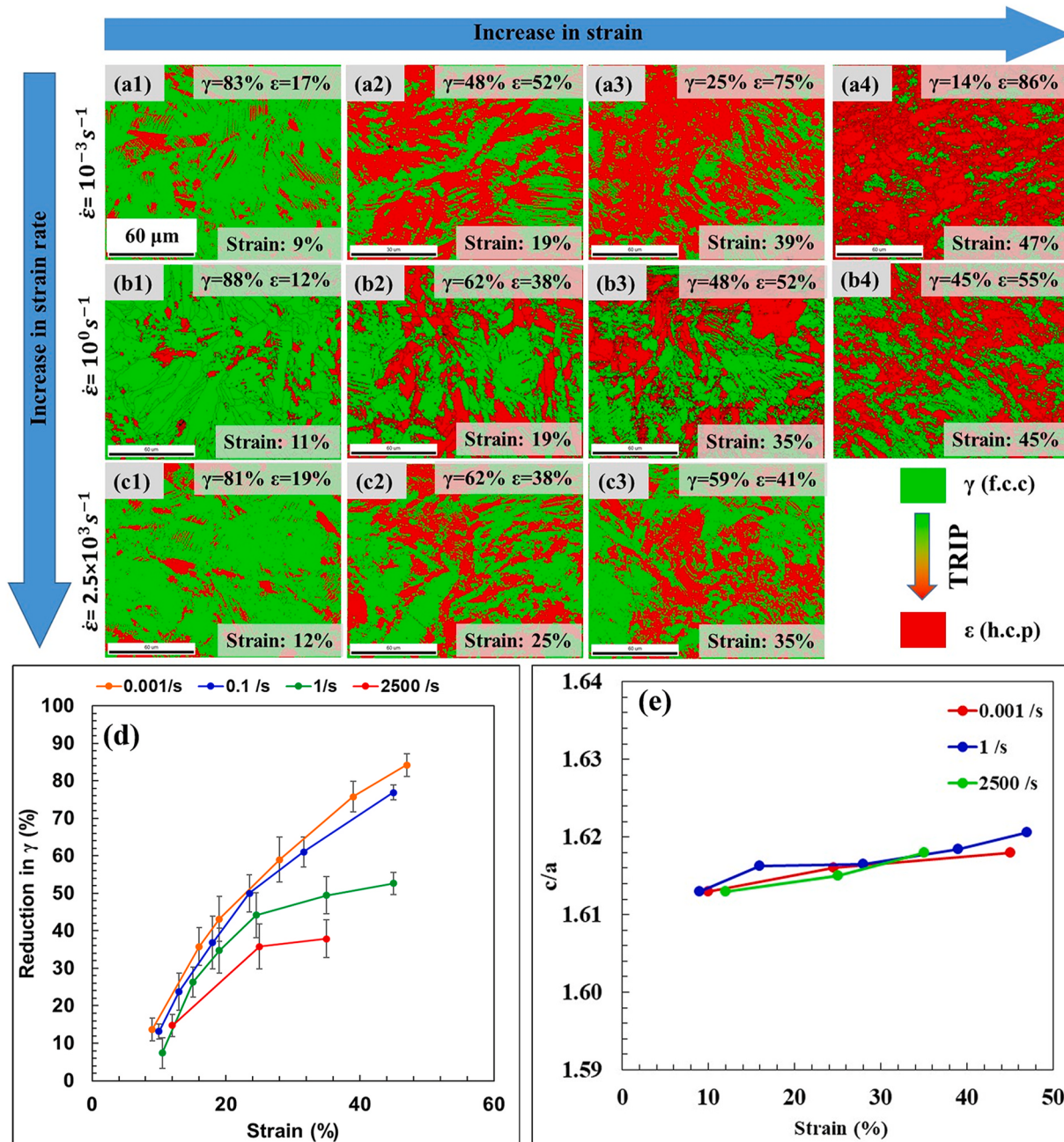


Fig. 24. Phase maps showing the transformation volume as a function of strain at strain rates (a1-a4) 10^{-3} s^{-1} , (b1-b4) 10^0 s^{-1} , (c1-c3) $2.5 \times 10^3 \text{ s}^{-1}$, (d) overall plot showing the percentage reduction in austenite phase with increase in strain at different strain rates, and (e) variation of c/a ratio as a function of strain and strain rate [238].

quantified transformation in Cu-HEA as a function of strain rate and established that the transformation volume reduces at higher strain rate at a constant strain level (Fig. 24 (a1-c3, d)). Additionally, they reported that the c/a ratio also evolves as a function of strain and strain rate; c/a ratio indicated marginal reduction with strain rate at a constant strain level (Fig. 24e). Unit cell volume measured using lattice parameters from XRD analysis revealed that martensitic transformation from γ (FCC) $\rightarrow \epsilon$ (HCP) phase is associated with a volume reduction. Such transformation volume changes are consistent with the results of Wei et al. [239] and Stanford and Dunne [240]. Additionally, less than ideal c/a ratio (1.633) was observed in most TRIP HEAs irrespective of the processing condition and deformation. Such lower values of c/a ratio enabled $<\text{c+a}>$ dislocations and twinning in ϵ (HCP) phase which favored strain accommodation along the c -axis, thus resulted in excellent work hardening and ductility in TRIP HEAs. Peculiar twin-bridging mechanism of extension twins was also observed where twins generate from a martensitic phase boundary at an inclination of 45–50°, changes their direction from the other boundary backwards to the initial boundary as shown in (Fig. 25). Further investigation on deformation mechanisms in Fe₄₀Mn₂₀Co₂₀Cr₁₅Si₅ TRIP HEA revealed the influence of metastability driven phase evolution, initial phase fraction, and processing condition on the work hardening and tensile response [241].

Analysis of deformation mechanism evolution using visco-plastic self-consistent model (VPSC) revealed the contribution of each deformation mechanism based on the initial phase fraction (Fig. 26). In a ϵ -dominant microstructure (S350 in Fig. 26d), strain accommodation in the initial deformation stage is via basal $<\text{a}>$, prismatic $<\text{c}>$ and pyramidal slip $<\text{c+a}>$ activities. As the deformation progresses, the individual contribution of basal and prismatic slip systems diminishes whereas pyramidal slip increases. However, in a dual phase microstructure having reasonable γ and ϵ phase fraction (S150 and D-pass in Fig. 26e-f), FCC slip activity prevails during the entire deformation process whereas the pyramidal $<\text{c+a}>$ slip activity increases with deformation as more ϵ phase fraction evolves. Similar to S350 condition, basal and prismatic slip activities in the initial and transformed ϵ martensitic phase deteriorates with deformation. Further, evaluation of critical value of shear stress on leading and trailing partials which facilitate stacking fault formation, revealed that those grains having their $[0\bar{1}2]$ orientation parallel to the tensile axis of loading favor γ (FCC) $\rightarrow \epsilon$ (HCP) martensitic transformation during the initial deformation stages when compared to other crystallographic orientations.

Frank et al. [242] used neutron diffraction techniques to experimentally investigate the evolution of deformation mechanisms in Fe₄₀Mn₂₀Co₂₀Cr₁₅Si₅ TRIP HEA. SFE of the TRIP HEA was determined to

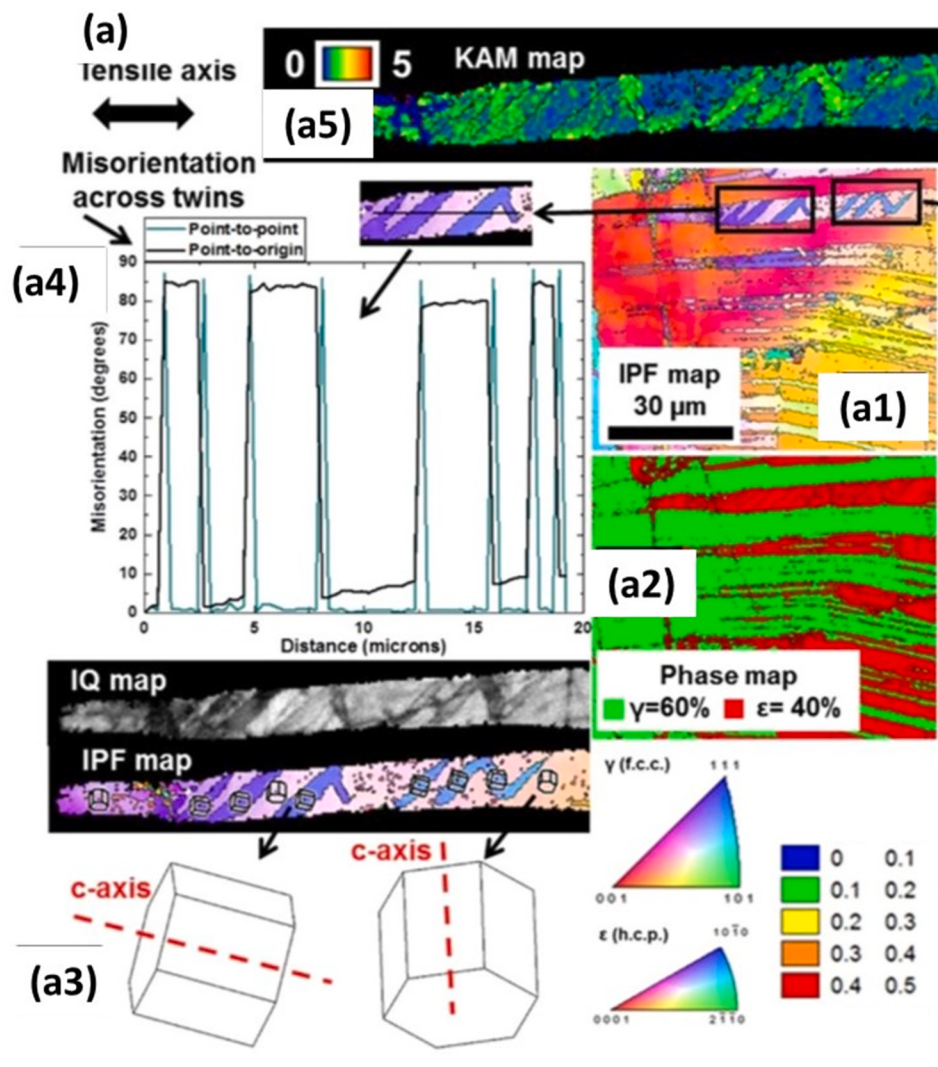


Fig. 25. (a) Unique twin-bridging mechanism observed in Fe_{38.5}Mn₂₀Co₂₀Cr₁₅Si₅Cu_{1.5} TRIP HEA, (a1) IPF map showing the twins which are highlighted in black box, (a2) phase map corresponding to (a1), (a3) unit cell orientation in the ϵ plate and the twins indicating twin orientation towards the tensile loading axis, (a4) misorientation profile along the twins, and (a5) KAM map of the ϵ plate and the twins [216].

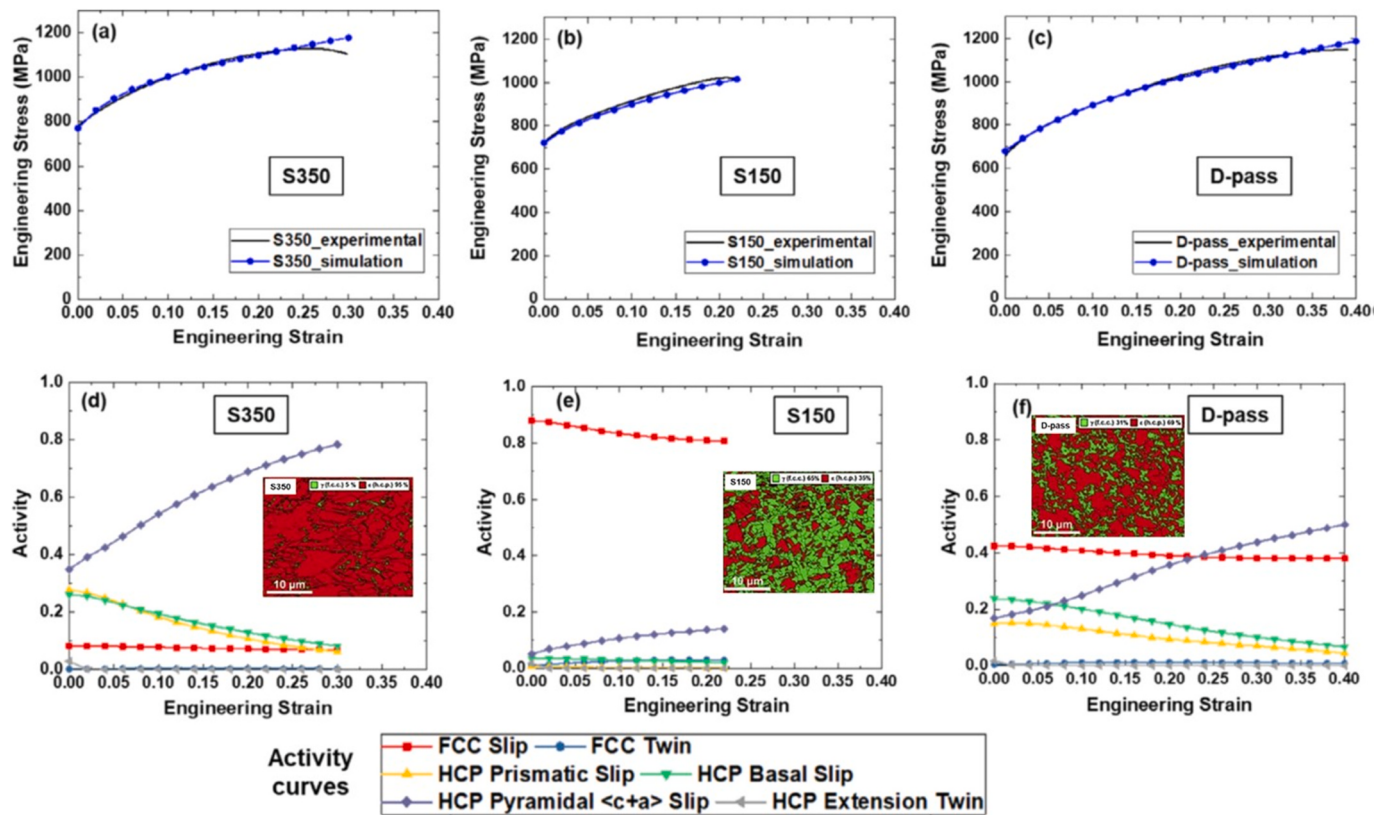


Fig. 26. VPSC simulation results obtained for $\text{Fe}_{40}\text{Mn}_{20}\text{Co}_{20}\text{Cr}_{15}\text{Si}_5$ TRIP HEA. (a–c) Comparison of experimental and VPSC model stress-strain responses for different FSP conditions, and (d–f) corresponding individual deformation mode activity as a function of strain. Inset in figures (d–f) indicate the phase fraction after FSP [241]. (D-pass: Double pass FSP).

be as low as 6.31 mJ m^{-2} . However, under tensile deformation, only a marginal fraction of transformation was obtained in $\text{Fe}_{40}\text{Mn}_{20}\text{Co}_{20}\text{Cr}_{15}\text{Si}_5$ TRIP HEA compared to a similar study on $\text{Fe}_{50}\text{Mn}_{30}\text{Co}_{10}\text{Cr}_{10}$ TRIP HEA [243] with the latter having higher initial γ phase fraction. Fu et al. [243] reported that the deformation in $\text{Fe}_{50}\text{Mn}_{30}\text{Co}_{10}\text{Cr}_{10}$ progresses through 4 different stages. Initial stage was characterized by the development of stacking faults through Shockley partial dissociation which resulted in generation of ϵ platelets and thus initiated martensitic transformation. On further loading, with persistent transformation, extension twins were developed in the transformed martensitic phase rather than slip activity, which was evidenced by the bifurcation of $\{00\bar{2}\}$ and $\{10\bar{3}\}$ diffraction peak intensities in both longitudinal (LD) and transverse (TD) directions as well as an increase in $\{10\bar{1}\}$ peak intensity along LD. Later stage of deformation was accompanied by development of compression twins and slip activity in the transformed martensitic phase. Similar evidence of lattice reorientation and the presence of extensive twinning activity was also observed in $\text{Fe}_{40}\text{Mn}_{20}\text{Co}_{20}\text{Cr}_{15}\text{Si}_5$ HEA [242]. Additionally, with increase in deformation, the c/a ratio reduced from 1.619 to 1.594; the reduction was rapid during the initial stage ($\sigma < 100 \text{ MPa}$) and final stage of deformation ($\sigma > 1100 \text{ MPa}$) due to dominant basal slip activity with an increase in a and non-basal $\langle c+a \rangle$ slip activity with a decrease in c , respectively (Fig. 27 (a1-a3)). Extent of straining along c -axis was higher than that along a direction in the final stage of deformation, which evidenced the dominance of non-basal slip activity in the ϵ martensitic phase (Fig. 27 b-c). In a recent study on $\text{Fe}_{40}\text{Mn}_{20}\text{Co}_{20}\text{Cr}_{15}\text{Si}_5$ HEA, Frank et al. [244] quantified the contribution of stacking faults towards work hardening and determined that the contribution is $\sim 50 \text{ MPa}$ and $\sim 250 \text{ MPa}$ in as-cast and FSP conditions, respectively. Hence, tailoring the stability of the metastable γ phase through careful selection of alloying components could trigger various deformation modes including TRIP, twinning and

non-basal slip modes in the ϵ phase, thus result in excellent strength-work hardening-ductility synergy in metastable TRIP HEAs.

4.2. Deformation mechanisms in BCC based HEAs

Although deformation mechanisms in FCC based HEAs have been greatly investigated extensively in literature, a significant level of study on deformation mechanisms in BCC based HEAs is lacking, particularly in tension. BCC based solid solutions are characterized by very high strength ranging from 900 to 1350 MPa and limited ductility [245,246]. It is well established in literature that the mechanical response of BCC HEAs can be tuned by varying valence electron concentration (VEC). A brief description of various factors contributing to deformation mechanism in BCC HEAs is given in the following sections.

4.2.1. Valence electron concentration (VEC)

For a material to be ductile, the stress required for dislocation nucleation should be lower than the stress required for failure processes like void nucleation and crack initiation; VEC controls the relative magnitude of ideal cleavage strength and shear strength. In essence, this is the hierarchical arrangement of mechanisms so that plasticity precedes fracture. Qi et al. [247] demonstrated that ductility of BCC-based HEA can be enhanced by tuning valence electron concentration (VEC) by careful choice of constituent elements, thereby reducing the ideal shear strength. It has been observed that by lowering the valence electron in Mo, Nb alloys, ideal shear strength of the material is lowered which in turn makes the material readily deformable and more ductile [248]. Transition from high strength-low ductility paradigm [246] to low strength-high ductility combination [249,250] can be achieved by lowering the VEC from 5 to 4.5. Based on valence electron theory, Sheikh et al. [251] have proposed that a ductile BCC based RHEA can be

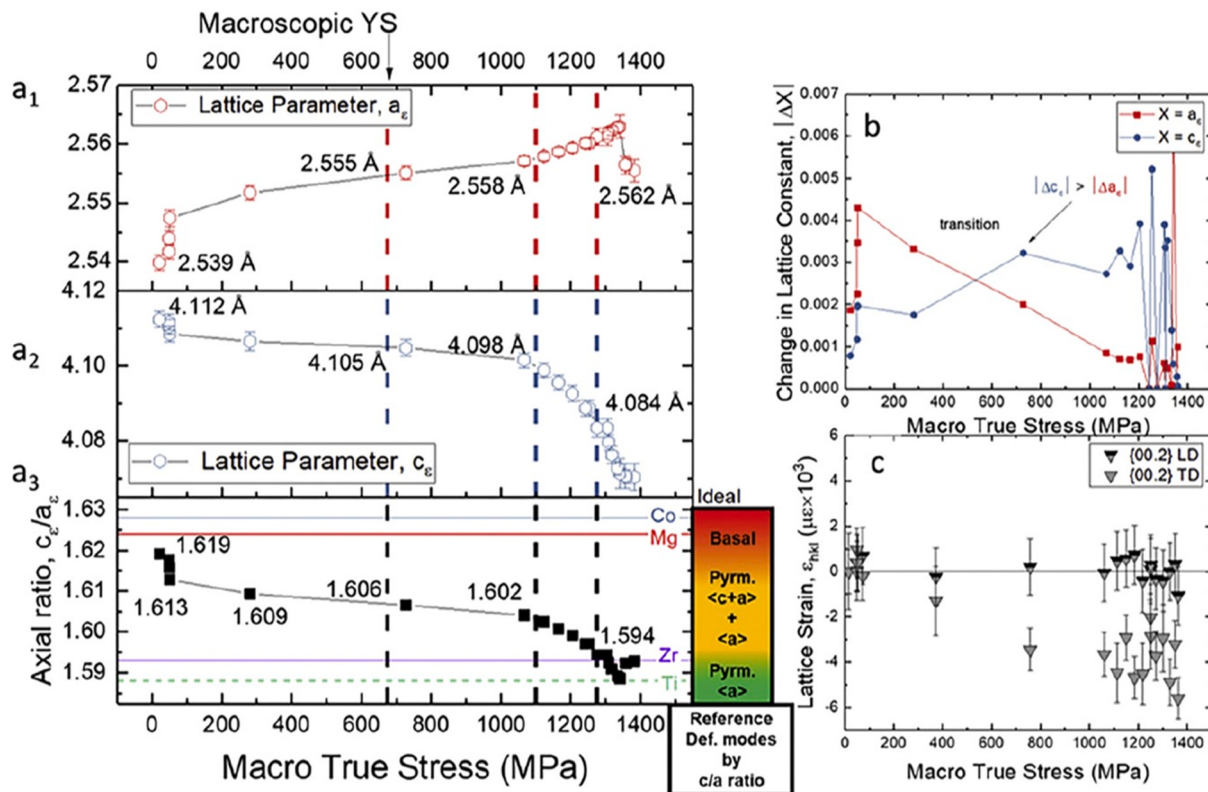


Fig. 27. Evolution of lattice parameters in the martensitic phase in $\text{Fe}_{40}\text{Mn}_{20}\text{Co}_{20}\text{Cr}_{15}\text{Si}_5$ TRIP HEA. (a₁) lattice parameter a_1 , (a₂) lattice parameter c , (a₃) c/a ratio, (b) change in the value of lattice constants a and c , and (c) lattice strain evolution along the longitudinal and transverse direction obtained from {00.2} family of basal oriented grains [242].

obtained by substituting alloying elements from group VI or group V with elements from group V or group IV, thereby achieving a reduction in the number of valence electrons. Fig. 28a from Sheikh et al. [251] summarizes the effect of VEC on the ductile-brittle transition behavior of BCC based HEAs. However, they suggested that one should ensure the formation of BCC solid solution in RHEAs before manipulating VEC by tuning the composition. As briefed earlier, solid solutions can be created by controlling the atomic size mismatch, δ ($\delta \leq 0.066$) and enthalpy of mixing, ΔH_{mix} ($\Delta H_{\text{mix}} \geq -11.6 \text{ kJ mol}^{-1}$). A design approach to develop

ductile BCC-based HEAs by controlling three parameters VEC, δ , and ΔH_{mix} proposed by Sheikh et al. is shown in Fig. 28b.

4.2.2. Activation volume

Generally, BCC alloys have two temperature-stress dependent regimes. At low temperature/high stress regime, activation volumes are generally low ($10 b^3$). In this regime deformation is mainly controlled by screw dislocation subjected to Peierls friction force. However, at low stress/high temperature regime kink pair is effectively characterized by

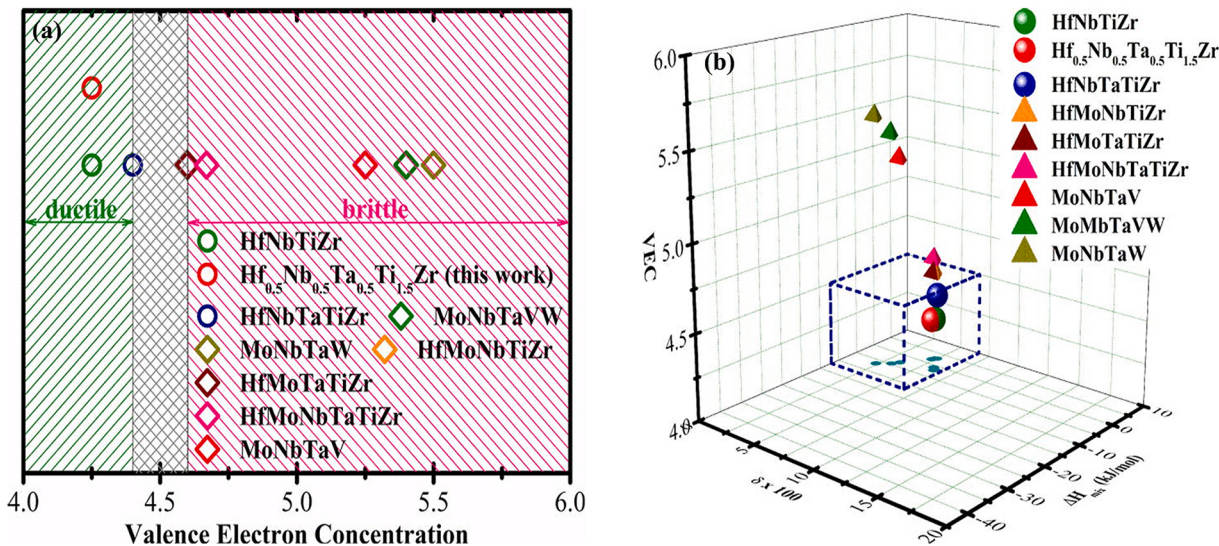


Fig. 28. (a) Dependence of VEC on the ductility in BCC-based RHEAs, and (b) a design approach proposed to obtain ductile BCC-based RHEA solid solutions by carefully tuning VEC, δ , and ΔH_{mix} (Sheikh et al. [251]).

uniform motion of dislocations [252]. Deformation mechanism of an alloy is first assessed by activation volume calculation. From stress relaxation tests one could evaluate the activation volume from the value of stress variation during relaxation as per the following equation [253]:

$$\Delta\sigma(t) = \frac{-MkT}{V_a^*} \ln\left(1 + \frac{t}{c}\right) \quad (18)$$

where V_a^* is activation volume, T is temperature, k is Boltzmann constant and c is a time constant. Lilensten et al. [253] performed single and multi-relaxation tests on annealed equiatomic TiZrHfNbTa HEA to understand the deformation mechanism activated during deformation. Activation volume for the alloy was determined to be $25 b^3$ to $40 b^3$ which is strain independent. Moreover, similarity in the values of apparent and physical activation volume for the alloy indicated that the hardening process hardly modifies the deformation mechanism [253]. Monotonic loading and load relaxation compression tests performed in HfNbTaTiZr HEA by Couzinie et al. [254] revealed a monotonic reduction in activation volume from $50 b^3$ – $30 b^3$ from initial stages of deformation towards failure. Such a reduction in activation volume is related to Peierls stresses experienced by screw dislocations having Burger's vector $b = a/2 <111>$ in early stages of deformation and dislocation band formation in the later stages.

4.2.3. Dislocation related deformation mechanism

Although there is lack of availability of extensive research on dislocation mechanisms in BCC based HEAs, this section is intended to provide a brief description on dislocation mediated plasticity in BCC HEAs. Study of TiZrNbHfTa BCC HEA showed that screw dislocation glide primarily controls the deformation [254]. In another study on

NbMoTaW BCC HEA, nano-pillar compression tests revealed that deformation is mainly due to lattice resistance to dislocation motion [255]. Lilensten et al. [253] studied deformation mechanisms in a homogenized single-phase BCC HfNbTaTiZr HEA deformed to a plastic strain level of 0.0265. Features related to dislocation glide were observed in the SEM micrographs of the deformed sample. TEM analysis revealed presence of two slip systems which were identified as screw dislocations with $a/2 <111>$ orientation parallel to {110} and {112} planes (Fig. 29). The deformation is mainly characterized by the glide of screw dislocations. Measurement of activation volume suggested high Peierls stress in HfNbTaTiZr at room temperature. High yield stress reported for the alloy was associated with the interaction of dislocations with the solute atoms whereas high strain hardening in the material was attributed to higher dislocation density and formation of deformation bands [253]. Similar results were also reported by Dirras et al. [249] for HfNbTaTiZr HEA. Atomistic simulation performed by Rao et al. [256] for BCC multicomponent HEAs revealed the influence of short range order due to local concentration fluctuations which acted as short range obstacles for dislocation motion. Podolskiy et al. [257] studied compression behavior and flow stress sensitivity in $Ti_{30}Zr_{25}Hf_{15}Nb_{20}Ta_{10}$ alloy in order to accomplish a complete overview of the mechanical behavior in the low temperature regime. The alloy exhibited excellent ductility of ~20% above 77 K irrespective of temperature, whereas yield strength improved with decrease in temperature. Thermally activated plasticity in the alloy at lower temperatures was attributed to the mechanism of kink pair formation along the dislocation line rather than the possibility of hindrance to dislocation due to local short-range clustering. Strain rate dependence on the plastic deformation of quinary HfNbTaTiZr single phase BCC HEA [258]

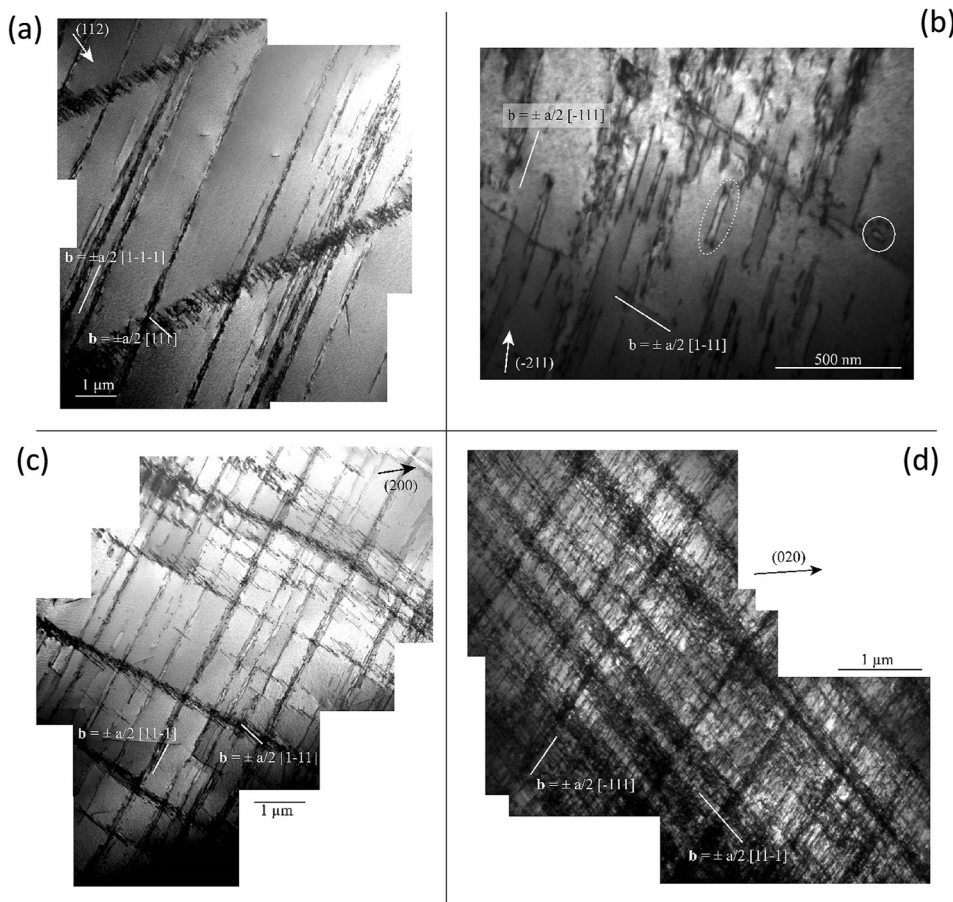


Fig. 29. Bright field TEM micrographs of HfNbTaTiZr HEA (inset: diffraction vector $g = 110$) strained to (a) and (b) $\epsilon_p = 0.0022$ indicating two sets of screw dislocations with $b = a/2 <111>$ in strained solid solution, (c) $\epsilon_p = 0.0289$, and (d) $\epsilon_p = 0.1012$ [253].

revealed intense slip activity and macroscopic shear band formation at strain rate of 1 s^{-1} , whereas at strain rate of 4.53 s^{-1} deformation was localized and heterogeneous within the grains, including observation of intense lattice rotations. Senkov et al. [259] studied the cold rolling behavior of HfNbTaTiZr HEA with 65% thickness reduction. Although the flow stress followed the Taylor hardening law, large adiabatic shear band formation in the rolled samples led to failure of the specimen. Nevertheless, achievement of large reduction in thickness during cold rolling keeps the alloy among the limited number of BCC HEAs with tensile ductility.

Adding heterogeneities to the BCC HEAs can be an effective way to enhance strain hardening along with the strength of the material. Precipitation is generally not exploited in BCC HEAs due to low ductility of the matrix; however, the precipitate precursors have been utilized. In a recent study [260], addition of small amount of oxygen (2 at %) in TiZrHfNb BCC HEA resulted in the formation of (O,Ti,Zr) complexes. Interaction of dislocations with these complexes resulted in dislocation pinning which enhanced the strength and work hardening of the alloy.

4.2.4. TRIP

Metastability based engineering approach has been widely used in FCC HEAs to promote plastic deformation via TRIP [35]. Huang et al. [261] utilized similar approach in BCC HEAs to explore the possibility of improving ductility. By varying Ta concentration from 1 to 0.4 (mole fraction) in a TaHfZrTi HEA, composition varies from single phase solid solution in equiatomic quaternary TaHfZrTi HEA to dual-phase BCC + HCP microstructure for a Ta concentration of $x = 0.4$ (Fig. 30 (a)). With a decrease in Ta content from $x = 1$ to $x = 0.4$, uniform ductility improved from mere 4%~27% (Fig. 30 (b)) upon the activation of BCC→HCP TRIP. Increase in work hardening rate with deformation in alloys with lower Ta content also substantiates the invocation of TRIP

(Fig. 30 (c)). Similarly, Lilenstein et al. [262] proposed an alloy design strategy to control the metastability in Ti containing BCC RHEAs based on the strategy implemented by Abdel-Hady and Morinaga [263] in β -Ti alloys by tuning the alloy composition in order to bring the alloy position close to $M_s = RT$ line in $\overline{B_0} - \overline{M_d}$ diagram, where M_s is the martensitic transformation temperature, $\overline{B_0}$ is the bond order and $\overline{M_d}$ is the energy associated with the d-orbitals. Upon deformation, the microstructure of optimized composition of Ti-rich HEA Ti₃₅Zr_{27.5}Hf_{27.5}Nb₅Ta₅ revealed the formation orthorhombic α'' martensite phase. High hardening and ductility achieved in the alloy were attributed to interplay of two competing mechanisms, viz., dynamic Hall-Petch effect in which formation of new interfaces due to TRIP effect hinder the dislocation glide, and dynamic composite effect due to accumulation of necessary dislocation near the interfaces. Similar design strategy was employed by Eleti et al. [264] to activate TRIP by designing a Ti-rich BCC HEA with composition Ti₃₈Zr₂₅Hf₂₅Ta₁₀Sn₂ which exhibited BCC (β) to HCP (α') martensitic transformation. TEM analysis of the alloy after deformation revealed that the deformation in BCC phase was characterized by dislocation slip whereas transformed HCP phase further deformed by twinning or dislocation slip. Hence, fine tuning of alloying element concentration in a multicomponent RHEAs to engineer the metastability of the matrix phase enable excellent hardening and ductility in the alloy, thereby creating a balance in mechanical properties.

4.3. Deformation mechanisms in HCP HEAs

Even though the compositional space available for high entropy alloys is wide, their matrix phase window is mostly restricted to FCC, BCC, or HCP based crystal structures. Mostly, HEAs adopt either FCC or BCC crystal structures, formation of HCP crystal structure is rather rare. BCC

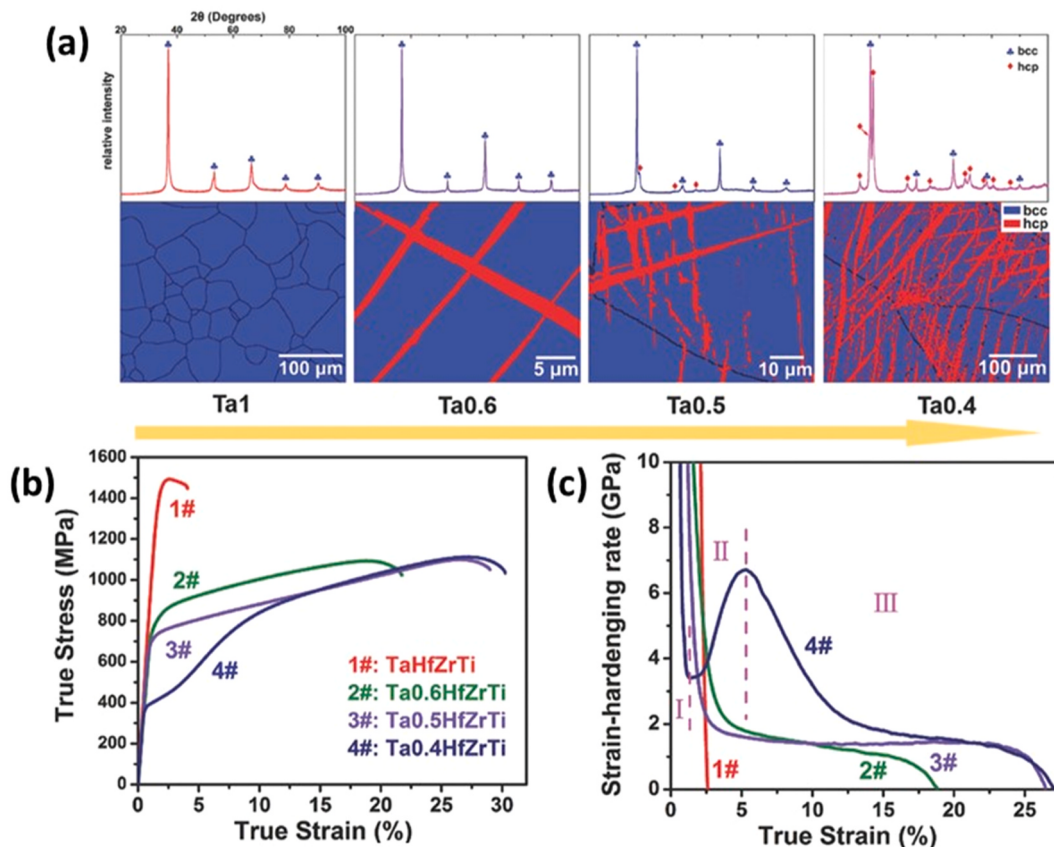


Fig. 30. (a) XRD patterns and EBSD micrographs showing the HCP phase evolution with a decrease in Ta content from $x = 1$ to $x = 0.4$, (b) tensile stress-strain curve for Ta_x HEAs at room temperature, and (c) corresponding work hardening curves (Huang et al. [261]).

HEAs possess high strength but limited ductility whereas FCC HEAs show extensive plastic ductility at low strength. HCP HEAs are desirable as they are expected to have a combination of both high strength and reasonable ductility. Zhao et al. [265] discussed mechanical behavior of HCP based HEA GdHoLaTbY which showed a compressive fracture strength of 880 MPa and 21.8% plastic deformation till failure. Rogal et al. [266] studied single phase HfScTiZr HEA with a HCP crystal structure which exhibited a Widmanstatten structure. As-cast alloy exhibited compressive strength of 1802 MPa with indication of post deformation shear band formation and presence of high dislocation density. Zhang et al. [267] performed compressive deformation study on a CuYZrTiHf dual phase HEA consisting of HCP matrix and ordered BCC phase. Microstructure of the alloy consists of HCP dendrites with BCC interdendritic regions. CuYZrTiHf HEA showed compressive strength of 1340 MPa and plastic strain of 13.2%. Easy dislocation glide in the HCP solid solution provided plasticity to the alloy when deformed. Cameron et al. [268] used high pressure synthesis to stabilize HCP phase in CrMnFeCoNi HEA, where decompression led to the formation of metastable FCC-HCP mixture. Mechanical response of the alloy was not reported. A detailed deformation study on pure HCP HEAs is still lacking. However, a detailed description of deformation mechanisms in dual phase (FCC + HCP) Fe₄₀Mn₂₀Cr₁₅Co₂₀Si₅ HEA is available [37,38]. HCP dominant microstructure obtained after FSP as well as AM showed excellent combination of strength and ductility. Frank et al. [242,244] performed in-situ neutron diffraction study to understand the deformation mechanism in the alloy. Stress is partitioned between both FCC and HCP phases. Excellent ductility obtained for the alloy is attributed to non-basal $<\text{c+a}>$ pyramidal slip and deformation twinning achieved in the alloy at larger strains. Detailed discussion on the deformation mechanism in Fe₄₀Mn₂₀Cr₁₅Co₂₀Si₅ HEA was already provided in section 4.1.3.

5. Mechanical properties of high entropy alloys – are they competitive with conventional engineering alloys?

In order to qualify an HEA for structural applications, an evaluation of the mechanical performance of the material is critical. Based on the mode of loading and type of engineering application, one has to establish tensile and compressive strengths, fatigue strength, fracture toughness, hardness, and wear of the alloy. As mentioned earlier, it is convenient to follow Ashby's materials selection for mechanical design approach [269] which lists the criterion as (a) stiffness-limiting design, (b) strength-limiting design, (c) toughness-limiting design, (d) fatigue-limiting design, and (e) creep limiting design. The stiffness-limiting design depends only on the elastic constants and HEAs don't exhibit any particular advantage on this front. Additionally, no plasticity is involved in this design approach. None of the HEA core effects directly or indirectly has a major impact on stiffness related discussion, so we do not consider this further.

Since HEAs are a class of alloys that have been touted as having potential for excellent multiple properties in synergy owing to the *cocktail effect* [82], they can be a good replacement for conventional high-performance alloys such as stainless steels, TRIP steels, TWIP steels, and nickel based superalloys. George et al. [14] have given a deep insight into the mechanical properties of HEAs in their detailed review. This section deals with exploring the mechanical properties of HEAs for four deformation-based design approaches that rely on tensile strength, fracture toughness, fatigue, and creep.

5.1. Tensile strength

In order to assess the strength of HEAs, the uniaxial strength data available in literature will be made use of, since the data available under other loading conditions is limited. Extreme structural applications need strength-ductility synergy along with exceptional performance at high temperature, as well as cryogenic temperature. Excellent strength and

ductility reported in HEAs and CCAs at extreme thermal conditions make them potential candidates for such applications [6,7,185,246]. Note that the mechanical performance of HEAs can be controlled by engineering the microstructure by appropriate selection of elemental composition and grain size [127,131,270], post-annealing heat treatments [22–24,134,136], and thermo-mechanical processing such as cold rolling, warm rolling, as well as FSP [36,235,271]. The thermo-mechanical processing can be a very strong component for HEAs because of the metastability and this aspect is discussed in the next sub-section. Although the initial studies had concentrated on single phase HEAs and MEAs such as CoCrFeNiMn and CoCrNi, respectively, recent studies were performed on non-equiautomic multi-phase-multi-component alloy systems to improve the strength and to overcome the strength-ductility tradeoff.

Although early research was carried out on single phase FCC HEAs such as CoCrFeMnNi and Al_{0.1}CoCrFeNi HEAs which displayed excellent strength and ductility at both room temperature and cryogenic temperature [97,185,272], performance of BCC based HEAs were also explored. Zhou et al. [68] studied the influence of varying alloy composition on the performance of a BCC based HEA. Increasing the amount of Ti in Al_xCoCrFeNiTi_x alloy has a significant effect on the mechanical properties and microstructure. Varying x from 0 to 1.5 changed the microstructure from a single phase to multiphase. Composition with $x = 0.5$ resulted in the best strength-ductility combination. Similarly, changing the volume fraction of Al in Al_xCoCrFeNiCu HEA changed the microstructure from single phase FCC to single phase BCC [89] (Fig. 31) with an increase in strength/hardness. Hence, selection of constituent elements and their proportion is one key element in deciding the final strength of the alloy.

Gwalani et al. [127] have shown that the strength of Al_{0.3}CoCrFeNi HEA can be tuned within a large range by coupling the effects of thermo-mechanical heat treatment, precipitation strengthening, and Hall-Petch effect. Possibility to obtain such a wide range of strength value relies upon the richness of phases in the phase diagram, where careful heat treatment can produce a microstructure with a combination of multiple phases which includes FCC, BCC, L1₂, B2 and σ . Mechanical property can be altered by changing the transformation pathways; precipitation annealing following cold rolling of homogenized alloy resulted in a combination of FCC, B2, and σ phases whereas incorporating a recrystallization step before annealing resulted in a FCC phase with L1₂ ordered precipitates distributed homogeneously inside the FCC matrix (Fig. 32a). Such variation in microstructure was also reflected in the strength and ductility response of the HEA (Fig. 32b). Final mechanical response can be controlled by accurate selection of heat-treatment conditions to precipitate out strengthening precipitates such as L1₂ and B2, thereby improving the strength of the alloy [23].

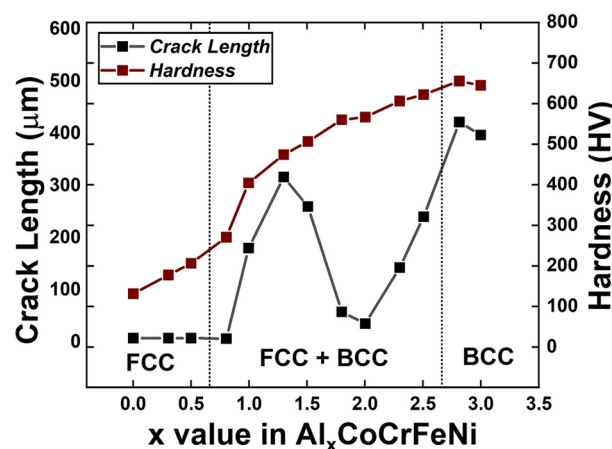


Fig. 31. Phase evolution and variation in Vickers hardness and crack length upon varying Al content in Al_xCoCrFeNiCu HEA [89].

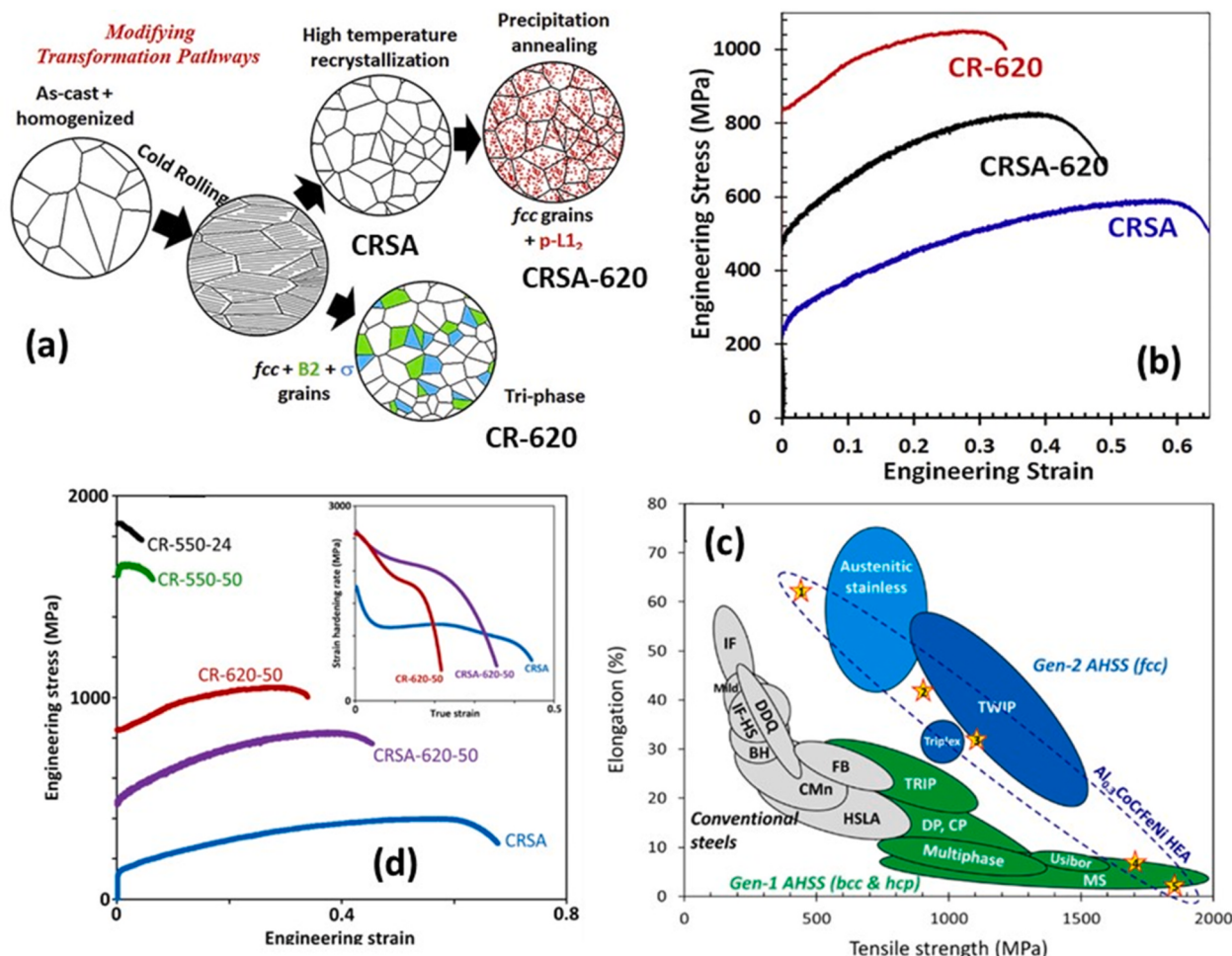


Fig. 32. (a) Changing the transformation pathways in $\text{Al}_{0.3}\text{CoCrFeNi}$ to vary the final microstructure and mechanical properties, (b) variation in strength and ductility when subjected to different heat treatment conditions in (a), (c) engineering the strength from 160 MPa to 1800 MPa using different thermos-mechanical heat treatments, and (d) strength-ductility spectrum that can be achieved in $\text{Al}_{0.3}\text{CoCrFeNi}$ HEA [23].

Ability to tune the microstructure in $\text{Al}_{0.3}\text{CoCrFeNi}$ HEA enabled one to engineer the strength from 160 MPa to 1800 MPa, an enormous 1025% improvement in strength (Fig. 32c-d [24]). Choudhuri et al. [273] have shown that the strength can be further improved via deformation twinning in $\text{Al}_{0.3}\text{CoCrFeNi}$ HEA reinforced with intermetallic compounds. Similar studies on tailoring the final mechanical response of the alloy by varying the microstructure via grain boundary strengthening and precipitation strengthening have also been reported in Al/Ti containing CoCrFeNi HEA [19], AlCoCrFeNi_x eutectic alloy system [274, 275], as well as in other HEA systems [276–282]. Hence to conclude, the mechanical strength of multicomponent alloys can be tailored vastly by controlling the microstructural evolution through careful design of thermo-mechanical heat treatment conditions.

Mishra et al. [283–285] have proposed FSP as a single thermo-mechanical process where strain, strain rate and temperature act in synergy to drastically vary the microstructure and mechanical properties of alloys ranging from Al, Mg, Ti based alloys, nickel-based alloys and steels [286–296]. Based on the processing parameters used, FSP can result in fine-grained and ultra-fine-grained microstructures which improve the mechanical performance of the material [285]. Friction stir processing has also been implemented in HEAs to improve their strength and ductility [128,297]. Recently, Nene et al. [36,59,60, 88] have used FSP as a thermo-mechanical processing tool to vary the grain size, microstructure and phase fraction in various TRIP HEAs and obtained excellent strength-ductility synergy.

George et al. [14], in their review on mechanical properties of HEAs,

have collected the data from relevant literatures on HEAs and integrated all the data into multiple room temperature tensile strength-total elongation plots based on the microstructure and phases present (Fig. 33 (a–d)). One has to note that the data presented was not normalized with respect to the grain size, initial dislocation density, thermo-mechanical processing route, as well as precipitation content. Additionally, in each of the HEAs, further refinement of properties could be achieved by minor adjustment in composition and microstructural optimization. Nevertheless, they suggested that the data can be considered as a lower bound for the strength and ductility. Fig. 33(a–d) illustrates the strength-ductility combination of FCC based HEAs, BCC based HEAs, dual phase FCC + BCC HEAs, BCC + HCP HEAs, and FCC + HCP HEAs. More data points were added from recent literature available to update the graphs [35,36,59,60,88,298–300]. From these figures, one can arrive at the following conclusions: (i) regardless of the phase and microstructure, HEAs could not outperform high strength steels and other conventional alloys when strength and ductility are compared, (ii) FCC based HEAs occupy a wide spectrum of the plot indicating the ability to tune the composition and microstructure to achieve the design-specific strength and ductility, (iii) BCC based HEAs could achieve extremely high strength, but the ductility is not exceptional, and in some cases not even the minimum acceptable value of 5%, (iv) dual phase and multi-phase HEAs showed a wider distribution in strength-ductility distribution spectrum than BCC based HEAs which indicated the flexibility in compositional space selection to achieve extreme properties, and (v) FCC based HEAs primarily occupied the high

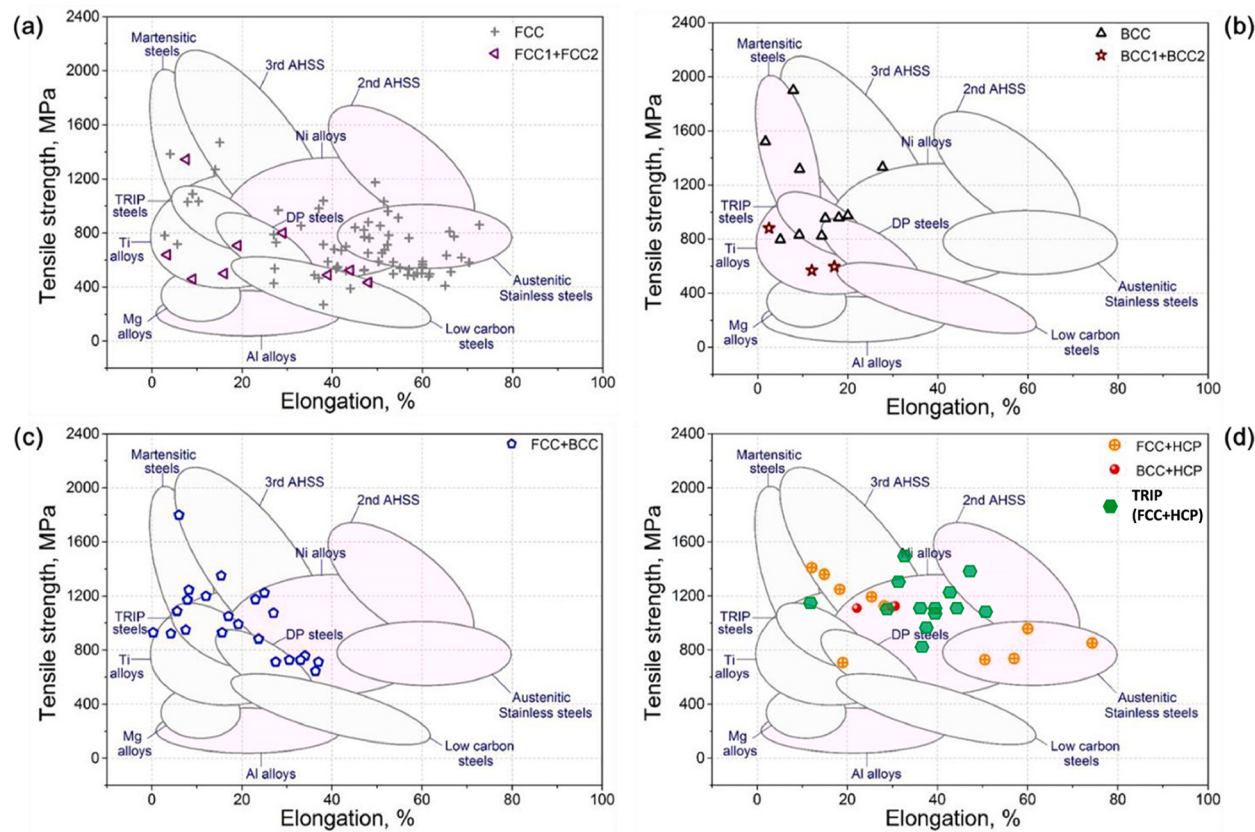


Fig. 33. Performance of HEAs/CCAs at room temperature classified according to the phases present, (a) FCC based HEAs, (b) BCC based HEAs, (c) dual phase FCC + BCC HEAs, and (d) dual phase FCC + HCP and BCC + HCP HEAs [14].

ductility-low strength regime whereas the high strength-low ductility regime is dominated by BCC based HEAs.

Gradual deviation of HEA compositional design from equimolar space to non-equimolar space (called as multi-component alloy or complex concentrated alloy) has enabled to achieve wide range of strength-ductility combination in HEAs/CCAs covering the entire strength-ductility spectrum combinedly occupied by other conventional alloy systems. Apart from good strength and ductility, *cocktail effect* facilitated fatigue, wear, and corrosion resistance enhancement indicates the vast possibility of exploring the composition space to enhance and optimize the mechanical properties [6].

5.1.1. Thermo-mechanical processing to tailor the microstructure – role of “high enthalpy states”

When a metastable HEA is thermo-mechanically processed, various lattice defects are introduced depending on the stacking fault energy of the specific alloy. Let us consider a simple list consisting of point defects, dislocations, stacking faults, twin boundaries, phase boundaries, and grain boundaries. All these lattice imperfections increase the internal energy of the alloy. Mishra and Nene [271] have formalized this in the framework of **high enthalpy states**. Figs. 22, 23 and 32 are good examples of using the thermo-mechanical processing to tailor the microstructure. Fig. 32a shows that the precipitates change based on the prior processing steps. This is different from conventional metallurgy of enhancing the precipitate density using prior cold working or dislocations. For example, in aluminum alloys the pathways of T4 to T6 tempers and T3 to T8 tempers to control the nucleation density of the precipitates is based on introduction of cold work in T3 temper. The cold work after solution treatment introduces dislocations in supersaturated solid solution. This leads to enhanced nucleation density but in general, the precipitating phases don't change! The change in precipitate types in Fig. 32a indicates that the energetics has changed due to previous

thermo-mechanical steps. Or in other words, the enthalpy of the system has altered the phase stability. Similar contrast can be drawn during friction stir processing of metastable TRIP HEAs. Mishra et al. [87] have summarized the impact of concurrent strain, strain rate and temperature on evolution of γ/ϵ microstructure in Fe–Mn–Co–Cr–Si–X HEAs. The relative stability and phase fraction of γ and ϵ change by changing the tool rotation rate during friction stir processing. Again, a comparison with friction stir processing of steels shows the enhanced responsiveness of metastable HEAs. As Mishra and Nene [271] have postulated, the metastable HEAs with stacking fault energy of $<40 \text{ mJ m}^{-2}$ provide exceptional opportunities for microstructural engineering. Some examples of microstructural engineering in HEAs include:

- Heterogeneous grain structure,
- Duplex and triplex microstructures with intermetallic phases,
- Twinning engineered microstructure,
- Coherent boundary engineered microstructure, and
- Dual-phase and triple-phase microstructure with solid solution phases.

This list is by no means exhaustive and many more variants are possible. But it suffices to make the point about importance of **high enthalpy states** in high entropy alloys. This is something that is easily quantifiable by differential scanning calorimetry. As discussed further in Section 6, the microstructural engineering is critical for hierarchical onset of deformation mechanisms to maximize the mechanical properties of HEAs.

5.2. Fracture toughness

In order to qualify HEAs for structural applications requiring high performance and reliability, a knowledge of fracture resistance is

desired. Fracture resistance of alloys is quantified by means of fracture toughness which denotes the material's resistance to crack extension [301]. Although, fracture toughness measurement depends on the type of loading condition, mode 1 fracture toughness (K_{IC}) is generally used for comparison as it represents the lower bound for fracture toughness compared to other primary modes as well as mixed modes [301]. Li et al. [302] extensively reviewed the fracture resistance in HEAs and compared the fracture toughness as a function of alloy composition, phase fraction, and temperature. Material fracture is broadly classified into brittle fracture and ductile fracture; fracture is catastrophic in the former whereas delayed fracture due to crack blunting and plastic deformation ahead of crack tip are the characteristics of the latter. Additionally, need for a well-designed experiment to measure fracture toughness is pointed out by Roy et al. [303]; otherwise the measurements may result in a huge scatter of values. Gludovatz et al. [109,304] studied the fracture toughness of CoCrFeNiMn HEA and CoCrNi MEA and reported exceptional strength-fracture toughness combination of ~ 1 GPa and ~ 200 MPa $m^{1/2}$, respectively, both of which matches the corresponding property level of cryogenic steels. Based on the available fracture toughness data on HEAs [302], K_{IC} value varies from as low as unity to as high as ~ 250 MPa $m^{1/2}$. Such a wide range for fracture toughness in HEA family is attributed to strong influence of alloy composition and phase fraction. Li et al. [302] have also specified the limitation of linear elastic fracture mechanics approach (LEFM) and suggested use of J-integral curve-based approach to determine K_{IC} values for highly ductile HEAs. Fig. 34a shows the Ashby plot for K_{IC} vs yield strength of HEAs in comparison to other conventional alloys. Single phase FCC based MEAs and HEAs possess the maximum fracture toughness whereas BCC based HEAs exhibit much lower fracture toughness due to the brittle nature of the alloys. Dual phase HEAs, such as FCC + BCC and FCC + HCP, have mediocre fracture toughness values. Additionally, a general trend of fracture toughness observed in HEAs is that the K_{IC} value decreases with increase in strength whereas it increases with increase in ductility (Fig. 34b-c).

Qualitative measurement of fracture toughness through impact energy measurement using Charpy impact tests indicated excellent

fracture toughness for $Al_{0.1}CoCrFeNi$ and $Al_{0.3}CoCrFeNi$ HEAs [305] compared to other $AlCoCrFeNi$ HEAs reported by Chen et al. [306]. For investigating the possibility of HEAs in cryogenic applications, it is important to quantify the fracture toughness at cryogenic temperature. However, ductile to brittle transition (DBT) is observed in steels where the ductility and fracture toughness values decline with decrease in temperature [307,308]. However, increase in strength and ductility at cryogenic temperature observed in CoCrNi MEA and CoCrFeNiMn HEA motivated Gullovatz et al. [109,304] to determine their fracture toughness at low temperatures. Interestingly, DBT was not observed and the value of fracture toughness remained constant for CoCrFeNiMn HEA and increased marginally for CoCrNi MEA with decrease in temperature, making them two of the toughest materials reported so far. Impact energy measurement at cryogenic temperature performed in $Al_{0.1}CoCrFeNi$ and $Al_{0.3}CoCrFeNi$ HEAs indicated somewhat deteriorated toughness (less by 30%) compared to room temperature. Although, mechanical characterization has been carried out in a wide range of HEAs designed by exploiting the vast elemental compositional space, the fracture toughness measurement studies are very limited; partly due to complexity of proper fracture toughness testing. While some of the HEAs and MEAs reported excellent strength-toughness properties, further improvement is possible through fine tuning of elemental composition and designing the process route. Equally important is the need to expand the number of HEAs/MEAs with properly tested values of fracture toughness.

5.3. Fatigue

Fatigue is a damage accumulation phenomenon that causes catastrophic failure of the structural materials under cyclic loading. The economic impact of fatigue failure of structural materials subjected to engineering applications is drastic that costs nearly 4% of the United States' gross domestic product [309]. Hence, alloy design strategies to develop fatigue-resistant metals/alloys will be economically beneficial to the society. Although HEAs show combination of exceptional mechanical properties, detailed fatigue analysis is required to qualify the

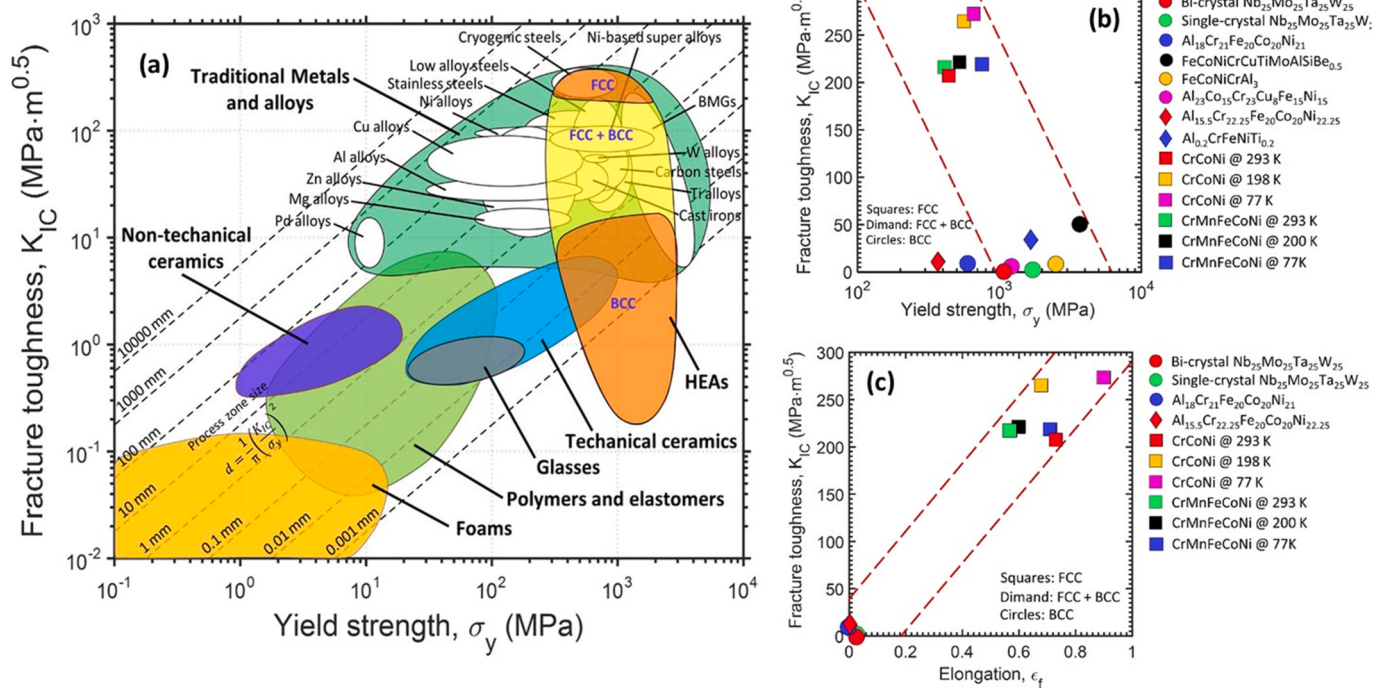


Fig. 34. Ashby plot of fracture toughness vs yield strength of HEAs in comparison to conventional alloy systems, (b) reduction in fracture toughness with increase in strength in HEAs, and (c) improvement in fracture toughness with ductility in HEAs [302].

alloys for structural applications involving cyclic loading. A brief discussion on the fatigue response of HEAs is provided in this section.

Chen et al. [309] provided a detailed review on the high cycle fatigue (HCF) response of HEAs reported in literature and expressed a concern regarding the lack of detailed analysis on the deformation mechanisms in single phase HEAs and refractory HEAs. Recently, Li et al. [236] carried out a short review on low-cycle fatigue (LCF) and HCF response of thirteen compositionally distinct HEAs and provided a guideline for design of fatigue-resistant HEAs. They reported that single phase FCC and BCC HEAs lack excellent fatigue resistance whereas multiphase HEAs exhibited promising fatigue resistance. Primary study conducted by Hemphill et al. [46] on an annealed and rolled Al_{0.5}CoCrCuFeNi HEA having FCC matrix phase with a homogeneous distribution of L1₂ phase indicated wide range of scatter in the fatigue data and the stress range at endurance limit was observed in the range 540–945 MPa, which gave the fatigue ratio (endurance limit/ultimate tensile strength) of 0.20–0.35. Such a wide scatter in fatigue life is attributed to the variation in the distribution of oxygen rich particles in the matrix rather than the change in morphology of the microstructure. In fact, fatigue life is extremely sensitive to manufacturing flaws and therefore, it is a key property to ascertain the pedigree or quality of material. Fatigue loading latches on the weakest microstructural region of specimen and starts failure process from that site.

Further investigation was carried out by Tang et al. [310] in Al_{0.5}CoCrCuFeNi HEA to understand the evolution of deformation mechanism under HCF. TEM images indicated the presence of low density nano-twins and tangled dislocations in the rolled sample. However, TEM analysis performed on samples obtained near crack tip revealed multiple sets of twinning with higher nano-twin density (Fig. 35(a–f)). Higher nano-twin density provides excellent work hardening ahead of the crack tip and improves the resistance to fatigue crack initiation. Thurston et al. [311] studied the temperature dependence on HCF crack propagation behavior of recrystallized CrMnFeCoNi HEA. Threshold applied stress intensity range, ΔK_{TH} increased from 4.8 MPa \sqrt{m} to 6.3 MPa \sqrt{m} with decrease in temperature from ambient condition to 198 K. Additionally, analysis of crack propagation path revealed

transgranular crack propagation in samples tested at room temperature whereas at 198 K the crack propagation was predominantly intergranular. Highly serrated dislocation surface in both the cases suggested planar dislocation slip as the main deformation mechanism.

Shukla et al. [86] performed HCF on AlCoCrFeNi_{2.1} eutectic HEA in as-cast and thermo-mechanically processed conditions. As-cast microstructure consists of FCC and BCC lamellae whereas thermo-mechanically processed material has a hierarchical microstructure with four distinct microstructure features with additional recrystallized FCC and BCC grains apart from the lamellar structure with evidence of B2 precipitate formation inside the FCC grains. Owing to the hierarchical microstructure obtained after thermo-mechanical processing, an improved endurance limit of 500 MPa was obtained when compared to 390 MPa for as-cast alloy. Persistent slip band (PSB) formation in FCC phase was observed as the main reason for crack initiation and presence of hierarchical B2 precipitates in FCC phase in thermo-mechanically processed HEA enhanced its fatigue performance by hindering the path of PSBs (Fig. 36a-d). Above study emphasize the possibility of achieving favorable microstructure in HEAs via thermo-mechanical processing route to improve fatigue resistance.

Liu et al. [312] carried out HCF on an ultrafine-grained (UFG) Al_{0.3}CoCrFeNi HEA obtained via FSP and obtained excellent fatigue endurance limit of ~0.43 UTS. Microstructure of the alloy revealed presence of ordered B2 and σ phases in a UFG FCC matrix. Post failure analysis indicated high density of nano-twins in FCC phase whereas hard B2 and σ phases were void of any persistent deformation mechanism (Fig. 36e-g). They suggested that dislocation pile-up at the B2/FCC interfaces due to stress concentration around the harder B2 phase led to nano-twin formation in the alloy (Fig. 36h-i). Similar nano-twinning was also observed during HCF of CoCrFeMnNi HEA [313]. Liu et al. [314] further investigated the effect of precipitation in Al_{0.7}CoCrFeNi HEA achieved by a low temperature annealing (LTA) after homogenization heat treatment. As-homogenized microstructure consisted of lamellas of FCC and B2 phases whereas further LTA resulted in the formation of nano-sized L1₂ precipitates in FCC phase. Although presence of nano-precipitates enhanced the strength of the alloy, a significant

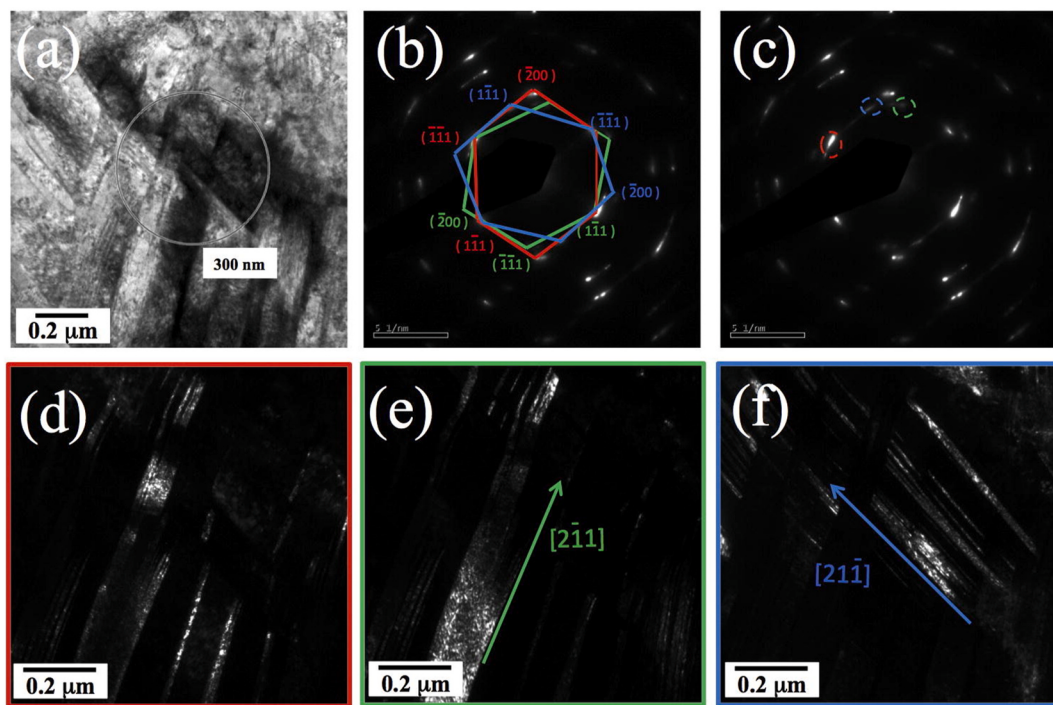


Fig. 35. (a) Presence of two different sets nano-twins along with high density tangled dislocations observed near crack-tip in Al_{0.5}CoCrCuFeNi HEA after HCF, (b) three different sets of diffraction patterns obtained along [011] zone axis, and (d-f) dark field images obtained using the diffraction spots indicated in (c) [310].

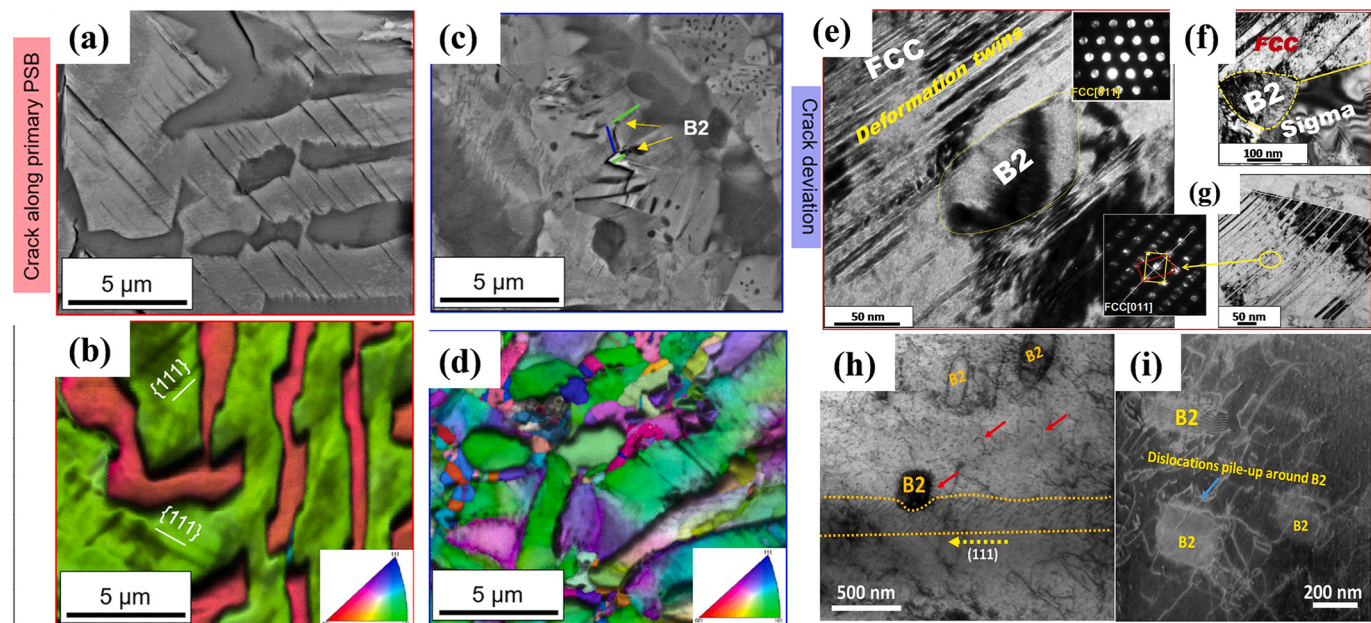


Fig. 36. (a) BSE image and (b) EBSD micrograph indicating crack initiation from PSBs in as-homogenized $\text{AlCoCrFeNi}_{2.1}$ eutectic HEA, (c) BSE image and (d) EBSD IPF map indicating presence of PSBs and crack deviation from harder B2 precipitates [86], (e–g) TEM micrographs showing presence of nano-twinning in FCC phase in $\text{Al}_{0.3}\text{CoCrFeNi}$ HEA (Liu et al.), (h) development of PSBs around harder B2 precipitates in $\text{Al}_{0.7}\text{CoCrFeNi}$ HEA, and (i) dislocation pile up around B2 phase in $\text{Al}_{0.7}\text{CoCrFeNi}$ HEA [312].

improvement in fatigue resistance was not observed; in fact the precipitate rich microstructure indicated a deteriorated fatigue performance (endurance limit $\sim 0.33\text{UTS}$) compared to the homogenized alloy (endurance limit $\sim 0.48\text{UTS}$). TEM analysis revealed the accumulation of dislocation pile-up around the B2 precipitates which acted as crack initiation sites. Early shearing of L1₂ precipitates facilitated ease of motion of dislocations within the FCC matrix which accumulated around the B2 phases and hence resulted in early crack initiation and deteriorated fatigue response. Lack of mechanical twinning could also be a possible reason for performance reduction. Shukla and Mishra [315] studied the effect of fine grained (FG) microstructure on fatigue response of a $\text{CoCr}_{1.3}\text{Ni}$ MEA. The material was cold rolled and subsequent LTA was varied to obtain a FG microstructure (average grain size $\sim 1.4 \mu\text{m}$) and UFG microstructure (average grain size $\sim 0.75 \mu\text{m}$). Although UFG material outperformed FG material at higher stresses, FG material caught up with the UFG material at low stress levels and the fatigue endurance limit is $\sim 0.45\text{UTS}$ in both cases. Detailed TEM analysis near the crack tip revealed the formation of HCP nano-lamella inside the FCC matrix which indicates the activation of stress induced martensitic transformation under HCF.

Further investigation on HCF of metastable HEAs were also carried out [39,110]. As discussed in the previous sections, TRIP provides excellent work hardening ability to the alloy. Effect of TRIP deformation mechanism on the fatigue response of HEAs has been discussed in some studies. Liu et al. [110] studied fatigue response of a FSP metastable dual phase $\text{Fe}_{40}\text{Mn}_{20}\text{Co}_{20}\text{Cr}_{15}\text{Si}_5$ TRIP HEA having a UFG microstructure. Stabilization of γ phase by the synergistic activity of temperature and strain during FSP and the UFG microstructure of the alloy enabled persistent TRIP ahead of crack tip (Fig. 37 (c₁–c₃)) and resulted in excellent fatigue endurance limit of 535 MPa, which is 0.46 UTS. Phase transformation within the plastic zone ahead of the crack tip enhanced the work hardening which in turn delayed crack propagation in the alloy. Crack branching has also been observed near the transformation region which further delayed the primary crack propagation. Liu et al. [39] extended the investigation of fatigue life in an UFG $\text{Fe}_{38.5}\text{Mn}_{20}\text{Co}_{20}\text{Cr}_{15}\text{Si}_5\text{Cu}_{1.5}$ (Cu-HEA) TRIP HEA. This TRIP HEA demonstrated a normalized fatigue strength of ~ 0.62 UTS as noted in Fig. 37(a–b), the

best value reported in the literature so far in HEAs. The alloy exhibited excellent resistance to crack initiation and propagation enabled via $\gamma \rightarrow \epsilon$ martensitic transformation near the crack tip thereby delaying the fatigue failure [39].

The results so far clearly show that incorporation of TWIP and TRIP mechanisms have significant impact on fatigue deformation and fracture. Both the crack initiation life and crack propagation life are impacted. The compositional search needs to focus on tailoring the SFE to incorporate particular micromechanism and the microstructural tailoring can further tune to overall fatigue response. This theme is further developed in the next sections.

5.4. Creep

Sluggish diffusion and lattice distortion are two important core effects in HEAs that have direct bearing on elevated temperature behavior. Although the literature available on high temperature behavior of HEAs is limited, CoCrFeMnNi [316–320], CoCrCuFeNi [321], AlCoCrFeCuNi [322,323], FeCoNiCr , $\text{Al}_x\text{CoCrFeNi}$ [324–327], $\text{AlCoCrFeNi}_{2.1}$, TaNbHfZrTi [328], and $\text{AlTaVNbZr}_{0.25}$ [329] HEAs are some of the alloys systems investigated. Li et al. [330] provided a short review on creep behavior of HEAs and explained the influence of microstructure on creep resistance of different HEAs reported in literature. Similarly, Lin et al. [331] briefed the past research conducted in high temperature creep behavior in HEAs using nanoindentation. Based on the creep data available for conventional polycrystals, Chokshi [332] discussed the dominant deformation mechanisms activated during high temperature deformation within temperature range of $0.5\text{--}0.7 T_m$ (melting point) and grain size, $d < 20 \mu\text{m}$ (Fig. 38). Six different regimes are depicted in the plot with increase in stress; Diffusion creep ($n = 1$), region I of superplasticity ($n > 3$), superplastic flow ($n = 2$), climb-controlled dislocation creep ($n = 5$), and glide-controlled dislocation creep ($n = 3$). Chokshi [332] also suggested that the interface controlled diffusion creep can also be activated at lower stresses and in solute drag controlled dislocation glide at breakaway stress dislocation can break away from solute giving rise to another regime of deformation ($n > 3$), which is between $n = 3$ and power law break down region. Depending upon the

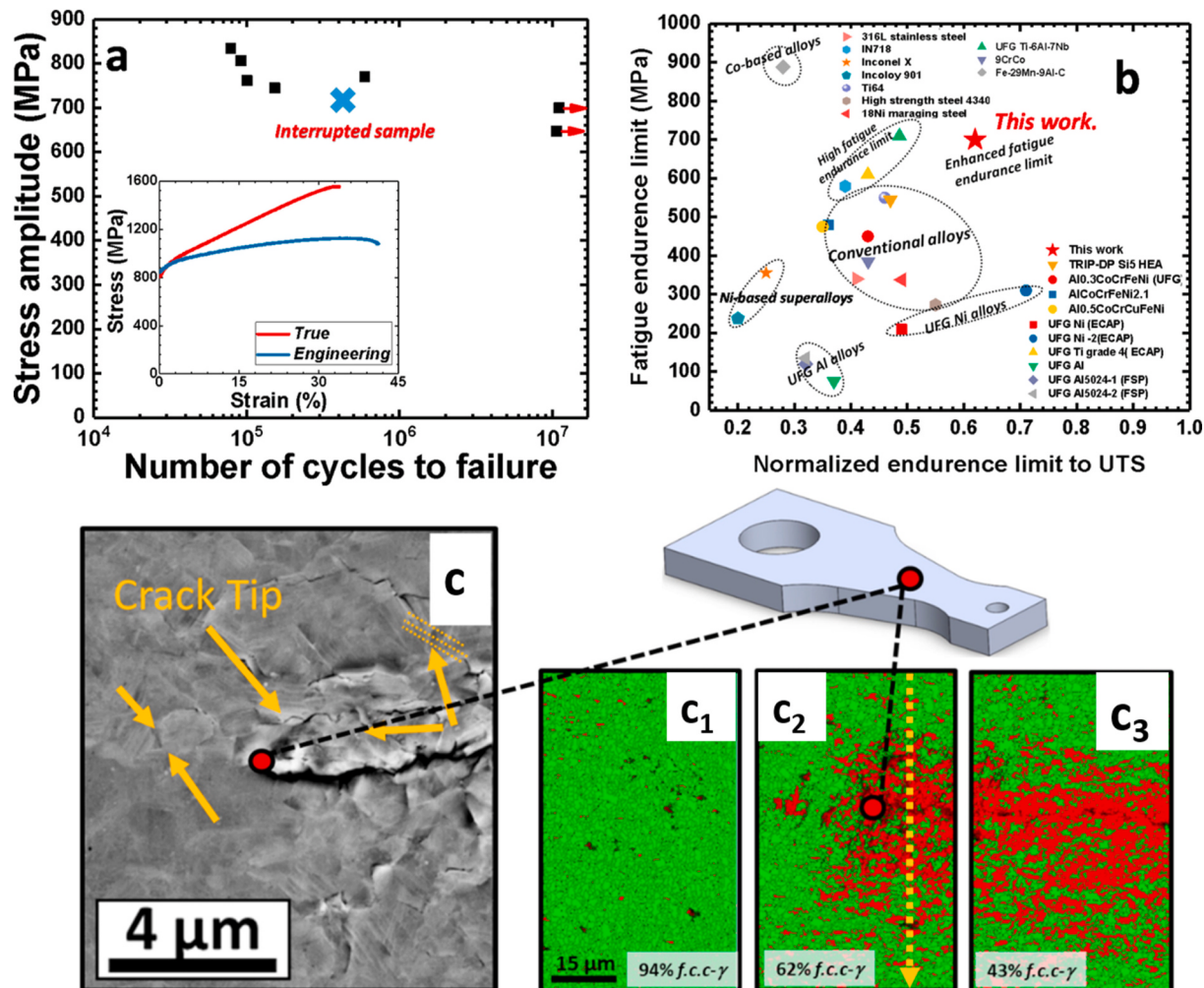


Fig. 37. (a) A S-N curve for ultrafine grained Cu-HEA [39], (b) a plot of fatigue endurance limit vs fatigue ratio comparing the ultrafine grained Cu-HEA with all other fatigue resistant materials [39], and (c,c₁₋₃) EBSD phase map showing microstructural evolution along the crack and at the crack tip for an interrupted fatigue specimen at 114,710 cycles at 717 MPa (0.64 UTS) [39].

microstructure and testing conditions any of the suggested creep deformation mechanism can be activated in HEAs.

Lee et al. [316] conducted nanoindentation creep tests in coarse grained (CG) and nanocrystalline (NC) CoCrFeMnNi HEA and observed difference in the stress exponent of steady state creep strain rate for both microstructures. Higher value of $n \sim 3$ in CG alloy indicated that the creep deformation mechanism is dislocation mediated whereas a lower value of $n \sim 1$ obtained for NC microstructure suggested a diffusion mediated creep (Fig. 39a). Additionally, CoCrFeMnNi HEA has excellent creep resistance when compared to theoretical values of steady state creep strain rate obtained for UFG Ni which reiterates the existence of “sluggish diffusion” in HEAs. He et al. [317] studied the high temperature steady state flow behavior in CoCrFeMnNi alloy between 750°C and 850°C and observed a two distinct stages of strain rate dependence on steady state stress demarcated at a strain rate of $2 \times 10^{-5} \text{ s}^{-1}$ (Fig. 39b). Higher value of stress exponent ($n \sim 5$) observed in high strain rate region suggested dislocation climb mediated deformation mechanism whereas a lower value of $n \sim 3$ at lower strain rate suggested a dislocation glide related creep deformation. Additionally, Lee et al. [318] studied the microstructural activities of precipitation and decomposition on the creep deformation of CoCrFeMnNi HEA at intermediate temperature. The study revealed the formation of intragranular Cr-phase along the dislocations in the entire temperature range considered, intragranular Cr-rich σ phase at 580°C, as well as decomposition and precipitation of other phases along the grain boundary. Recently, Sun

et al. [333] suggested nanostructuring as a possible route to obtain a synergy of high strength and creep resistance in CoCrNi MEA and CoCrFeMnNi HEA.

Cao et al. [324] studied the effect of Al addition on creep resistance in CoCrFeMnNi HEA. Molar ratio x was varied from 0.4 to 0.6 to obtain fcc + bcc duplex-phase $\text{Al}_x\text{CrMnFeCoNi}$ HEAs with equiaxed grain microstructure. The steady state creep rate is lower for $\text{Al}_{0.4}\text{Ce}-\text{FeMnCoNi}$ HEA than CoCeFeMnNi HEA at 600°C. Al provided solid solution and precipitation strengthening to the material and enhanced the creep resistance. However, an interesting observation is that the creep rate curves indicated two distinct stress regions with different exponents in $\text{Al}_{0.4}\text{CoCrFeMnNi}$ HEA, stage 1 with a lower slope $n = 1.6-2.2$ and stage 2 with a higher n value between 4.2 and 4.9 (Fig. 39c). However, such a differentiation is not observed in $\text{Al}_{0.6}\text{CoCrFeMnNi}$ HEA (Fig. 39d). Difference in stress exponent is attributed to variation in rate controlling mechanisms as a function of stress. Dominant creep mechanism at low stress levels in stage I is suggested to be the viscous glide of dislocations as observed in CoCrFeMnNi HEA whereas the higher stress exponent at higher stresses is attributed to be the effect of dislocation climb. Also, the higher creep rate observed in $\text{Al}_{0.6}\text{CoCrFeMnNi}$ HEA than $\text{Al}_{0.4}\text{CoCrFeMnNi}$ HEA is attributed to higher activation volume and SFE due to addition of Al atoms. Further, Cao et al. [325] evaluated creep behavior of $\text{Al}_{0.15}\text{CoCrFeNi}$ HEAs by stress relaxation tests at temperature range of 580°C–700°C. They observed that single phase FCC $\text{Al}_{0.15}\text{CoCrFeNi}$ HEA exhibited higher creep resistance

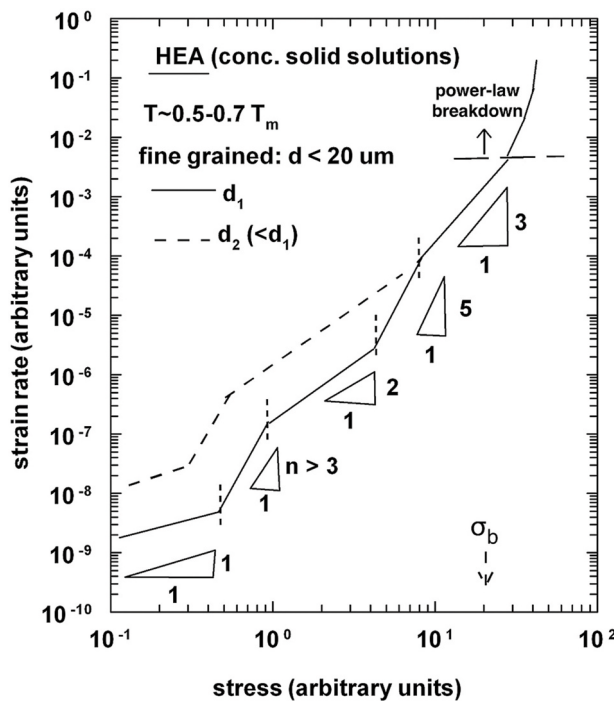


Fig. 38. Strain rate - stress plot polycrystalline materials depicting various possible deformation mechanisms [332].

than dual phase FCC + BCC Al_{0.6}CoCrFeNi HEA. Al_{0.15}CoCrFeNi HEA has a stress exponent of 5.56 and creep activation energy of 385 kJ mol⁻¹ whereas the corresponding values for Al_{0.6}CoCrFeNi HEA are 8.83 and 334 kJ mol⁻¹, respectively. Since activation volume determined for both the alloys fall in cross-slip dominant rate-controlling mechanism, improved creep resistance in Al_{0.15}CoCrFeNi HEA is attributed to its lower SFE. Both studies reveal the possibility of tuning

the alloy composition to improve the creep resistance in HEAs via addition of optimum concentration of minor alloying element such as Al.

Tsao et al. [334] investigated the tensile creep property of a L1₂ strengthened FCC high entropy superalloy ((HESA)) Ni_{47.9}Al_{10.2}Co_{16.9}Cr_{7.4}Fe_{8.9}Ti_{5.8}Mo_{0.9}Nb_{1.2}W_{0.4}C_{0.4} (at. %) at 982, 850 and 750°C at 159 MPa. At 982°C the creep life was 114 h which is comparable 1st generation Ni-based superalloys and the creep curve depicted the absence of a significant primary creep but a gradual increase in strain with a massive tertiary creep. Additionally, activation energy for creep in HESA was 290 kJ mol⁻¹ which is higher than that for Ni-based superalloy CMSX-2 which is 230 kJ mol⁻¹. At 982°C there was no significant evidence of L1₂ particle shearing; however, parallel rafting was observed in L1₂ precipitates along with dislocation pile up in FCC matrix. Lower SFE, higher creep activation energy, stable γ' phases and the sluggish diffusion of the high entropy γ matrix enhanced the creep resistance of the alloy [334].

Kang et al. [319] performed tensile creep tests in CoCrFeMnNi HEA at intermediate temperatures 535–650°C to understand the influence of stress on activated creep mechanisms. Interestingly, at lower stresses the creep curve is characterized by a higher initial creep rate which reduces with time reaching a steady state (stress exponent ~6) whereas at higher stresses an inverted creep curve was observed (stress exponent ~3) which suggests a variation in creep deformation mechanisms. Such a variation in creep curve is attributed to climb-dominated creep at low stresses to viscous glide-dominated creep at higher stresses. Further, with the aid of theoretical analysis they established that Cr atoms having the largest atomic size misfit mostly governs the climb-glide transition during high temperature creep at intermediate strain rates. Of course, the overall number of creep studies are still very few and the key question of magnitude of sluggish diffusion is not clearly quantified. Also, the question of “what the magnitude of creep rate reduction from sluggish diffusion should be” requires significantly more studies with systematic variation of composition and microstructure.

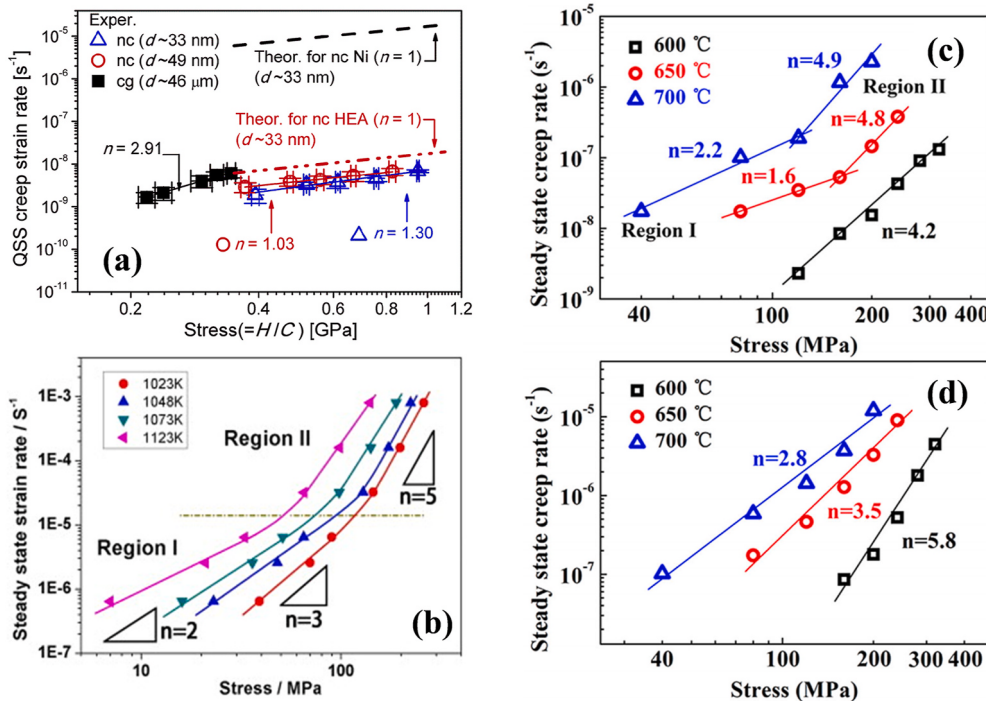


Fig. 39. (a) Variation in steady state creep strain rate as a function of stress for coarse-grained (cg) and nanocrystalline (nc) CoCrFeMnNi HEA [316], (b) two distinct stages of stress dependence on steady state creep strain rate in CoCrFeMnNi HEA [317], (c) steady state creep strain rate indicating two distinct stages of stress dependency in Al_{0.4}CoCrFeMnNi HEA, and (d) corresponding behavior in Al_{0.6}CoCrFeMnNi HEA [324].

6. High entropy alloy design approach: evolving paradigm

The importance of alloy design paradigm shift with the invention of high entropy alloys is well accepted now! The naming of these multi-principal element alloys as high entropy alloys is itself historic and in spite of the discussion on its appropriateness, it has served the alloy physics community well by providing excitement and exceptional potential for discovery. In the context of the current review which is focused on mechanical behavior, the alloy design is intrinsically tied with micromechanisms of deformation. At the most fundamental level, plastic deformation can only take place by moving vacancies or dislocations! The vacancies are important only for diffusion related processes, thereby relevant for creep-limiting designs. For strength-limiting, toughness-limiting and fatigue-limiting, we have to focus on the nature of dislocation-based plasticity. Therefore, in this section we have focused on the dislocation-based mechanisms. Fig. 40 shows a generic depiction of alloy design paradigm and includes the use of macro- and micro-alloying to tune the mechanisms as briefly discussed next.

6.1. Tuning composition for activation of different deformation mechanisms

Although the origin of all deformation mechanisms discussed here is based on dislocations, albeit with full and partial Burgers vector, for practical purposes we make use of the following comprehensive approach:

- Solid solution strengthening – point defects that are particularly relevant for lattice distortion,
- Grain boundary strengthening,
- Dislocation density strengthening,
- Stacking fault strengthening – note that lower SFE leads to dislocations becoming a planar defect rather than a line defect,
- Dual-phase strengthening,
- Deformation induced transformation strengthening – TRIP,
- Deformation induced twinning strengthening – TWIP,
- Precipitation strengthening, and
- Composite strengthening.

Looking at the list, the first obvious thought is, “we already use all these mechanisms in conventional alloys, so what is different?” The answer lies in the concentrated composition of matrix without any dominant host element. Additionally, depending on the specific choice of mechanisms, the matrix composition can vary with the microstructural approach and activation of additional mechanisms. Let us take a few illustrative examples as considering all the nine listed mechanisms is not necessary at this stage. An example of bringing a few mechanisms for hierarchical activation of micromechanisms is illustrated in Fig. 41, where compositional engineering for metastability and microstructural engineering can overcome the traditional strength-ductility tradeoff paradigm.

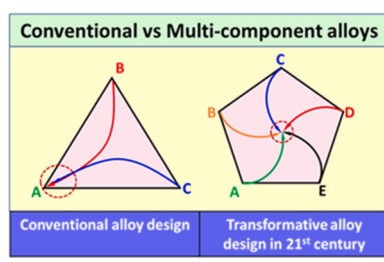


Fig. 40. A generic depiction of paradigm shift from conventional alloy design to transformative alloy design of high entropy alloys. Further evolution has opened the space to multi-phase non-equiautomatic compositions.

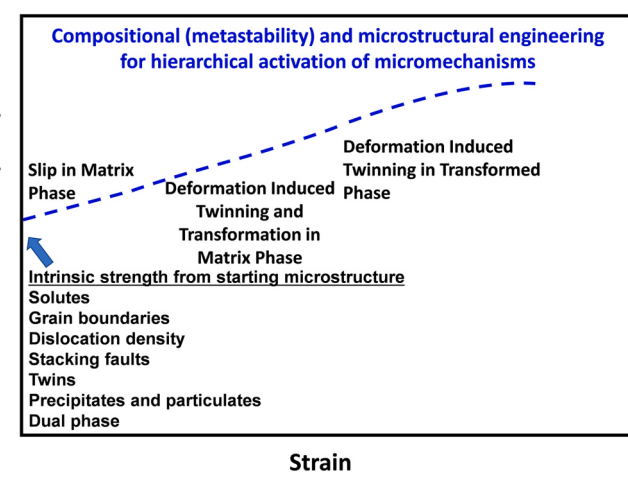


Fig. 41. A hypothetical stress-strain curve for a compositionally engineering HEA that transforms and twins during deformation. Using alloy chemistry and microstructure to sequentially activate micromechanisms is a recipe for overcoming strength-ductility tradeoff observed in conventional alloys.

6.1.1. Stacking fault strengthening in an ultrafine grained or nanocrystalline matrix

Significant research was pursued in the last 30 years on enhancing strength by decreasing grain size to take advantage of emerging severe plastic deformation processing methods. A general trend was that while the strength goes up, work hardening diminishes as dislocation storage decreases when grain size is below a critical range [335–337]. Byun [338] proposed a model for stress-assisted separation of partials. By tuning SFE below 10 mJ m^{-2} , it should be possible to extend the stacking faults across the grain, thereby producing an effective mechanism of work hardening in ultrafine grained and nanocrystalline alloys!

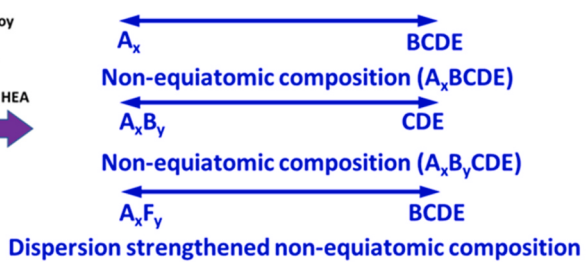
6.1.2. Manipulating twinning and transformation of precipitation strengthened alloy

As reviewed earlier, the HEAs provide a rich playbook for obtaining variations of precipitates in the matrix, thereby concurrently changing the SFE of the matrix phase. This aspect is barely quantified so far and has potential to be very powerful. The example from Gwalani et al. [23, 24, 127] cited before is one example of manipulating the SFE and lattice distortion in an $\text{Al}_x\text{CoCrFeNi}$ system with FCC matrix. There is a need to quantify the change in SFE with precipitation of different phases based on the thermomechanical processing conditions. Such approach has not been examined in BCC and HCP matrices.

6.2. Tuning composition for controlling metastability of phases

As discussed earlier, Mishra and Nene [271] have introduced the concept of **high enthalpy states** of microstructure that synergistically enhances the impact of compositional tailoring of metastability.

Examples of non-equiautomatic composition approaches



Although in generic terms one can argue that most of the materials processing is done in non-equilibrium and far-from-equilibrium states, the context of current metastability is in the narrower domain of **deformation induced transformation**. The deformation induced transformation is relevant for both thermomechanical processing as well as testing of processed alloys. Fig. 42 shows Burgers depiction of shear transitions in the FCC-BCC-HCP system [339] and Cayron has recently discussed the details of angular distortive matrices of these phase transitions [340]. Superimposed on this figure is the observations of $\gamma \rightarrow \varepsilon$ (FCC to HCP) and $\varepsilon \rightarrow \alpha$ (HCP to BCC) in Fe–Mn–Co–Cr–Si–Cu–V metastable HEA system that uses major and minor non-stoichiometric alloying scheme [87,271,341]. Two important aspects of $\gamma \rightarrow \varepsilon$ in Fe–Mn–Co–Cr–Si–X HEAs are volume change and the evolution of c/a ratio [87,271]. There is significant opportunity to cover the various transformation pathways in the FCC-BCC-HCP system and associated changes in volume and lattice parameters. These transitions have potential to impact the mechanical properties in unique ways.

6.2.1. Hierarchical activation of transformation and twinning: can it be effectively coupled with dispersion strengthening and composite strengthening?

The dual phase HEAs provide opportunity to sequence the activation of transformation and subsequent twinning in transformed phase. In the very low stacking fault energy Fe–Mn–Co–Cr–Si HEA, the stacking faults are quite wide. The presence of dispersoids with various sizes provides opportunity to strengthen the matrix further and also bring in the aspect of stress concentration and load transfer. When the dispersoids are in the range of 5–50 nm, they are very effective obstacle for dislocation glide. Interaction of a dissociated dislocation with such fine dispersoids requires much higher stress because of the need for constriction. Currently the TRIP HEAs have not been strengthened with nanodispersoids.

Additionally, when the dispersoids exceed 500 nm size, they are more effective in composite strengthening through load transfer. But they also bring in the aspect of stress concentration at the particle. In TRIP HEAs, one can hypothesize that the stress concentration at such particle will lead to local stress induced transformation. Such a transformation will have particle size dependence, and therefore would have

a gradual progression in the microstructure.

6.2.2. Dilatation during transformation: can it be engineered through elemental selection?

Dilatation is a key part of shear induced transformation. The FCC-HCP-BCC triangle shown in Fig. 42 gives a bird's eye view of each transformation path. The role of dilatation during deformation and crack growth is quite intriguing. The FCC and HCP structures are closed packed whereas the BCC structure is open. So, transformations from FCC or HCP to BCC should lead to volume expansion. Formation of BCC phase internally would then lead to development of compressive stress field around it. On the other hand, formation of FCC or HCP phase in the BCC matrix would develop tensile stress state around the transformed volume. This type of volume change should impact the deformation process in multiple ways. It would set up an internal variation of stress states superimposed with the overall applied stress state. Apart for its influence on the deformation and crack nucleation, the dilatation is likely to directly impact the crack tip plasticity and extension. While initial results show the volume change associated with FCC to HCP transformation in TRIP HEAs, its impact on crack tip mechanisms have not been explored. More importantly, the ability of tailor this dilatation with alloying element selection is unexplored.

7. Future of high entropy alloys or complex concentrated alloys

High entropy alloys or the broader framing of equiatomic compositions and non-equiatomic compositions under the nomenclature of “complex concentrated alloys” is transformative alloying approach! Will it translate in engineering applications? The lead author of this article has been personally involved with rapid solidification in 1980s, metal matrix composites in 1990s, nanocrystalline materials in 1990s and 2000s, bulk metallic glasses in 2000s, friction stir welding and processing in the last twenty years, additive manufacturing in the last five years, and high entropy alloys from 2015. From this involvement, it is relatively easy to reflect back on the promise of each area of research and its progression towards technological impact. Given the complicated layers of materials and technology qualifications/certifications required for structural applications, at a very basic level, there are two drivers for implementation of new materials and new technologies, (a) it will lead to cost savings, and/or (b) the enhanced performance will be enabling! Where do HEAs/CCAs fit in?

Criterion#1: Economic considerations – Let us take this first. For industry to pay attention to all the scientific enthusiasm and discoveries, the cost argument needs to be compartmentalized. If we take the CoCrFeMnNi, the first thought is that it contains Co and Ni, therefore it is costly. However, a quick change in apple-to-apple comparison can shift the consideration. In WC-Co cermets, the binder is relatively pure Co. How about replacing those with cheaper elements in CoCrFeMnNi? Similarly, a cobalt based superalloy, MP159, is material of choice for many applications. Can new HEAs compete with MP159? Under such framing of discussion, the economic considerations are no longer impediments. A clear-cut performance argument and data needed to qualify the new alloy are the barriers.

Criterion#2: Structural performance considerations – Because of the scope of this review, the discussion is limited to structural properties in the Materials Selection in Mechanical Design framework of Ashby.

Stiffness-limiting design: The compositional approach of HEAs provide no intrinsic advantages. The microstructural design of composites is similar to the approaches in the past. So, this sub-group can be considered as not unique to HEAs based on the knowledge so far. Of course, HEA based composites will be a way to take advantage of some intrinsic advantages of micromechanisms of deformation.

Strength-limiting design: This is an area that has been explored significantly, particularly under the strength-ductility paradigm discussion. One line of research that has been pursued by many researchers is the ability to tailor the microstructure of a single alloy to obtain

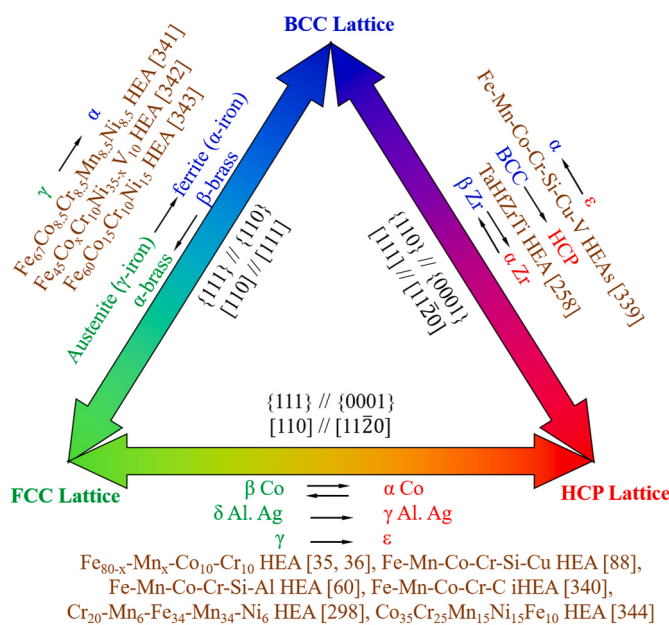


Fig. 42. Shear induced phase transformations in the FCC-HCP-BCC system as represented by Burgers [339]. The current observation of FCC to HCP and HCP to BCC by controlling composition in high entropy alloy system is superimposed [35,38,60,88,261,300,341–346]. All the legs of this FCC-HCP-BCC system have not been explored in the HEAs yet.

different combination of strength-ductility. Primary alloy producers are very keen to sell large volume of a particular composition. One hears such arguments when examples are given regarding how many tons of an aluminum alloy is sold for cans vs aerospace applications. So, the performance and usages have to make the overall case. Tunability of an alloy for a wide range of applications using different processing conditions is a viable argument. Yet, examples of industrial interests have not emerged so far or not publicized. A potential path is to create microstructure-strength-performance that are not possible in conventional alloys. For example, can coherent boundary strengthened HEAs provide unprecedented corrosion resistance in high strength alloys. If one considers stainless steels, higher strength variants are precipitation strengthened. On the other hand, interface strengthened TRIP and TWIP HEAs can easily surpass the highest strength of ~ 1 GPa in conventional stainless steels.

Toughness-limiting design: The nanotwin bridging as a new mechanism and increase of toughness at cryogenic temperatures are two arguments that did resonate with the research community. Extension of that to industry is still lagging. For many such applications, stainless steels are dominant alloys of choice. High strength-toughness combination would be another area of interest and currently the data is limited. Part of the issue is the difficulty in evaluating K_{Ic} . A targeted approach in this area is likely to result in a clear comparison with leading alloys being currently used. Recent results on medium entropy alloys are expanding the toughness argument. But most of the current compositions contain high amount of Co. Therefore, the cost-performance paradigm is important to frame and targeted case studies are needed.

Fatigue-limiting design: Fatigue failures being a dominant issue for industrial structural applications, are good opportunities to pursue. The observation of twinning and transformation during the crack initiation life and crack propagation life have excellent potential to push the fatigue strength. Early results are quite promising and as the understanding grows, this is an area that is very suitable for compositional exploration as well as synergistic microstructural tailoring. Traditionally, steels and titanium alloys are well known for having good fatigue strength and they demonstrate “true” fatigue endurance limit. The best values of fatigue limits of HEAs are better than any conventional alloys! There is a need to expand the fatigue database as the number of studies so far are quite limited. Applications where stainless steels are dominant, HEAs have potential to clearly make a mark.

Creep-limiting design: Creep properties are directly influenced by diffusion and the “sluggish diffusion” core effect led to many discussions about high temperature potential of HEAs. Nickel base superalloys have been the workhorse alloys for high temperature applications. The challenges to effectively produce creep resistant alloys lies in achieving microstructural stability along with retarding diffusional and dislocation processes. Many of the current HEAs have not shown sufficient microstructural stability. Going beyond the nickel base superalloys can be pursued with RHEAs, but apart from not having adequate ductility and processability, they suffer from intrinsic BCC crystal structure related issues.

8. Concluding remarks

Much of this review includes statements regarding the current perspective in specific sections. The field has matured in the last 16+ years and the discussion has certainly moved beyond equiatomic compositions. Obviously, the search for “useful” compositions cuts down the extremely vast alloy discovery space. At the same time, non-equiatomic compositional search make the possibilities virtually infinite within the useful search domain. Even though nascent, the emergence of high-throughput synthesis techniques including friction stir gradient alloying are very promising for explorations of non-equiatomic HEA compositions. The subgroup of HEA research community engaged with structural alloys are quite rightly focused on compositional and microstructural factors controlling the activation of different deformation

mechanisms. With hierarchical activation of micromechanisms in TWIP and TRIP HEAs, quantification of each mechanism during the stress-strain response becomes difficult and advanced diffraction techniques (neutron and synchrotron) have been very helpful. Processability of HEAs with conventional techniques is a big strength for scaling the investigations in future towards qualification/certification for structural applications. Manipulating the onset of deformation induced twinning and transformation allows for excellent strength-ductility combination, observations of unique toughening behavior and pushing the fatigue strength. With further understanding, the quantitative correlation between specific alloying element and the micromechanism would enrich the field. Many coordinated efforts have started across the world and these are likely to lead to examples of industrial transitions. As with any field, crossing the chasm requires efforts that go far beyond university-based research facilities, where the current efforts are centered. Industrial involvement and definition of needs or insertion opportunities are very much demand of the hour! The brief survey of five design approaches and core mechanisms behind the required properties is intended to provide guidance for further development. The tunability of mechanical properties for a given composition is being integrated with advanced manufacturing techniques. In the context of qualification of a new alloy or a new process, opportunity exists for a synergistic “co-implementation” of new alloy and advanced process, e.g. HEA and additive manufacturing!

CRediT authorship contribution statement

Rajiv S. Mishra: Conceptualization, Supervision, Investigation, Data curation, Writing – original draft, Writing – review & editing. **Ravi Sankar Haridas:** Data curation, Investigation, Writing – original draft. **Priyanshi Agrawal:** Data curation, Investigation, Writing – original draft.

Declaration of competing interest

The authors declare that they have no known competing financial interests or personal relationships that could have appeared to influence the work reported in this paper.

Acknowledgements

RSM is grateful to the Army Research Laboratory, USA, for the cooperative agreements (W911NF-18-2-0067 and W911NF1920011) and to the National Science Foundation (grant #1435810) for supporting the research on high entropy alloys.

Data availability statement

The raw/processed data required to reproduce these findings cannot be shared at this time as the data also forms part of an ongoing study and in many cases taken from literature as attributed in the figure captions.

Originality statement

I write on behalf of myself and all co-authors to confirm that the results reported in the manuscript are original and has not been previously published. The authors confirm that the article has not been submitted to peer review, nor has been accepted for publishing in another journal. The authors confirm that the research in their work is original. Because this work is a review, most of the figures are taken from literature with appropriate references cited. If necessary, the article can be recalled, and errors corrected.

References

- [1] J.W. Yeh, S.K. Chen, S.J. Lin, J.Y. Gan, T.S. Chin, T.T. Shun, C.H. Tsau, S. Y. Chang, Nanostructured high-entropy alloys with multiple principal elements: novel alloy design concepts and outcomes, *Adv. Eng. Mater.* 6 (2004) 299–303, <https://doi.org/10.1002/adem.200300567>.
- [2] B. Cantor, I.T.H. Chang, P. Knight, A.J.B. Vincent, Microstructural development in equiaxed multicomponent alloys, *Mater. Sci. Eng. A* 375–377 (2004) 213–218, <https://doi.org/10.1016/j.msea.2003.10.257>.
- [3] W. Hume-Rothery, H.M. Powell, On the theory of super-lattice structures in alloys, *Z. für Kristallogr. Cryst. Mater.* 91 (1935), <https://doi.org/10.1524/zkri.1935.91.1.23>.
- [4] W. Hume-Rothery, B.R. Coles, *I. of Metals, Atomic Theory for Students of Metallurgy*, Institute of Metals, 1988.
- [5] J.W. Yeh, Recent progress in high-entropy alloys, *Ann. Chim. Sci. Des Mater.* 31 (2006) 633–648, <https://doi.org/10.3166/acsm.31.633-648>.
- [6] Y. Zhang, T.T. Zuo, Z. Tang, M.C. Gao, K.A. Dahmen, P.K. Liaw, Z.P. Lu, Microstructures and properties of high-entropy alloys, *Prog. Mater. Sci.* 61 (2014) 1–93, <https://doi.org/10.1016/J.PMATSCI.2013.10.001>.
- [7] M.H. Tsai, J.W. Yeh, High-entropy alloys: a critical review, *Mater. Res. Lett.* 2 (2014) 107–123, <https://doi.org/10.1080/21663831.2014.912690>.
- [8] Y.F. Ye, Q. Wang, J. Lu, C.T. Liu, Y. Yang, High-entropy alloy: challenges and prospects, *Mater. Today* 19 (2016) 349–362, <https://doi.org/10.1016/j.mattod.2015.11.026>.
- [9] D.B. Miracle, O.N. Senkov, A critical review of high entropy alloys and related concepts, *Acta Mater.* 122 (2017) 448–511, <https://doi.org/10.1016/J.ACTAMAT.2016.08.081>.
- [10] Z. Li, S. Zhao, R.O. Ritchie, M.A. Meyers, Mechanical properties of high-entropy alloys with emphasis on face-centered cubic alloys, *Prog. Mater. Sci.* 102 (2019) 296–345, <https://doi.org/10.1016/j.jmatsci.2018.12.003>.
- [11] B.E. MacDonald, Z. Fu, B. Zheng, W. Chen, Y. Lin, F. Chen, L. Zhang, J. Ivanisenko, Y. Zhou, H. Hahn, E.J. Lavernia, Recent progress in high entropy alloy research, *Jom* 69 (2017) 2024–2031, <https://doi.org/10.1007/s11837-017-2484-6>.
- [12] E.P. George, D. Raabe, R.O. Ritchie, High-entropy alloys, *Nat. Rev. Mater.* 4 (2019) 515–534, <https://doi.org/10.1038/s41578-019-0121-4>.
- [13] P. Sathiyamoorthy, H.S. Kim, High-entropy alloys with heterogeneous microstructure: processing and mechanical properties, *Prog. Mater. Sci.* (2020), 100709, <https://doi.org/10.1016/j.jmatsci.2020.100709>.
- [14] E.P. George, W.A. Curtin, C.C. Tasan, High entropy alloys: a focused review of mechanical properties and deformation mechanisms, *Acta Mater.* 188 (2020) 435–474, <https://doi.org/10.1016/j.actamat.2019.12.015>.
- [15] Y.A. Alshataif, S. Sivasankaran, F.A. Al-Mufadi, A.S. Alaboodi, H.R. Ammar, Manufacturing Methods, Microstructural and Mechanical Properties Evolutions of High-Entropy Alloys: A Review, <https://doi.org/10.1007/s12540-019-00565-z>, 2020.
- [16] G.B. Olson, Computational design of hierarchically structured materials, *Science* (80-.) 277 (1997), <https://doi.org/10.1126/science.277.5330.1237>, 1237 LP–1242.
- [17] O.N. Senkov, D.B. Miracle, A new thermodynamic parameter to predict formation of solid solution or intermetallic phases in high entropy alloys, *J. Alloys Compd.* 658 (2016) 603–607, <https://doi.org/10.1016/j.jallcom.2015.10.279>.
- [18] A. Takeuchi, N. Chen, T. Wada, Y. Yokoyama, H. Kato, A. Inoue, J.W. Yeh, Pd20Pt20Cu20Ni20P20 high-entropy alloy as a bulk metallic glass in the centimeter, *Intermetallics* 19 (2011) 1546–1554, <https://doi.org/10.1016/j.intermet.2011.05.030>.
- [19] J.Y. He, H. Wang, H.L. Huang, X.D. Xu, M.W. Chen, Y. Wu, X.J. Liu, T.G. Nieh, K. An, Z.P. Lu, A precipitation-hardenable high-entropy alloy with outstanding tensile properties, *Acta Mater.* 102 (2016) 187–196, <https://doi.org/10.1016/j.actamat.2015.08.076>.
- [20] S. Yadav, A. Kumar, K. Biswas, Wear behavior of high entropy alloys containing soft dispersoids (Pb, Bi), *Mater. Chem. Phys.* 210 (2018) 222–232, <https://doi.org/10.1016/j.matchemphys.2017.06.020>.
- [21] S. Yadav, S. Sarkar, A. Aggarwal, A. Kumar, K. Biswas, Wear and mechanical properties of novel (CuCrFeTiZn)100-xPbx high entropy alloy composite via mechanical alloying and spark plasma sintering, *Wear* 410–411 (2018) 93–109, <https://doi.org/10.1016/j.wear.2018.05.023>.
- [22] S. Dasari, A. Jagetia, V. Soni, B. Gwalani, S. Gorsse, R. Banerjee, Engineering transformation pathways in an Al0.3CoFeNi complex concentrated alloy leads to excellent strength–ductility combination, *Mater. Res. Lett.* 8 (2020) 399–407, <https://doi.org/10.1080/21663831.2020.1777215>.
- [23] B. Gwalani, S. Gorsse, D. Choudhuri, M. Styles, Y. Zheng, R.S. Mishra, R. Banerjee, Modifying transformation pathways in high entropy alloys or complex concentrated alloys via thermo-mechanical processing, *Acta Mater.* 153 (2018) 169–185, <https://doi.org/10.1016/j.actamat.2018.05.009>.
- [24] B. Gwalani, S. Gorsse, D. Choudhuri, Y. Zheng, R.S. Mishra, R. Banerjee, Tensile yield strength of a single bulk Al 0.3 CoCrFeNi high entropy alloy can be tuned from 160 MPa to 1800 MPa, *Scr. Mater.* 162 (2019) 18–23, <https://doi.org/10.1016/j.scriptamat.2018.10.023>.
- [25] S. Gangireddy, B. Gwalani, V. Soni, R. Banerjee, R.S. Mishra, Contrasting mechanical behavior in precipitation hardenable Al_xCoCrFeNi high entropy alloy microstructures: single phase FCC vs. dual phase FCC-BCC, *Mater. Sci. Eng. A* 739 (2019) 158–166, <https://doi.org/10.1016/j.msea.2018.10.021>.
- [26] S. Singh, N. Wanderka, B.S. Murty, U. Glatzel, J. Banhart, Decomposition in multi-component AlCoCrCuFeNi high-entropy alloy, *Acta Mater.* 59 (2011) 182–190, <https://doi.org/10.1016/j.actamat.2010.09.023>.
- [27] S. Shukla, T. Wang, M. Frank, P. Agrawal, S. Sinha, R.A. Mirshams, R.S. Mishra, Friction stir gradient alloying: a novel solid-state high throughput screening technique for high entropy alloys, *Mater. Today Commun.* 23 (2020), 100869, <https://doi.org/10.1016/j.jmtcomm.2019.100869>.
- [28] P. Agrawal, S. Shukla, S. Gupta, P. Agrawal, R.S. Mishra, Friction stir gradient alloying: a high-throughput method to explore the influence of V in enabling HCP to BCC transformation in a γ-FCC dominated high entropy alloy, *Appl. Mater. Today* 21 (2020), 100853, <https://doi.org/10.1016/j.apmt.2020.100853>.
- [29] K. Tseng, Y. Yang, C. Juan, T. Chin, C. Tsai, J. Yeh, A light-weight high-entropy alloy Al20Be20Fe10Si15Ti35, *Sci. China Technol. Sci.* 61 (2018) 184–188, <https://doi.org/10.1007/s11431-017-9073-0>.
- [30] R. Feng, M.C. Gao, C. Zhang, W. Guo, J.D. Poplawsky, F. Zhang, J.A. Hawk, J. C. Neufeind, Y. Ren, P.K. Liaw, Phase stability and transformation in a light-weight high-entropy alloy, *Acta Mater.* 146 (2018) 280–293, <https://doi.org/10.1016/j.actamat.2017.12.061>.
- [31] N.D. Stepanov, D.G. Shaysultanov, G.A. Salishchev, M.A. Tikhonovsky, Structure and mechanical properties of a light-weight AlNbTiV high entropy alloy, *Mater. Lett.* 142 (2015) 153–155, <https://doi.org/10.1016/j.matlet.2014.11.162>.
- [32] K.M. Youssef, A.J. Zaddach, C. Niu, D.L. Irving, C.C. Koch, A novel low-density, high-hardness, high-entropy alloy with close-packed single-phase nanocrystalline structures, *Mater. Res. Lett.* 3 (2015) 95–99, <https://doi.org/10.1080/21663831.2014.985855>.
- [33] R. Li, J.C. Gao, K. Fan, Study to microstructure and mechanical properties of Mg containing high entropy alloys, *Mater. Sci. Forum* 650 (2010) 265–271. <https://doi.org/10.4028/www.scientific.net/MSF.650.265>.
- [34] O. Maulik, D. Kumar, S. Kumar, D.M. Fabijanic, V. Kumar, Structural evolution of spark plasma sintered AlFeCuCrMgx (x = 0, 0.5, 1, 1.7) high entropy alloys, *Intermetallics* 77 (2016) 46–56, <https://doi.org/10.1016/j.intermet.2016.07.001>.
- [35] Z. Li, K.G. Pradeep, Y. Deng, D. Raabe, C.C. Tasan, Metastable high-entropy dual-phase alloys overcome the strength–ductility trade-off, *Nature* 534 (2016) 227–230, <https://doi.org/10.1038/nature17981>.
- [36] S.S. Nene, K. Liu, M. Frank, R.S. Mishra, R.E. Brennan, K.C. Cho, Z. Li, D. Raabe, Enhanced strength and ductility in a friction stir processing engineered dual phase high entropy alloy, *Sci. Rep.* 7 (2017) 16167, <https://doi.org/10.1038/s41598-017-16509-9>.
- [37] P. Agrawal, S. Thapliyal, S.S. Nene, R.S. Mishra, B.A. McWilliams, K.C. Cho, Excellent strength–ductility synergy in metastable high entropy alloy by laser powder bed additive manufacturing, *Addit. Manuf.* 32 (2020), 101098, <https://doi.org/10.1016/j.addma.2020.101098>.
- [38] S.S. Nene, M. Frank, K. Liu, S. Sinha, R.S. Mishra, B. McWilliams, K.C. Cho, Reversed strength–ductility relationship in microstructurally flexible high entropy alloy, *Scr. Mater.* 154 (2018) 163–167, <https://doi.org/10.1016/J.SCRIPTAMAT.2018.05.043>.
- [39] K. Liu, S.S. Nene, M. Frank, S. Sinha, R.S. Mishra, Extremely high fatigue resistance in an ultrafine grained high entropy alloy, *Appl. Mater. Today* 15 (2019) 525–530, <https://doi.org/10.1016/J.APMT.2019.04.001>.
- [40] S. Thapliyal, S.S. Nene, P. Agrawal, T. Wang, C. Morphew, R.S. Mishra, B. A. McWilliams, K.C. Cho, Damage-tolerant, corrosion-resistant high entropy alloy with high strength and ductility by laser powder bed fusion additive manufacturing, *Addit. Manuf.* 36 (2020), 101455, <https://doi.org/10.1016/j.addma.2020.101455>.
- [41] S.G. Ma, S.F. Zhang, J.W. Qiao, Z.H. Wang, M.C. Gao, Z.M. Jiao, H.J. Yang, Y. Zhang, Superior high tensile elongation of a single-crystal CoCrFeNiAl 0.3 high-entropy alloy by Bridgman solidification, *Intermetallics* 54 (2014) 104–109, <https://doi.org/10.1016/j.intermet.2014.05.018>.
- [42] T.T. Shun, Y.C. Du, Microstructure and tensile behaviors of FCC Al10.3CoCrFeNi high entropy alloy, *J. Alloys Compd.* 479 (2009) 157–160, <https://doi.org/10.1016/j.jallcom.2008.12.088>.
- [43] H.M. Daoud, A. Manzoni, R. Völkli, N. Wanderka, U. Glatzel, Microstructure and tensile behavior of Al8Co17Cr17Cu8Fe17Ni33 (at.%) high-entropy alloy, *Jom* 65 (2013) 1805–1814, <https://doi.org/10.1007/s11837-013-0756-3>.
- [44] B. Gwalani, D. Choudhuri, V. Soni, Y. Ren, M. Styles, J.Y. Hwang, S.J. Nam, H. Ryu, S.H. Hong, R. Banerjee, Cu assisted stabilization and nucleation of L12 precipitates in Al0.3CuFeCrNi2 fcc-based high entropy alloy, *Acta Mater.* 129 (2017) 170–182, <https://doi.org/10.1016/j.actamat.2017.02.053>.
- [45] F. Wang, Y. Zhang, G. Chen, H.A. Davies, Tensile and compressive mechanical behavior of a CoCrCuFeNiAl0.5 high entropy alloy, *Int. J. Mod. Phys. B* 23 (2009) 1254–1259, <https://doi.org/10.1142/S02179797209060774>.
- [46] M.A. Hemphill, T. Yuan, G.Y. Wang, J.W. Yeh, C.W. Tsai, A. Chuang, P.K. Liaw, Fatigue behavior of Al 0.5CoCrFeNi high entropy alloys, *Acta Mater.* 60 (2012) 5723–5734, <https://doi.org/10.1016/j.actamat.2012.06.046>.
- [47] C.W. Tsai, M.H. Tsai, J.W. Yeh, C.C. Yang, Effect of temperature on mechanical properties of Al10.5CoCrCuFeNi wrought alloy, *J. Alloys Compd.* 490 (2010) 160–165, <https://doi.org/10.1016/j.jallcom.2009.10.088>.
- [48] C. Ng, S. Guo, J. Luan, Q. Wang, J. Lu, S. Shi, C.T. Liu, Phase stability and tensile properties of Co-free Al 0.5CrCuFeNi2 high-entropy alloys, *J. Alloys Compd.* 584 (2014) 530–537, <https://doi.org/10.1016/j.jallcom.2013.09.105>.
- [49] A.V. Kuznetsov, D.G. Shaysultanov, N.D. Stepanov, G.A. Salishchev, O.N. Senkov, Tensile properties of an AlCrCuNiFeCo high-entropy alloy in as-cast and wrought conditions, *Mater. Sci. Eng. A* 533 (2012) 107–118, <https://doi.org/10.1016/j.msea.2011.11.045>.
- [50] F. Otto, A. Dlouhý, C. Somsen, H. Bei, G. Eggeler, E.P. George, The influences of temperature and microstructure on the tensile properties of a CoCrFeMnNi high-entropy alloy, *Acta Mater.* 61 (2013) 5743–5755, <https://doi.org/10.1016/j.actamat.2013.06.018>.

- [51] A.J. Zaddach, C. Niu, C.C. Koch, D.L. Irving, Mechanical properties and stacking fault energies of NiFeCrCoMn high-entropy alloy, *Jom* 65 (2013) 1780–1789, <https://doi.org/10.1007/s11837-013-0771-4>.
- [52] A. Gali, E.P. George, Tensile properties of high- and medium-entropy alloys, *Intermetallics* 39 (2013) 74–78, <https://doi.org/10.1016/j.intermet.2013.03.018>.
- [53] O.N. Senkov, S.V. Senkova, C. Woodward, Effect of aluminum on the microstructure and properties of two refractory high-entropy alloys, *Acta Mater.* 68 (2014) 214–228, <https://doi.org/10.1016/j.actamat.2014.01.029>.
- [54] O.N. Senkov, S.V. Senkova, C. Woodward, D.B. Miracle, Low-density, refractory multi-principal element alloys of the Cr-Nb-Ti-V-Zr system: microstructure and phase analysis, *Acta Mater.* 61 (2013) 1545–1557, <https://doi.org/10.1016/j.actamat.2012.11.032>.
- [55] X. Yang, Y. Zhang, P.K. Liaw, Microstructure and compressive properties of NbTiVTAIx high entropy alloys, *Procedia Eng.* 36 (2012) 292–298, <https://doi.org/10.1016/j.proeng.2012.03.043>.
- [56] O.N. Senkov, G.B. Wilks, J.M. Scott, D.B. Miracle, Mechanical properties of Nb₂₅Mo₂₅Ta₂₅W₂₅ and V₂₀Nb₂₀Mo₂₀Ta₂₀W₂₀ refractory high entropy alloys, *Intermetallics* 19 (2011) 698–706, <https://doi.org/10.1016/j.intermet.2011.01.004>.
- [57] E. Fazakas, V. Zadorozhny, L.K. Varga, A. Inoue, D.V. Louzguine-Luzgin, F. Tian, L. Vitos, Experimental and theoretical study of Ti₂₀Zr₂₀Hf₂₀Nb₂₀X₂₀ (X = v or Cr) refractory high-entropy alloys, *Int. J. Refract. Met. Hard Mater.* 47 (2014) 131–138, <https://doi.org/10.1016/j.ijrmhm.2014.07.009>.
- [58] O.N. Senkov, C. Woodward, D.B. Miracle, Microstructure and properties of aluminum-containing refractory high-entropy alloys, *Jom* 66 (2014) 2030–2042, <https://doi.org/10.1007/s11837-014-1066-0>.
- [59] S.S. Nene, M. Frank, K. Liu, R.S. Mishra, B.A. McWilliams, K.C. Cho, Extremely high strength and work hardening ability in a metastable high entropy alloy, *Sci. Rep.* 8 (2018) 9920, <https://doi.org/10.1038/s41598-018-28383-0>.
- [60] S.S. Nene, S. Sinha, M. Frank, K. Liu, R.S. Mishra, B.A. McWilliams, K.C. Cho, Unexpected strength–ductility response in an annealed, metastable, high-entropy alloy, *Appl. Mater. Today.* 13 (2018) 198–206, <https://doi.org/10.1016/J.APMT.2018.09.002>.
- [61] R.A. Swalin, *Thermodynamics of Solids*, J. Wiley, 1972.
- [62] D.R. Gaskell, D.E. Laughlin, Introduction to the Thermodynamics of Materials, sixth ed., CRC Press, 2017 <https://doi.org/10.1201/9781315119038>.
- [63] B.S. Murty, J.W. Yeh, S. Ranganathan, P.P. Bhattacharjee, High Entropy Alloys, Elsevier, 2019, <https://doi.org/10.1016/B978-0-12-816067-1.00001-1>.
- [64] F. Otto, Y. Yang, H. Bei, E.P. George, Relative effects of enthalpy and entropy on the phase stability of equiatomic high-entropy alloys, *Acta Mater.* 61 (2013) 2628–2638, <https://doi.org/10.1016/j.actamat.2013.01.042>.
- [65] F. Otto, A. Dlouhý, K.G. Pradeep, M. Kuběnová, D. Raabe, G. Eggeler, E.P. George, Decomposition of the single-phase high-entropy alloy CrMnFeCoNi after prolonged anneals at intermediate temperatures, *Acta Mater.* 112 (2016) 40–52, <https://doi.org/10.1016/j.actamat.2016.04.005>.
- [66] J.W. Yeh, S.Y. Chang, Y. De Hong, S.K. Chen, S.J. Lin, Anomalous decrease in X-ray diffraction intensities of Cu-Ni-Al-Co-Cr-Fe-Si alloy systems with multi-principal elements, *Mater. Chem. Phys.* 103 (2007) 41–46, <https://doi.org/10.1016/j.matchemphys.2007.01.003>.
- [67] Y. Zhang, X. Yang, P.K. Liaw, Alloy design and properties optimization of high-entropy alloys, *JOM* 64 (2012) 830–838, <https://doi.org/10.1007/s11837-012-0366-5>.
- [68] Y.J. Zhou, Y. Zhang, Y.L. Wang, G.L. Chen, Solid solution alloys of AlCoCrFeNiTiX with excellent room-temperature mechanical properties, *Appl. Phys. Lett.* 90 (2007), 181904, <https://doi.org/10.1063/1.2734517>.
- [69] Y. Zhang, Y. Zhou, X. Hui, M. Wang, G. Chen, Minor alloying behavior in bulk metallic glasses and high-entropy alloys, *Sci. China Ser. G Phys. Mech. Astron.* 51 (2008) 427–437, <https://doi.org/10.1007/s11433-008-0050-5>.
- [70] J. Yeh, S. Chen, J. Gan, S. Lin, T. Chin, Formation of simple crystal structures in Cu-Co-Ni-Cr-Al-Fe-Ti-V alloys with multiprincipal metallic elements, *Mater. Mater. A.* 35 (2010) 2533–2536.
- [71] H.K.D.H. Bhadeshia, High entropy alloys, *Mater. Sci. Technol.* 31 (2015) 1139–1141, <https://doi.org/10.1179/0267083615Z.00000000969>.
- [72] K.K. Sankaran, R.S. Mishra, Metallurgy and Design of Alloys with Hierarchical Microstructures, Elsevier, 2017, <https://doi.org/10.1016/B978-0-12-812068-2.01001-8>.
- [73] M. Komarasamy, N. Kumar, R.S. Mishra, P.K. Liaw, Anomalies in the deformation mechanism and kinetics of coarse-grained high entropy alloy, *Mater. Sci. Eng. A.* 654 (2016) 256–263, <https://doi.org/10.1016/j.msea.2015.12.063>.
- [74] R.S. Mishra, N. Kumar, M. Komarasamy, Lattice strain framework for plastic deformation in complex concentrated alloys including high entropy alloys, *Mater. Sci. Technol.* 31 (2015) 1259–1263, <https://doi.org/10.1179/1743284715Y.0000000050>.
- [75] Y. Hao, X.X. Wu, X.Y. San, S. Li, X.K. Zhu, The influence of stacking fault energy on compression test of Cu and Cu-Al alloys, *Procedia Eng.* 36 (2012) 307–315, <https://doi.org/10.1016/j.proeng.2012.03.045>.
- [76] M. Komarasamy, S. Shukla, N. Ley, K. Liu, K. Cho, B. McWilliams, R. Brennan, M. L. Young, R.S. Mishra, A novel method to enhance CSL fraction, tensile properties and work hardening in complex concentrated alloys – Lattice distortion effect, *Mater. Sci. Eng. A.* 736 (2018) 383–391, <https://doi.org/10.1016/j.msea.2018.09.005>.
- [77] E.I. Galindo-Navia, P.E.J. Rivera-Díaz-del-Castillo, Understanding martensite and twin formation in austenitic steels: a model describing TRIP and TWIP effects, *Acta Mater.* 128 (2017) 120–134, <https://doi.org/10.1016/j.actamat.2017.02.004>.
- [78] Z. Balogh, G. Schmitz, Diffusion in metals and alloys, in: *Phys. Metall.*, Elsevier, 2014, pp. 387–559, <https://doi.org/10.1016/B978-0-444-53770-6.00005-8>.
- [79] G. Hevesy, A. Obreutsheva, Self-diffusion in solid metals, *Nature* 115 (1925) 674–675, <https://doi.org/10.1038/115674a0>.
- [80] B.S. Bokstein, B.B. Straumal, Diffusion in materials science and technology, in: *Diffus. Spreading Nature, Technol. Soc.*, Springer International Publishing, Cham, 2018, pp. 261–275, https://doi.org/10.1007/978-3-319-67798-9_13.
- [81] K.Y. Tsai, M.H. Tsai, J.W. Yeh, Sluggish diffusion in Co-Cr-Fe-Mn-Ni high-entropy alloys, *Acta Mater.* 61 (2013) 4887–4897, <https://doi.org/10.1016/j.actamat.2013.04.058>.
- [82] S. Ranganathan, Alloyed pleasures: multmetallic cocktails, *Curr. Sci.* 85 (2003) 1404–1406.
- [83] J.-W. Yeh, Physical metallurgy of high-entropy alloys, *JOM* 67 (2015) 2254–2261, <https://doi.org/10.1007/s11837-015-1583-5>.
- [84] Z.P. Lu, H. Wang, M.W. Chen, I. Baker, J.W. Yeh, C.T. Liu, T.G. Nieh, An assessment on the future development of high-entropy alloys: summary from a recent workshop, *Intermetallics* 66 (2015) 67–76, <https://doi.org/10.1016/j.intermet.2015.06.021>.
- [85] Y.-F. Kao, T.-J. Chen, S.-K. Chen, J.-W. Yeh, Microstructure and mechanical property of as-cast, -homogenized, and -deformed AlxCoCrFeNi (0<x≤2) high-entropy alloys, *J. Alloys Compd.* 488 (2009) 57–64, <https://doi.org/10.1016/j.jallcom.2009.08.090>.
- [86] S. Shukla, T. Wang, S. Cotton, R.S. Mishra, Hierarchical microstructure for improved fatigue properties in a eutectic high entropy alloy, *Scr. Mater.* 156 (2018) 105–109, <https://doi.org/10.1016/j.scriptamat.2018.07.022>.
- [87] R.S. Mishra, S.S. Nene, M. Frank, S. Sinha, K. Liu, S. Shukla, Metastability driven hierarchical microstructural engineering: overview of mechanical properties of metastable complex concentrated alloys, *J. Alloys Compd.* 842 (2020), 155625, <https://doi.org/10.1016/j.jallcom.2020.155625>.
- [88] S.S. Nene, M. Frank, K. Liu, S. Sinha, R.S. Mishra, B.A. McWilliams, K.C. Cho, Corrosion-resistant high entropy alloy with high strength and ductility, *Scr. Mater.* 166 (2019) 168–172, <https://doi.org/10.1016/J.SCR.2019.03.028>.
- [89] C.J. Tong, M.-R. Chen, J.-W. Yeh, S.-J. Lin, S.-K. Chen, T.-T. Shun, S.-Y. Chang, Mechanical performance of the Al x CoCrCuFeNi high-entropy alloy system with multiprincipal elements, *Metall. Mater. Trans. A.* 36 (2005) 1263–1271, <https://doi.org/10.1007/s11661-005-0218-9>.
- [90] C.J. Tong, Y.-L. Chen, J.-W. Yeh, S.-J. Lin, S.-K. Chen, T.-T. Shun, C.-H. Tsau, S.-Y. Chang, Microstructure characterization of Al x CoCrCuFeNi high-entropy alloy system with multiprincipal elements, *Metall. Mater. Trans. A.* 36 (2005) 881–893, <https://doi.org/10.1007/s11661-005-0283-0>.
- [91] D. Misseroni, A.B. Movchan, N.V. Movchan, D. Bigoni, Experimental and analytical insights on fracture trajectories in brittle materials with voids, *Int. J. Solids Struct.* 63 (2015) 219–225, <https://doi.org/10.1016/j.ijсолstr.2015.03.001>.
- [92] Y. Ma, B. Jiang, C. Li, Q. Wang, C. Dong, P. Liaw, F. Xu, L. Sun, The BCC/B2 morphologies in AlxNiCoFeCr high-entropy alloys, *Metals (Basel)* 7 (2017) 57, <https://doi.org/10.3390/met7020057>.
- [93] L.J. Santodonato, Y. Zhang, M. Feygenson, C.M. Parish, M.C. Gao, R.J.K. Weber, J.C. Neufeind, Z. Tang, P.K. Liaw, Deviation from high-entropy configurations in the atomic distributions of a multi-principal-element alloy, *Nat. Commun.* 6 (2015) 5964, <https://doi.org/10.1038/ncomms6964>.
- [94] B.A. Welk, R.E.A. Williams, G.B. Viswanathan, M.A. Gibson, P.K. Liaw, H. L. Fraser, Nature of the interfaces between the constituent phases in the high entropy alloy CoCrCuFeNiAl, *Ultramicroscopy* 134 (2013) 193–199, <https://doi.org/10.1016/j.ultramic.2013.06.006>.
- [95] A. Manzoni, H. Daoud, R. Völkli, U. Glatzel, N. Wunderka, Phase separation in equiatomic AlCoCrFeNi high-entropy alloy, *Ultramicroscopy* 132 (2013) 212–215, <https://doi.org/10.1016/j.ultramic.2012.12.015>.
- [96] J. Ding, Q. Yu, M. Asta, R.O. Ritchie, Tunable stacking fault energies by tailoring local chemical order in CrCoNi medium-entropy alloys, *Proc. Natl. Acad. Sci.* 115 (2018) 8919–8924, <https://doi.org/10.1073/pnas.1808660115>.
- [97] G. Laplanche, A. Kostka, C. Reinhart, J. Hunfeld, G. Eggeler, E.P. George, Reasons for the superior mechanical properties of medium-entropy CrCoNi compared to high-entropy CrMnFeCoNi, *Acta Mater.* 128 (2017) 292–303, <https://doi.org/10.1016/j.actamat.2017.02.036>.
- [98] J. Miao, C.E. Sloane, T.M. Smith, C. Niu, H. Bei, M. Ghazisaeidi, G.M. Pharr, M. J. Mills, The evolution of the deformation substructure in a Ni-Co-Cr equiatomic solid solution alloy, *Acta Mater.* 132 (2017) 35–48, <https://doi.org/10.1016/j.actamat.2017.04.033>.
- [99] F.X. Zhang, S. Zhao, K. Jin, H. Xue, G. Velisa, H. Bei, R. Huang, J.Y.P. Ko, D. C. Pagan, J.C. Neufeind, W.J. Weber, Y. Zhang, Local structure and short-range order in a NiCoCr solid solution alloy, *Phys. Rev. Lett.* 118 (2017) 1–6, <https://doi.org/10.1103/PhysRevLett.118.205501>.
- [100] R. Zhang, S. Zhao, J. Ding, Y. Chong, T. Jia, C. Ophus, M. Asta, R.O. Ritchie, A. M. Minor, Short-range order and its impact on the CrCoNi medium-entropy alloy, *Nature* 581 (2020) 283–287, <https://doi.org/10.1038/s41586-020-2275-z>.
- [101] D. Sobieraj, J.S. Wróbel, T. Rygier, K.J. Kurzydowski, O. El Atwani, A. Devaraj, E. Martinez Saez, D. Nguyen-Manh, Chemical short-range order in derivative Cr-Ta-Ti-V-W high entropy alloys from the first-principles thermodynamic study, *Phys. Chem. Chem. Phys.* 22 (2020) 23929–23951, <https://doi.org/10.1039/d0cp03764h>.
- [102] M.M. Nygård, W.A. Śląwiński, G. Ek, M.H. Sorby, M. Sahlberg, D.A. Keen, B. C. Hauback, Local order in high-entropy alloys and associated deuterides – a total scattering and Reverse Monte Carlo study, *Acta Mater.* 199 (2020) 504–513, <https://doi.org/10.1016/j.actamat.2020.08.045>.

- [103] E. Antillon, C. Woodward, S.I. Rao, B. Akdim, T.A. Parthasarathy, Chemical short range order strengthening in a model FCC high entropy alloy, *Acta Mater.* 190 (2020) 29–42, <https://doi.org/10.1016/j.actamat.2020.02.041>.
- [104] A. Fernández-Caballero, J.S. Wróbel, P.M. Mummary, D. Nguyen-Manh, Short-range order in high entropy alloys: theoretical formulation and application to Mo-Nb-Ta-V-W system, *J. Phase Equilibria Diffus.* 38 (2017) 391–403, <https://doi.org/10.1007/s11669-017-0582-3>.
- [105] P. Singh, A. Marshal, A.V. Smirnov, A. Sharma, G. Balasubramanian, K. G. Pradeep, D.D. Johnson, Tuning phase stability and short-range order through Al doping in (CoCrFeMn)100-x A_x high-entropy alloys, *Phys. Rev. Mater.* 3 (2019) 1–9, <https://doi.org/10.1103/PhysRevMaterials.3.075002>.
- [106] J.B. Seol, J.W. Bae, J.G. Kim, H. Sung, Z. Li, H.H. Lee, S.H. Shim, J.H. Jang, W.-S. Ko, S.I. Hong, H.S. Kim, Short-range order strengthening in boron-doped high-entropy alloys for cryogenic applications, *Acta Mater.* 194 (2020) 366–377, <https://doi.org/10.1016/j.actamat.2020.04.052>.
- [107] S. Yin, J. Ding, M. Asta, R.O. Ritchie, Ab initio modeling of the energy landscape for screw dislocations in body-centered cubic high-entropy alloys, *Npj Comput. Mater.* 6 (2020) 110, <https://doi.org/10.1038/s41524-020-00377-5>.
- [108] Y. Ma, Q. Wang, C. Li, L.J. Santodonato, M. Feygenson, C. Dong, P.K. Liaw, Chemical short-range orders and the induced structural transition in high-entropy alloys, *Scr. Mater.* 144 (2018) 64–68, <https://doi.org/10.1016/j.scriptamat.2017.09.049>.
- [109] B. Gludovatz, A. Hohenwarter, D. Catoor, E.H. Chang, E.P. George, R.O. Ritchie, A fracture-resistant high-entropy alloy for cryogenic applications, *Science* 345 (2014) 1153–1158, <https://doi.org/10.1126/science.1254581>, 80.
- [110] K. Liu, S.S. Nene, M. Frank, S. Sinha, R.S. Mishra, Metastability-assisted fatigue behavior in a friction stir processed dual-phase high entropy alloy, *Mater. Res. Lett.* 6 (2018) 613–619, <https://doi.org/10.1080/21663831.2018.1523240>.
- [111] G.E. Dieter, Mechanical metallurgy, *Mech. Metall.* (2011), <https://doi.org/10.5962/bhl.title.35895>.
- [112] O.N. Senkov, J.M. Scott, S.V. Senkova, D.B. Miracle, C.F. Woodward, Microstructure and room temperature properties of a high-entropy TaNbHfZrTi alloy, *J. Alloys Compd.* 509 (2011) 6043–6048, <https://doi.org/10.1016/j.jallcom.2011.02.171>.
- [113] H. Mughrabi, *Treatise on Materials Science and Technology, Vol 6: Plastic Deformation and Fracture of Materials*, VCH, Cambridge, 1993.
- [114] M. Meyers, A. Engineering, S. Diego, E. Conferences, H. Senior, S. Award, T.M.S. D. Scientist, E. Awards, L.H. Award, K. Chawla, M. Science, *Mechanical Behavior of Materials*, 2009, pp. 46–6830, <https://doi.org/10.5860/choice>.
- [115] C. Varvenne, A. Luque, W.A. Curtin, Theory of strengthening in fcc high entropy alloys, *Acta Mater.* 118 (2016) 164–176, <https://doi.org/10.1016/j.actamat.2016.07.040>.
- [116] G. Bracq, M. Laurent-Brocq, C. Varvenne, L. Perrière, W.A. Curtin, J.M. Joubert, I. Guillot, Combining experiments and modeling to explore the solid solution strengthening of high and medium entropy alloys, *Acta Mater.* 177 (2019) 266–279, <https://doi.org/10.1016/j.actamat.2019.06.050>.
- [117] C.R. LaRosa, M. Shih, C. Varvenne, M. Ghazisaeidi, Solid solution strengthening theories of high-entropy alloys, *Mater. Char.* 151 (2019) 310–317, <https://doi.org/10.1016/j.matchar.2019.02.034>.
- [118] C. Varvenne, W.A. Curtin, Strengthening of high entropy alloys by dilute solute additions: CoCrFeNiAlx and CoCrFeNiMnAlx alloys, *Scr. Mater.* 138 (2017) 92–95, <https://doi.org/10.1016/j.scriptamat.2017.05.035>.
- [119] E.O. Hall, The deformation and ageing of mild steel: {III} discussion of results, *Proc. Phys. Soc. Sect. B* 64 (1951) 747–753, <https://doi.org/10.1088/0370-1301/64/9/303>.
- [120] J.N. Petch, The cleavage strength of polycrystals, *J. Iron Steel Inst.* 174 (1953) 25–28.
- [121] R.W. Armstrong, Y.T. Chou, R.A. Fisher, N. Louat, No title, *Philos. Mag.* 14 (1966) 943.
- [122] A.H. Chokshi, A. Rosen, J. Karch, H. Gleiter, On the validity of the hall-petch relationship in nanocrystalline materials, *Scr. Metall.* 23 (1989) 1679–1683, [https://doi.org/10.1016/0036-9748\(89\)90342-6](https://doi.org/10.1016/0036-9748(89)90342-6).
- [123] Z.C. Cordero, B.E. Knight, C.A. Schuh, Six decades of the Hall-Petch effect – a survey of grain-size strengthening studies on pure metals, *Int. Mater. Rev.* 61 (2016) 495–512, <https://doi.org/10.1080/09506608.2016.1191808>.
- [124] J.B. Seol, J.W. Bae, Z. Li, J. Chan Han, J.G. Kim, D. Raabe, H.S. Kim, Boron doped ultrastrong and ductile high-entropy alloys, *Acta Mater.* 151 (2018) 366–376, <https://doi.org/10.1016/j.actamat.2018.04.004>.
- [125] N.D. Stepanov, D.G. Shaysultanov, R.S. Chernichenko, N.Y. Yurchenko, S. V. Zherebtsov, M.A. Tikhonovsky, G.A. Salishchev, Effect of thermomechanical processing on microstructure and mechanical properties of the carbon-containing CoCrFeNiMn high entropy alloy, *J. Alloys Compd.* 693 (2017) 394–405, <https://doi.org/10.1016/j.jallcom.2016.09.208>.
- [126] Z. Wu, H. Bei, F. Otto, G.M. Pharr, E.P. George, Recovery, recrystallization, grain growth and phase stability of a family of FCC-structured multi-component equiatomic solid solution alloys, *Intermetallics* 46 (2014) 131–140, <https://doi.org/10.1016/j.intermet.2013.10.024>.
- [127] B. Gwalani, V. Soni, M. Lee, S.A. Mantri, Y. Ren, R. Banerjee, Optimizing the coupled effects of Hall-Petch and precipitation strengthening in a Al0.3CoCrFeNi high entropy alloy, *Mater. Des.* 121 (2017) 254–260, <https://doi.org/10.1016/j.matdes.2017.02.072>.
- [128] N. Kumar, M. Komarasamy, P. Nelaturu, Z. Tang, P.K. Liaw, R.S. Mishra, Friction stir processing of a high entropy alloy Al0.1CoCrFeNi, *Jom* 67 (2015) 1007–1013, <https://doi.org/10.1007/s11837-015-1385-9>.
- [129] R. Sriharitha, B.S. Murty, R.S. Kottada, Alloying, thermal stability and strengthening in spark plasma sintered AlxCoCrCuFeNi high entropy alloys, *J. Alloys Compd.* 583 (2014) 419–426, <https://doi.org/10.1016/j.jallcom.2013.08.176>.
- [130] B. Kang, J. Lee, H.J. Ryu, S.H. Hong, Ultra-high strength WNbMoTaV high-entropy alloys with fine grain structure fabricated by powder metallurgical process, *Mater. Sci. Eng. A* 712 (2018) 616–624, <https://doi.org/10.1016/j.msea.2017.12.021>.
- [131] S. Chen, K.K. Tseng, Y. Tong, W. Li, C.W. Tsai, J.W. Yeh, P.K. Liaw, Grain growth and Hall-Petch relationship in a refractory HfNbTaZrTi high-entropy alloy, *J. Alloys Compd.* 795 (2019) 19–26, <https://doi.org/10.1016/j.jallcom.2019.04.291>.
- [132] T.T. Shun, L.Y. Chang, M.H. Shiu, Microstructure and mechanical properties of multiprincipal component CoCrFeNiMo x alloys, *Mater. Char.* 70 (2012) 63–67, <https://doi.org/10.1016/j.matchar.2012.05.005>.
- [133] F. He, Z. Wang, P. Cheng, Q. Wang, J. Li, Y. Dang, J. Wang, C.T. Liu, Designing eutectic high entropy alloys of CoCrFeNiNb_x, *J. Alloys Compd.* 656 (2016) 284–289, <https://doi.org/10.1016/j.jallcom.2015.09.153>.
- [134] S. Niu, H. Kou, T. Guo, Y. Zhang, J. Wang, J. Li, Strengthening of nanoprecipitations in an annealed Al0.5CoCrFeNi high entropy alloy, *Mater. Sci. Eng. A* 671 (2016) 82–86, <https://doi.org/10.1016/j.msea.2016.06.040>.
- [135] Y. Tong, D. Chen, B. Han, J. Wang, R. Feng, T. Yang, C. Zhao, Y.L. Zhao, W. Guo, Y. Shimizu, C.T. Liu, P.K. Liaw, K. Inoue, Y. Nagai, A. Hu, J.J. Kai, Outstanding tensile properties of a precipitation-strengthened FeCoNiCrTi0.2 high-entropy alloy at room and cryogenic temperatures, *Acta Mater.* 165 (2019) 228–240, <https://doi.org/10.1016/j.actamat.2018.11.049>.
- [136] Y. Ma, Q. Wang, B.B. Jiang, C.L. Li, J.M. Hao, X.N. Li, C. Dong, T.G. Nieh, Controlled formation of coherent cuboidal nanoprecipitates in body-centered cubic high-entropy alloys based on Al2(Ni,Co,Fe,Cr)14 compositions, *Acta Mater.* 147 (2018) 213–225, <https://doi.org/10.1016/j.actamat.2018.01.050>.
- [137] S. Dasari, A. Jetagia, Y.J. Chang, V. Soni, B. Gwalani, S. Gorse, A.C. Yeh, R. Banerjee, Engineering multi-scale B2 precipitation in a heterogeneous FCC based microstructure to enhance the mechanical properties of a Al0.5Co1.5CrFeNi1.5 high entropy alloy, *J. Alloys Compd.* 830 (2020), 154707, <https://doi.org/10.1016/j.jallcom.2020.154707>.
- [138] S. Dasari, A. Sarkar, A. Sharma, B. Gwalani, D. Choudhuri, V. Soni, S. Manda, I. Samajdar, R. Banerjee, Recovery of cold-worked Al0.3CoCrFeNi complex concentrated alloy through twinning assisted B2 precipitation resulting in excellent strength-ductility combination, *Acta Mater.* (2020), <https://doi.org/10.1016/j.actamat.2020.10.071>.
- [139] H. Zhang, Y. He, Y. Pan, Enhanced hardness and fracture toughness of the laser-solidified FeCoNiCrCuTiMoAlSi0.5 high-entropy alloy by martensite strengthening, *Scr. Mater.* 69 (2013) 342–345, <https://doi.org/10.1016/j.scriptamat.2013.05.020>.
- [140] L. Wang, C. Fu, Y. Wu, R. Li, X. Hui, Y. Wang, Superelastic effect in Ti-rich high entropy alloys via stress-induced martensitic transformation, *Scr. Mater.* 162 (2019) 112–117, <https://doi.org/10.1016/j.scriptamat.2018.10.035>.
- [141] Z. Li, K.G. Pradeep, Y. Deng, D. Raabe, C.C. Tasan, Metastable high-entropy dual-phase alloys overcome the strength-ductility trade-off, *Nature* 534 (2016) 227–230, <https://doi.org/10.1038/nature17981>.
- [142] Z. Wu, H. Bei, G.M. Pharr, E.P. George, Temperature dependence of the mechanical properties of equiatomic solid solution alloys with face-centered cubic crystal structures, *Acta Mater.* 81 (2014) 428–441, <https://doi.org/10.1016/j.scriptamat.2014.08.026>.
- [143] J.W. Bae, J. Moon, M.J. Jang, D. Yim, D. Kim, S. Lee, H.S. Kim, Trade-off between tensile property and formability by partial recrystallization of CrMnFeCoNi high-entropy alloy, *Mater. Sci. Eng. A* 703 (2017) 324–330, <https://doi.org/10.1016/j.msea.2017.07.079>.
- [144] K.V.S. Thurston, A. Hohenwarter, G. Laplanche, E.P. George, B. Gludovatz, R. O. Ritchie, On the onset of deformation twinning in the CrFeMnCoNi high-entropy alloy using a novel tensile specimen geometry, *Intermetallics* 110 (2019), <https://doi.org/10.1016/j.intermet.2019.04.012>.
- [145] L.R. Owen, E.J. Pickering, H.Y. Playford, H.J. Stone, M.G. Tucker, N.G. Jones, An assessment of the lattice strain in the CrMnFeCoNi high-entropy alloy, *Acta Mater.* 122 (2017) 11–18, <https://doi.org/10.1016/j.actamat.2016.09.032>.
- [146] G.D. Sathiaraj, P.P. Bhattacharjee, C.W. Tsai, J.W. Yeh, Effect of heavy cryo-rolling on the evolution of microstructure and texture during annealing of equiatomic CoCrFeMnNi high entropy alloy, *Intermetallics* 69 (2016) 1–9, <https://doi.org/10.1016/j.intermet.2015.10.005>.
- [147] N. Gao, D.H. Lu, Y.Y. Zhao, X.W. Liu, G.H. Liu, Y. Wu, G. Liu, Z.T. Fan, Z.P. Lu, E. P. George, Strengthening of a CrMnFeCoNi high-entropy alloy by carbide precipitation, *J. Alloys Compd.* 792 (2019) 1028–1035, <https://doi.org/10.1016/j.jallcom.2019.04.121>.
- [148] B. Gludovatz, E.P. George, R.O. Ritchie, Processing, microstructure and mechanical properties of the CrMnFeCoNi high-entropy alloy, *Jom* 67 (2015) 2262–2270, <https://doi.org/10.1007/s11837-015-1589-z>.
- [149] J. Gu, M. Song, Annealing-induced abnormal hardening in a cold rolled CrMnFeCoNi high entropy alloy, *Scr. Mater.* 162 (2019) 345–349, <https://doi.org/10.1016/j.scriptamat.2018.11.042>.
- [150] Z.H. Han, S. Liang, J. Yang, R. Wei, C.J. Zhang, A superior combination of strength-ductility in CoCrFeNiMn high-entropy alloy induced by asymmetric rolling and subsequent annealing treatment, *Mater. Char.* 145 (2018) 619–626, <https://doi.org/10.1016/j.matchar.2018.09.029>.
- [151] Z. Li, S. Zhao, S. Alotaibi, Y. Liu, B. Wang, M.A. Meyers, Adiabatic shear localization in the CrMnFeCoNi high-entropy alloy, *Acta Mater.* 151 (2018) 424–431, <https://doi.org/10.1016/j.actamat.2018.03.040>.
- [152] G. Liu, D.H. Lu, X.W. Liu, F.C. Liu, Q. Yang, H. Du, Q. Hu, Z.T. Fan, Solute segregation effect on grain boundary migration and Hall-Petch relationship in

- CrMnFeCoNi high-entropy alloy, Mater. Sci. Technol. (United Kingdom). 35 (2019) 500–508, <https://doi.org/10.1080/02670836.2019.1570679>.
- [153] E.J. Pickering, R. Muñoz-Moreno, H.J. Stone, N.G. Jones, Precipitation in the equiatomic high-entropy alloy CrMnFeCoNi, Scr. Mater. 113 (2016) 106–109, <https://doi.org/10.1016/j.scriptamat.2015.10.025>.
- [154] G. Laplanche, J. Bonneville, C. Varvenne, W.A. Curtin, E.P. George, Thermal activation parameters of plastic flow reveal deformation mechanisms in the CrMnFeCoNi high-entropy alloy, Acta Mater. 143 (2018) 257–264, <https://doi.org/10.1016/j.actamat.2017.10.014>.
- [155] S.J. Sun, Y.Z. Tian, H.R. Lin, X.G. Dong, Y.H. Wang, Z.J. Wang, Z.F. Zhang, Temperature dependence of the Hall-Petch relationship in CoCrFeMnNi high-entropy alloy, J. Alloys Compd. 806 (2019) 992–998, <https://doi.org/10.1016/j.jallcom.2019.07.357>.
- [156] Z.J. Zhang, M.M. Mao, J. Wang, B. Gludovatz, Z. Zhang, S.X. Mao, E.P. George, Q. Yu, R.O. Ritchie, Nanoscale origins of the damage tolerance of the high-entropy alloy CrMnFeCoNi, Nat. Commun. 6 (2015) 2–7, <https://doi.org/10.1038/ncomms10143>.
- [157] N.L. Okamoto, S. Fujimoto, Y. Kambara, M. Kawamura, Z.M.T. Chen, H. Matsunoshita, K. Tanaka, H. Inui, E.P. George, Size effect, critical resolved shear stress, stacking fault energy, and solid solution strengthening in the CrMnFeCoNi high-entropy alloy, Sci. Rep. 6 (2016) 1–10, <https://doi.org/10.1038/srep35863>.
- [158] Z. Wu, Y. Gao, H. Bei, Thermal activation mechanisms and Labusch-type strengthening analysis for a family of high-entropy and equiatomic solid-solution alloys, Acta Mater. 120 (2016) 108–119, <https://doi.org/10.1016/j.actamat.2016.08.047>.
- [159] S.I. Hong, J. Moon, S.K. Hong, H.S. Kim, Thermally activated deformation and the rate controlling mechanism in CoCrFeMnNi high entropy alloy, Mater. Sci. Eng. A. 682 (2017) 569–576, <https://doi.org/10.1016/j.msea.2016.11.078>.
- [160] R. Labusch, A statistical theory of solid solution hardening, Phys. Status Solidi 41 (1970) 659–669, <https://doi.org/10.1002/pssb.19700410221>.
- [161] R. Labusch, Statistische theorien der mischkrystallhärtung, Acta Metall. 20 (1972) 917–927, [https://doi.org/10.1016/0001-6160\(72\)90085-5](https://doi.org/10.1016/0001-6160(72)90085-5).
- [162] L.A. Gypen, A. Deruyttere, Multi-component solid solution hardening, J. Mater. Sci. 12 (1977) 1028–1033, <https://doi.org/10.1007/BF00540987>.
- [163] I. Toda-Caraballo, P.E.J. Rivera-Díaz-del-Castillo, Modelling solid solution hardening in high entropy alloys, Acta Mater. 85 (2015) 14–23, <https://doi.org/10.1016/j.actamat.2014.11.014>.
- [164] I. Toda-Caraballo, J.S. Wróbel, S.L. Dudarev, D. Nguyen-Manh, P.E.J. Rivera-Díaz-del-Castillo, Interatomic spacing distribution in multicomponent alloys, Acta Mater. 97 (2015) 156–169, <https://doi.org/10.1016/j.actamat.2015.07.010>.
- [165] T.M. Smith, M.S. Hooshmand, B.D. Esser, F. Otto, D.W. Mccomb, E.P. George, M. Ghazisaeidi, M.J. Mills, Atomic-scale characterization and modeling of 60° dislocations in a high-entropy alloy, Acta Mater. 110 (2016) 352–363, <https://doi.org/10.1016/j.actamat.2016.03.045>.
- [166] X.D. Xu, P. Liu, Z. Tang, A. Hirata, S.X. Song, T.G. Nieh, P.K. Liaw, C.T. Liu, M.W. Chen, Transmission electron microscopy characterization of dislocation structure in a face-centered cubic high-entropy alloy Al0.1CoCrFeNi, Acta Mater. 144 (2018) 107–115, <https://doi.org/10.1016/j.actamat.2017.10.050>.
- [167] Q. Ding, Y. Zhang, X. Chen, X. Fu, D. Chen, S. Chen, L. Gu, F. Wei, H. Bei, Y. Gao, M. Wen, J. Li, Z. Zhang, T. Zhu, R.O. Ritchie, Q. Yu, Tuning element distribution, structure and properties by composition in high-entropy alloys, Nature 574 (2019) 223–227, <https://doi.org/10.1038/s41586-019-1617-1>.
- [168] J.W. Christian, S. Mahajan, Deformation twinning, Prog. Mater. Sci. 39 (1995) 1–157, [https://doi.org/10.1016/0079-6425\(94\)00007-7](https://doi.org/10.1016/0079-6425(94)00007-7).
- [169] J.B. Cohen, J. Weertman, A dislocation model for twinning in f.c.c. metals, Acta Metall. 11 (1963) 996–998, [https://doi.org/10.1016/0001-6160\(63\)90074-9](https://doi.org/10.1016/0001-6160(63)90074-9).
- [170] M. Niewczas, Dislocations and Twinning in Face Centred Cubic Crystals, 2007, [https://doi.org/10.1016/S1572-4859\(07\)80007-6](https://doi.org/10.1016/S1572-4859(07)80007-6).
- [171] T. Cai, Z.J. Zhang, P. Zhang, J.B. Yang, Z.F. Zhang, Competition between slip and twinning in face-centered cubic metals, J. Appl. Phys. 116 (2014), 163512, <https://doi.org/10.1063/1.4898319>.
- [172] E. El-Danaf, S.R. Kalidindi, R.D. Doherty, Influence of grain size and stacking-fault energy on deformation twinning in fcc metals, Metall. Mater. Trans. A Phys. Metall. Mater. Sci. 30 (1999) 1223–1233, <https://doi.org/10.1007/s11661-99-0272-9>.
- [173] D.T. Pierce, J.A. Jiménez, J. Bentley, D. Raabe, J.E. Wittig, The influence of stacking fault energy on the microstructural and strain-hardening evolution of Fe-Mn-Al-Si steels during tensile deformation, Acta Mater. 100 (2015) 178–190, <https://doi.org/10.1016/j.actamat.2015.08.030>.
- [174] D.T. Pierce, J. Bentley, J.A. Jiménez, J.E. Wittig, Stacking fault energy measurements of Fe-Mn-Al-Si austenitic twinning-induced plasticity steels, Scr. Mater. 66 (2012) 753–756, <https://doi.org/10.1016/j.scriptamat.2012.01.050>.
- [175] Y.Y. Wang, X. Sun, Y.D. Wang, X.H. Hu, H.M. Zbib, A mechanism-based model for deformation twinning in polycrystalline FCC steel, Mater. Sci. Eng. A. 607 (2014) 206–218, <https://doi.org/10.1016/j.msea.2014.04.010>.
- [176] O. Bouaziz, S. Allain, C. Scott, Effect of grain and twin boundaries on the hardening mechanisms of twinning-induced plasticity steels, Scr. Mater. 58 (2008) 484–487, <https://doi.org/10.1016/j.scriptamat.2007.10.050>.
- [177] Y. Gu, L.Q. Chen, T.W. Heo, L. Sandoval, J. Belak, Phase field model of deformation twinning in tantalum parameterization via molecular dynamics, Scr. Mater. 68 (2013) 451–454, <https://doi.org/10.1016/j.scriptamat.2012.11.022>.
- [178] S. Hu, C.H. Henager, L. Chen, Simulations of stress-induced twinning and detwinning: a phase field model, Acta Mater. 58 (2010) 6554–6564, <https://doi.org/10.1016/j.actamat.2010.08.020>.
- [179] S.L. Wong, M. Madivala, U. Prahl, F. Roters, D. Raabe, A crystal plasticity model for twinning- and transformation-induced plasticity, Acta Mater. 118 (2016) 140–151, <https://doi.org/10.1016/j.actamat.2016.07.032>.
- [180] B. Srinivas, A. Dhal, S.K. Panigrahi, A mathematical prediction model to establish the role of stacking fault energy on the cryo-deformation behavior of FCC materials at different strain levels, Int. J. Plast. 97 (2017) 159–177, <https://doi.org/10.1016/j.ijplas.2017.05.014>.
- [181] S. Allain, J.P. Chateau, O. Bouaziz, S. Migot, N. Guelton, Correlations between the calculated stacking fault energy and the plasticity mechanisms in Fe-Mn-C alloys, Mater. Sci. Eng. A. 387–389 (2004) 158–162, <https://doi.org/10.1016/j.msea.2004.01.059>.
- [182] Y.F. Shen, X.X. Li, X. Sun, Y.D. Wang, L. Zuo, Twinning and martensite in a 304 austenitic stainless steel, Mater. Sci. Eng. A. 552 (2012) 514–522, <https://doi.org/10.1016/j.msea.2012.05.080>.
- [183] D.T. Pierce, J.A. Jiménez, J. Bentley, D. Raabe, C. Oskay, J.E. Wittig, The influence of manganese content on the stacking fault and austenite-ε-martensite interfacial energies in Fe-Mn-(Al-Si) steels investigated by experiment and theory, Acta Mater. 68 (2014) 238–253, <https://doi.org/10.1016/j.actamat.2014.01.001>.
- [184] S. Kibey, J.B. Liu, D.D. Johnson, H. Sehitoglu, Predicting twinning stress in fcc metals: linking twin-energy pathways to twin nucleation, Acta Mater. 55 (2007) 6843–6851, <https://doi.org/10.1016/j.actamat.2007.08.042>.
- [185] G. Laplanche, A. Kostka, O.M. Horst, G. Eggeler, E.P. George, Microstructure evolution and critical stress for twinning in the CrMnFeCoNi high-entropy alloy, Acta Mater. 118 (2016) 152–163, <https://doi.org/10.1016/j.actamat.2016.07.038>.
- [186] T.K. Liu, Z. Wu, A.D. Stoica, Q. Xie, W. Wu, Y.F. Gao, H. Bei, K. An, Twinning-mediated work hardening and texture evolution in CrCoFeMnNi high entropy alloys at cryogenic temperature, Mater. Des. 131 (2017) 419–427, <https://doi.org/10.1016/j.matedes.2017.06.039>.
- [187] S. Huang, W. Li, E. Holmström, S.K. Kwon, O. Eriksson, L. Vitos, Plastic deformation transition in FeCrCoNiAlx high-entropy alloys, Mater. Res. Lett. 7 (2019) 439–445, <https://doi.org/10.1080/2163831.2019.1644683>.
- [188] S. Huang, H. Huang, W. Li, D. Kim, S. Lu, X. Li, E. Holmström, S.K. Kwon, L. Vitos, Twinning in metastable high-entropy alloys, Nat. Commun. 9 (2018) 1–7, <https://doi.org/10.1038/s41467-018-04780-x>.
- [189] J. Venables, The nucleation and propagation of deformation twins, J. Phys. Chem. Solids. 25 (1964) 693–700, [https://doi.org/10.1016/0022-3697\(64\)90178-7](https://doi.org/10.1016/0022-3697(64)90178-7).
- [190] S. Mahajan, G.Y. Chin, Formation of deformation twins in f.c.c. crystals, Acta Metall. 21 (1973) 1353–1363, [https://doi.org/10.1016/0001-6160\(73\)90085-0](https://doi.org/10.1016/0001-6160(73)90085-0).
- [191] H. Fujita, T. Mori, A formation mechanism of mechanical twins, in: F.C.C. Metals (Ed.), Scr. Metall. 9 (1975) 631–636, [https://doi.org/10.1016/0036-9748\(75\)90476-7](https://doi.org/10.1016/0036-9748(75)90476-7).
- [192] S. Muira, J. Takamura, N. N. Trans. Japan Inst. Met. Suppl. 9 (1975) 555.
- [193] H.D. Joo, H. Kato, M.J. Jang, J. Moon, C.W. Tsai, J.W. Yeh, H.S. Kim, Tensile deformation behavior and deformation twinning of an equimolar CoCrFeMnNi high-entropy alloy, Mater. Sci. Eng. A. 689 (2017) 122–133, <https://doi.org/10.1016/j.msea.2017.02.043>.
- [194] I.V. Kireeva, Y.I. Chumlyakov, Z.V. Pobedennaya, I.V. Kuksagausen, I. Karaman, Orientation dependence of twinning in single crystalline CoCrFeMnNi high-entropy alloy, Mater. Sci. Eng. A. 705 (2017) 176–181, <https://doi.org/10.1016/j.msea.2017.08.065>.
- [195] N. Stepanov, M. Tikhonovsky, N. Yurchenko, D. Zyabkin, M. Klimova, S. Zherebtsov, A. Efimov, G. Salishchev, Effect of cryo-deformation on structure and properties of CoCrFeNiMn high-entropy alloy, Intermetallics 59 (2015) 8–17, <https://doi.org/10.1016/j.intermet.2014.12.004>.
- [196] S.J. Sun, Y.Z. Tian, H.R. Lin, H.J. Yang, X.G. Dong, Y.H. Wang, Z.F. Zhang, Transition of twinning behavior in CoCrFeMnNi high entropy alloy with grain refinement, Mater. Sci. Eng. A. 712 (2018) 603–607, <https://doi.org/10.1016/j.msea.2017.12.022>.
- [197] K.M. Rahman, V.A. Vorontsov, D. Dye, The effect of grain size on the twin initiation stress in a TWIP steel, Acta Mater. 89 (2015) 247–257, <https://doi.org/10.1016/j.actamat.2015.02.008>.
- [198] R. Ueji, N. Tsuchida, D. Terada, N. Tsuji, Y. Tanaka, A. Takemura, K. Kunishige, Tensile properties and twinning behavior of high manganese austenitic steel with fine-grained structure, Scr. Mater. 59 (2008) 963–966, <https://doi.org/10.1016/j.scriptamat.2008.06.050>.
- [199] I. Gutierrez-Urrutia, S. Zaehlerer, D. Raabe, The effect of grain size and grain orientation on deformation twinning in a Fe-22wt.% Mn-0.6wt.% C TWIP steel, Mater. Sci. Eng. A. 527 (2010) 3552–3560, <https://doi.org/10.1016/j.msea.2010.02.041>.
- [200] R. Sidharth, W. Abuzaid, H. Sehitoglu, Nano-twinning enhanced room temperature fatigue crack growth in single crystalline CoCrFeMnNi high entropy alloy, Intermetallics 126 (2020), 106919, <https://doi.org/10.1016/j.intermet.2020.106919>.
- [201] T.N. Lam, S.Y. Lee, N.T. Tsou, H.S. Chou, B.H. Lai, Y.J. Chang, R. Feng, T. Kawasaki, S. Harjo, P.K. Liaw, A.C. Yeh, M.J. Li, R.F. Cai, S.C. Lo, E.W. Huang, Enhancement of fatigue resistance by overload-induced deformation twinning in a CoCrFeMnNi high-entropy alloy, Acta Mater. 201 (2020) 412–424, <https://doi.org/10.1016/j.actamat.2020.10.016>.
- [202] S.W. Wu, G. Wang, Y.D. Jia, J. Yi, Q.J. Zhai, C.T. Liu, B.A. Sun, H.J. Chu, J. Shen, P.K. Liaw, T.Y. Zhang, Enhancement of strength-ductility trade-off in a high-entropy alloy through a heterogeneous structure, Acta Mater. 165 (2019) 444–458, <https://doi.org/10.1016/j.actamat.2018.12.012>.
- [203] S.W. Wu, G. Wang, J. Yi, Y.D. Jia, I. Hussain, Q.J. Zhai, P.K. Liaw, Strong grain-size effect on deformation twinning of an Al0.1CoCrFeNi high-entropy alloy,

- Mater. Res. Lett. 5 (2017) 276–283, <https://doi.org/10.1080/21663831.2016.1257514>.
- [204] N. Kumar, Q. Ying, X. Nie, R.S. Mishra, Z. Tang, P.K. Liaw, R.E. Brennan, K. J. Doherty, K.C. Cho, High strain-rate compressive deformation behavior of the Al0.1CrFeCoNi high entropy alloy, Mater. Des. 86 (2015) 598–602, <https://doi.org/10.1016/j.matdes.2015.07.161>.
- [205] S. Gangireddy, D. Whitaker, R.S. Mishra, Significant contribution to strength enhancement from deformation twins in thermomechanically processed Al0.1CoCrFeNi microstructures, J. Mater. Eng. Perform. 28 (2019) 1661–1667, <https://doi.org/10.1007/s11665-019-3885-1>.
- [206] S. Gangireddy, L. Kaimiao, B. Gwalani, R. Mishra, Microstructural dependence of strain rate sensitivity in thermomechanically processed Al0.1CoCrFeNi high entropy alloy, Mater. Sci. Eng. A. 727 (2018) 148–159, <https://doi.org/10.1016/j.msea.2018.04.108>.
- [207] S. Gangireddy, B. Gwalani, R.S. Mishra, Grain size dependence of strain rate sensitivity in a single phase FCC high entropy alloy Al0.3CoCrFeNi, Mater. Sci. Eng. A. 736 (2018) 344–348, <https://doi.org/10.1016/j.msea.2018.09.009>.
- [208] S. Gangireddy, B. Gwalani, K. Liu, R. Banerjee, R.S. Mishra, Microstructures with extraordinary dynamic work hardening and strain rate sensitivity in Al0.3CoCrFeNi high entropy alloy, Mater. Sci. Eng. A. 734 (2018) 42–50, <https://doi.org/10.1016/j.msea.2018.07.088>.
- [209] S. Gangireddy, B. Gwalani, R. Banerjee, R.S. Mishra, High strain rate response of Al0.7CoCrFeNi high entropy alloy: dynamic strength over 2 GPa from thermomechanical processing and hierarchical microstructure, J. Dyn. Behav. Mater. 5 (2019), <https://doi.org/10.1007/s40870-018-00178-4>.
- [210] A. Rohatgi, K.S. Vecchio, G.T. Gray, The influence of stacking fault energy on the mechanical behavior of Cu and Cu-al alloys: deformation twinning, work hardening, and dynamic recovery, Metall. Mater. Trans. A Phys. Metall. Mater. Sci. 32 (2001) 135–145, <https://doi.org/10.1007/s11661-001-0109-7>.
- [211] W.S. Yang, C.M. Wan, The influence of aluminium content to the stacking fault energy in Fe-Mn-Al-C alloy system, J. Mater. Sci. 25 (1990) 1821–1823, <https://doi.org/10.1007/BF01045392>.
- [212] Z. Li, C.C. Tasan, H. Springer, B. Gault, D. Raabe, Interstitial atoms enable joint twinning and transformation induced plasticity in strong and ductile high-entropy alloys, Sci. Rep. 7 (2017) 1–7, <https://doi.org/10.1038/srep40704>.
- [213] Y. Deng, C.C. Tasan, K.G. Pradeep, H. Springer, A. Kostka, D. Raabe, Design of a twinning-induced plasticity high entropy alloy, Acta Mater. 94 (2015) 124–133, <https://doi.org/10.1016/j.actamat.2015.04.014>.
- [214] Y.H. Jo, S. Jung, W.M. Choi, S.S. Sohn, H.S. Kim, B.J. Lee, N.J. Kim, S. Lee, Cryogenic strength improvement by utilizing room-temperature deformation twinning in a partially recrystallized VCrMnFeCoNi high-entropy alloy, Nat. Commun. 8 (2017) 1–8, <https://doi.org/10.1038/ncomms15719>.
- [215] S. Sinha, M. Komarasamy, T. Wang, R.S. Haridas, P. Agrawal, S. Shukla, S. Thapliyal, M. Frank, R.S. Mishra, Notch-tensile behavior of Al0.1CrFeCoNi high entropy alloy, Mater. Sci. Eng. A. 774 (2020), 138918, <https://doi.org/10.1016/j.msea.2020.138918>.
- [216] S. Sinha, S.S. Nene, M. Frank, K. Liu, P. Agrawal, R.S. Mishra, On the evolving nature of c/a ratio in a hexagonal close-packed epsilon martensite phase in transformative high entropy alloys, Sci. Rep. 9 (2019) 1–14, <https://doi.org/10.1038/s41598-019-49904-5>.
- [217] O. Grässel, G. Frommeyer, C. Derder, H. Hofmann, Phase transformations and mechanical properties of Fe-Mn-Si-Al TRIP-steels, J. Phys. IV JP 7 (1997) 1–6, <https://doi.org/10.1051/jp4:1997560>.
- [218] M.F. Buchely, D.M. Field, D.C. Van Aken, Analysis of hot- and cold-rolled loads in medium-Mn TRIP steels, Metall. Mater. Trans. B Process Metall. Mater. Process. Sci. 50 (2019) 1180–1192, <https://doi.org/10.1007/s11663-019-01566-4>.
- [219] F.X. Yin, H. Xia, J.H. Feng, M.H. Cai, X. Zhang, G.K. Wang, T. Sawaguchi, Mechanical properties of an Fe-30Mn-4Si-2Al alloy after rolling at different temperatures ranging from 298 to 1073 K, Mater. Sci. Eng. A. 725 (2018) 127–137, <https://doi.org/10.1016/j.msea.2018.03.079>.
- [220] G. Frommeyer, U. Brüx, P. Neumann, Supra-ductile and high-strength manganese-TRIP/TWIP steels for high energy absorption purposes, ISIJ Int. 43 (2003) 438–446, <https://doi.org/10.2355/isijinternational.43.438>.
- [221] Y. Tomota, M. Strum, J.W. Morris, Tensile deformation behavior of mechanically stabilized Fe-Mn austenite, Metall. Trans. A. 19 (1988) 1563–1568, <https://doi.org/10.1007/BF02674030>.
- [222] D. Bhandarkar, V.F. Zackay, E.R. Parker, Stability and mechanical properties of some metastable austenitic steels, Metall. Trans. 3 (1972) 2619–2631, <https://doi.org/10.1007/BF02644238>.
- [223] V.F. Zackay, E.R. Parker, D. Fahr, R. Busch, The enhancement of ductility in high-strength steels, ASM Trans. Quart. 60 (1967) 252–259.
- [224] D.M. Field, D.C. Van Aken, Dynamic strain aging phenomena and tensile response of medium-Mn TRIP steel, Metall. Mater. Trans. A Phys. Metall. Mater. Sci. 49 (2018) 1152–1166, <https://doi.org/10.1007/s11661-018-4481-y>.
- [225] D.M. Field, J. Qing, D.C. Van Aken, Chemistry and properties of medium-Mn two-stage TRIP steels, Metall. Mater. Trans. A Phys. Metall. Mater. Sci. 49 (2018) 4615–4632, <https://doi.org/10.1007/s11661-018-4798-6>.
- [226] L. Rémy, A. Pineau, Twinning and strain-induced f.c.c. → h.c.p. transformation on the mechanical properties of CoNiCrMo alloys, Mater. Sci. Eng. 26 (1976) 123–132, [https://doi.org/10.1016/0025-5416\(76\)90234-2](https://doi.org/10.1016/0025-5416(76)90234-2).
- [227] J.F. Breedis, L. Kaufman, Formation of Hcp and Bcc phases in ausleititic iron alloys, Metall. Mater. Trans. B 2 (1971), <https://doi.org/10.1007/bf02814993>, 3249–3249.
- [228] S.T. Pisarik, D.C. Van Aken, Thermodynamic driving force of the $\gamma \rightarrow \epsilon$ transformation and resulting MS temperature in high-Mn steels, Metall. Mater. Trans. A Phys. Metall. Mater. Sci. 47 (2016) 1009–1018, <https://doi.org/10.1007/s11661-015-3265-x>.
- [229] Z. Li, D. Raabe, Strong and ductile non-equiautomic high-entropy alloys: design, processing, microstructure, and mechanical properties, Jom 69 (2017) 2099–2106, <https://doi.org/10.1007/s11837-017-2540-2>.
- [230] Z. Li, C.C. Tasan, K.G. Pradeep, D. Raabe, A TRIP-assisted dual-phase high-entropy alloy: grain size and phase fraction effects on deformation behavior, Acta Mater. 131 (2017) 323–335, <https://doi.org/10.1016/j.actamat.2017.03.069>.
- [231] R. Xiong, H. Peng, H. Si, W. Zhang, Y. Wen, Thermodynamic calculation of stacking fault energy of the Fe-Mn-Si-C high manganese steels, Mater. Sci. Eng. A. 598 (2014) 376–386, <https://doi.org/10.1016/j.msea.2014.01.046>.
- [232] S. Sinha, S.S. Nene, M. Frank, K. Liu, R.S. Mishra, B.A. McWilliams, K.C. Cho, Revealing the microstructural evolution in a high entropy alloy enabled with transformation, twinning and precipitation, Materialia 6 (2019), 100310, <https://doi.org/10.1016/j.jmtla.2019.100310>.
- [233] W. Lu, C.H. Liebscher, G. Dehm, D. Raabe, Z. Li, Bidirectional transformation enables hierarchical nanolaminate dual-phase high-entropy alloys, Adv. Mater. 30 (2018) 1–10, <https://doi.org/10.1002/adma.201804727>.
- [234] G.B. Olson, M. Cohen, A general mechanism of martensitic nucleation: Part I. General concepts and the FCC → HCP transformation, Metall. Trans. A. 7 (1976) 1897–1904, <https://doi.org/10.1007/BF02659822>.
- [235] S.S. Nene, M. Frank, P. Agrawal, S. Sinha, K. Liu, S. Shukla, R.S. Mishra, B. A. McWilliams, K.C. Cho, Microstructurally flexible high entropy alloys: linkages between alloy design and deformation behavior, Mater. Des. 194 (2020), 108968, <https://doi.org/10.1016/j.matdes.2020.108968>.
- [236] W. Li, S. Chen, P.K. Liaw, Discovery and design of fatigue-resistant high-entropy alloys, Scr. Mater. 187 (2020) 68–75, <https://doi.org/10.1016/j.scriptamat.2020.05.047>.
- [237] T. Niendorf, T. Wegener, Z. Li, D. Raabe, Unexpected cyclic stress-strain response of dual-phase high-entropy alloys induced by partial reversibility of deformation, Scr. Mater. 143 (2018) 63–67, <https://doi.org/10.1016/j.scriptamat.2017.09.013>.
- [238] R.S. Haridas, P. Agrawal, S. Thapliyal, S. Yadav, Strain rate sensitive microstructural evolution in a TRIP assisted high entropy alloy : experiments , microstructure and modeling, Mech. Mater. 156 (2021), 103798, <https://doi.org/10.1016/j.mechmat.2021.103798>.
- [239] S. Wei, J. Kim, C.C. Tasan, Boundary micro-cracking in metastable Fe45Mn35Co10Cr10 high-entropy alloys, Acta Mater. 168 (2019) 76–86, <https://doi.org/10.1016/j.actamat.2019.01.036>.
- [240] N. Stanford, D.P. Dunne, Effect of Si on the reversibility of stress-induced martensite in Fe-Mn-Si shape memory alloys, Acta Mater. 58 (2010) 6752–6762, <https://doi.org/10.1016/j.actamat.2010.08.041>.
- [241] S. Sinha, S.S. Nene, M. Frank, K. Liu, R.A. Lebensohn, R.S. Mishra, Deformation mechanisms and ductile fracture characteristics of a friction stir processed transformative high entropy alloy, Acta Mater. 184 (2020) 164–178, <https://doi.org/10.1016/j.actamat.2019.11.056>.
- [242] M. Frank, Y. Chen, S.S. Nene, S. Sinha, K. Liu, K. An, R.S. Mishra, Investigating the deformation mechanisms of a highly metastable high entropy alloy using in-situ neutron diffraction, Mater. Today Commun. 23 (2020), 100858, <https://doi.org/10.1016/j.jtc.2019.100858>.
- [243] S. Fu, H. Bei, Y. Chen, T.K. Liu, D. Yu, K. An, Deformation mechanisms and work-hardening behavior of transformation-induced plasticity high entropy alloys by in -situ neutron diffraction, Mater. Res. Lett. 6 (2018) 620–626, <https://doi.org/10.1080/21663831.2018.1523239>.
- [244] M. Frank, S.S. Nene, Y. Chen, B. Gwalani, E.J. Kautz, A. Devaraj, K. An, R. S. Mishra, Correlating work hardening with co-activation of stacking fault strengthening and transformation in a high entropy alloy using in-situ neutron diffraction, Sci. Rep. 10 (2020) 1–10, <https://doi.org/10.1038/s41598-020-79492-8>.
- [245] Y. Zou, H. Ma, R. Spolenak, Ultrastrong ductile and stable high-entropy alloys at small scales, Nat. Commun. 6 (2015), <https://doi.org/10.1038/ncomms748>.
- [246] O.N. Senkov, G.B. Wilks, D.B. Miracle, C.P. Chuang, P.K. Liaw, Refractory high-entropy alloys, Intermetallics 18 (2010) 1758–1765, <https://doi.org/10.1016/j.intermet.2010.05.014>.
- [247] L. Qi, D.C. Chrzan, Tuning ideal tensile strengths and intrinsic ductility of bcc refractory alloys, Phys. Rev. Lett. 112 (2014) 1–5, <https://doi.org/10.1103/PhysRevLett.112.115503>.
- [248] Y.T. Zhu, X.Z. Liao, X.L. Wu, Deformation twinning in nanocrystalline materials, Prog. Mater. Sci. 57 (2012) 1–62, <https://doi.org/10.1016/j.scriptamat.2011.05.001>.
- [249] G. Dirras, L. Lilenstein, P. Djemba, M. Laurent-Brocq, D. Tingaud, J.P. Couzinié, L. Perrière, T. Chauveau, I. Guillot, Elastic and plastic properties of as-cast equimolar TiHfZrTaNb high-entropy alloy, Mater. Sci. Eng. A. 654 (2016) 30–38, <https://doi.org/10.1016/j.msea.2015.12.017>.
- [250] Y.D. Wu, Y.H. Cai, T. Wang, J.J. Si, J. Zhu, Y.D. Wang, X.D. Hui, A refractory Hf25Nb25Ti25Zr25 high-entropy alloy with excellent structural stability and tensile properties, Mater. Lett. 130 (2014) 277–280, <https://doi.org/10.1016/j.matlet.2014.05.134>.
- [251] S. Sheikh, S. Shafeie, Q. Hu, J. Ahlström, C. Persson, J. Veselý, J. Zýka, U. Klement, S. Guo, Alloy design for intrinsically ductile refractory high-entropy alloys, J. Appl. Phys. 120 (2016), <https://doi.org/10.1063/1.4966659>.
- [252] Pergamon materials series, in: D. Caillard, J.L. Martin (Eds.), Therm. Act. Mech. Cryst. Plast., Pergamon, 2003, [https://doi.org/10.1016/S1470-1804\(13\)60015-2](https://doi.org/10.1016/S1470-1804(13)60015-2).
- [253] L. Lilenstein, J.P. Couzinié, L. Perrière, A. Hocini, C. Keller, G. Dirras, I. Guillot, Study of a bcc multi-principal element alloy: tensile and simple shear properties

- and underlying deformation mechanisms, *Acta Mater.* 142 (2018) 131–141, <https://doi.org/10.1016/j.actamat.2017.09.062>.
- [254] J.P. Couzinié, L. Lilenstein, Y. Champion, G. Dirras, L. Perrière, I. Guillot, On the room temperature deformation mechanisms of a TiZrHfNbTa refractory high-entropy alloy, *Mater. Sci. Eng. A* 645 (2015) 255–263, <https://doi.org/10.1016/j.msea.2015.08.024>.
- [255] Y. Zou, S. Maiti, W. Steurer, R. Spolenak, Size-dependent plasticity in an Nb₂₅Mo₂₅Ta₂₅W₂₅ refractory high-entropy alloy, *Acta Mater.* 65 (2014) 85–97, <https://doi.org/10.1016/j.actamat.2013.11.049>.
- [256] S.I. Rao, C. Varvenne, C. Woodward, T.A. Parthasarathy, D. Miracle, O.N. Senkov, W.A. Curtin, Atomistic simulations of dislocations in a model BCC multicomponent concentrated solid solution alloy, *Acta Mater.* 125 (2017) 311–320, <https://doi.org/10.1016/j.actamat.2016.12.011>.
- [257] A.V. Podolskiy, E.D. Tabachnikova, V.V. Voloschuk, V.F. Gorban, N.A. Krapivka, S.A. Firstov, Mechanical properties and thermally activated plasticity of the Ti₃₀Zr₂₅Hf₁₅Nb₂₀Ta₁₀ high entropy alloy at temperatures 4.2–350 K, *Mater. Sci. Eng. A* 710 (2018) 136–141, <https://doi.org/10.1016/j.msea.2017.10.073>.
- [258] G. Dirras, H. Couque, L. Lilenstein, A. Heczel, D. Tingaud, J.P. Couzinié, L. Perrière, J. Gubicza, I. Guillot, Mechanical behavior and microstructure of Ti₂₀Hf₂₀Ta₂₀Nb₂₀ high-entropy alloy loaded under quasi-static and dynamic compression conditions, *Mater. Charact.* 111 (2016) 106–113, <https://doi.org/10.1016/j.matchar.2015.11.018>.
- [259] O.N. Senkov, S.L. Semiatin, Microstructure and properties of a refractory high-entropy alloy after cold working, *J. Alloys Compd.* 649 (2015) 1110–1123, <https://doi.org/10.1016/j.jallcom.2015.07.209>.
- [260] Z. Lei, X. Liu, Y. Wu, H. Wang, S. Jiang, S. Wang, X. Hui, Y. Wu, B. Gault, P. Kontis, D. Raabe, L. Gu, Q. Zhang, H. Chen, H. Wang, J. Liu, K. An, Q. Zeng, T. G. Nieh, Z. Lu, Enhanced strength and ductility in a high-entropy alloy via ordered oxygen complexes, *Nature* 563 (2018) 546–550, <https://doi.org/10.1038/s41598-018-0685-y>.
- [261] H. Huang, Y. Wu, J. He, H. Wang, X. Liu, K. An, W. Wu, Z. Lu, Phase-transformation ductilization of brittle high-entropy alloys via metastability engineering, *Adv. Mater.* 29 (2017) 1–7, <https://doi.org/10.1002/adma.201701678>.
- [262] L. Lilenstein, J.P. Couzinié, J. Bourgon, L. Perrière, G. Dirras, F. Prima, I. Guillot, Design and tensile properties of a bcc Ti-rich high-entropy alloy with transformation-induced plasticity, *Mater. Res. Lett.* 5 (2017) 110–116, <https://doi.org/10.1080/21663831.2016.1221861>.
- [263] M. Abdel-Hady, K. Hinoshita, M. Morinaga, General approach to phase stability and elastic properties of β -type Ti-alloys using electronic parameters, *Scr. Mater.* 55 (2006) 477–480, <https://doi.org/10.1016/j.scriptamat.2006.04.022>.
- [264] R.R. Eletti, M. Klimova, M. Tikhonovsky, N. Stepanov, S. Zherebtsov, Exceptionally high strain-hardening and ductility due to transformation induced plasticity effect in Ti-rich high-entropy alloys, *Sci. Rep.* 10 (2020) 1–8, <https://doi.org/10.1038/s41598-020-70298-2>.
- [265] Y.J. Zhao, J.W. Qiao, S.G. Ma, M.C. Gao, H.J. Yang, M.W. Chen, Y. Zhang, A hexagonal close-packed high-entropy alloy: the effect of entropy, *Mater. Des.* 96 (2016) 10–15, <https://doi.org/10.1016/j.matdes.2016.01.149>.
- [266] F. Czerwinski Rogal, P.T. Jochym, L. Litynska-Dobrzynska, Microstructure and mechanical properties of the novel Hf₂₅Sc₂₅Ti₂₅Zr₂₅ equiatomic alloy with hexagonal solid solutions, *Mater. Des.* 92 (2016) 8–17, <https://doi.org/10.1016/j.matdes.2015.11.104>.
- [267] Z. Zhang, E. Axinte, W. Ge, C. Shang, Y. Wang, Microstructure, mechanical properties and corrosion resistance of CuZrY/Al, Ti, Hf series high-entropy alloys, *Mater. Des.* 108 (2016) 106–113, <https://doi.org/10.1016/j.matdes.2016.06.100>.
- [268] C.L. Tracy, S. Park, D.R. Rittman, S.J. Zinkle, H. Bei, M. Lang, R.C. Ewing, W. L. Mao, High pressure synthesis of a hexagonal close-packed phase of the high-entropy alloy CrMnFeCoNi, *Nat. Commun.* 8 (2017) 1–6, <https://doi.org/10.1038/ncomms15634>.
- [269] Micheal F. Ashby, Materials selection in mechanical design, in: Micheal F. Ashby (Ed.), *Mater. Sel. Mech. Des.*, Elsevier, 2011, <https://doi.org/10.1016/B978-1-85617-663-7.00026-6>.
- [270] J. Yang, J.W. Qiao, S.G. Ma, G.Y. Wu, D. Zhao, Z.H. Wang, Revealing the Hall-Petch relationship of Al_{0.1}CoCrFeNi high-entropy alloy and its deformation mechanisms, *J. Alloys Compd.* 795 (2019) 269–274, <https://doi.org/10.1016/j.jallcom.2019.04.333>.
- [271] R.S. Mishra, S.S. Nene, Some unique aspects of mechanical behavior of metastable transformative high entropy alloys, *Metall. Mater. Trans. A* 52 (2021) 889–896, <https://doi.org/10.1007/s11661-021-06138-3>.
- [272] S. Xia, Y. Zhang, Deformation mechanisms of Al_{0.1}CoCrFeNi high entropy alloy at ambient and cryogenic temperatures, *Mater. Sci. Eng. A* 733 (2018) 408–413, <https://doi.org/10.1016/j.msea.2018.07.073>.
- [273] D. Choudhuri, B. Gwalani, S. Gorsee, M. Komarasamy, S.A. Mantri, S. G. Srinivasan, R.S. Mishra, R. Banerjee, Enhancing strength and strain hardenability via deformation twinning in fcc-based high entropy alloys reinforced with intermetallic compounds, *Acta Mater.* 165 (2019) 420–430, <https://doi.org/10.1016/j.actamat.2018.12.010>.
- [274] Y. Lu, X. Gao, L. Jiang, Z. Chen, T. Wang, J. Jie, H. Kang, Y. Zhang, S. Guo, H. Ruan, Y. Zhao, Z. Cao, T. Li, Directly cast bulk eutectic and near-eutectic high entropy alloys with balanced strength and ductility in a wide temperature range, *Acta Mater.* 124 (2017) 143–150, <https://doi.org/10.1016/j.actamat.2016.11.016>.
- [275] I.S. Wani, T. Bhattacharjee, S. Sheikh, P.P. Bhattacharjee, S. Guo, N. Tsuji, Tailoring nanostructures and mechanical properties of AlCoCrFeNi_{2.1} eutectic high entropy alloy using thermo-mechanical processing, *Mater. Sci. Eng. A* 675 (2016) 99–109, <https://doi.org/10.1016/j.msea.2016.08.048>.
- [276] Q. Wang, Y. Ma, B. Jiang, X. Li, Y. Shi, C. Dong, P.K. Liaw, A cuboidal B₂ nanoprecipitation-enhanced body-centered-cubic alloy Al_{0.7}CoCrFe₂Ni with prominent tensile properties, *Scr. Mater.* 120 (2016) 85–89, <https://doi.org/10.1016/j.scriptamat.2016.04.014>.
- [277] Z.G. Wang, W. Zhou, L.M. Fu, J.F. Wang, R.C. Luo, X.C. Han, B. Chen, X.D. Wang, Effect of coherent L1₂ nanoprecipitates on the tensile behavior of a fcc-based high-entropy alloy, *Mater. Sci. Eng. A* 696 (2017) 503–510, <https://doi.org/10.1016/j.msea.2017.04.111>.
- [278] C. Zhang, C. Zhu, P. Cao, X. Wang, F. Ye, K. Kaufmann, L. Casalena, B. E. MacDonald, X. Pan, K. Vecchio, E.J. Lavernia, Aged metastable high-entropy alloys with heterogeneous lamella structure for superior strength-ductility synergy, *Acta Mater.* 199 (2020) 602–612, <https://doi.org/10.1016/j.actamat.2020.08.043>.
- [279] Y.L. Zhao, T. Yang, Y.R. Li, L. Fan, B. Han, Z.B. Jiao, D. Chen, C.T. Liu, J.J. Kai, Superior high-temperature properties and deformation-induced planar faults in a novel L1₂-strengthened high-entropy alloy, *Acta Mater.* 188 (2020) 517–527, <https://doi.org/10.1016/j.actamat.2020.02.028>.
- [280] T. Yang, Y.L. Zhao, L. Fan, J. Wei, J.H. Luan, W.H. Liu, C. Wang, Z.B. Jiao, J. J. Kai, C.T. Liu, Control of nanoscale precipitation and elimination of intermediate-temperature embrittlement in multicomponent high-entropy alloys, *Acta Mater.* 189 (2020) 47–59, <https://doi.org/10.1016/j.actamat.2020.02.059>.
- [281] Y.Y. Zhao, H.W. Chen, Z.P. Lu, T.G. Nieh, Thermal stability and coarsening of coherent particles in a precipitation-hardened (NiCoFeCr)94Ti2Al4 high-entropy alloy, *Acta Mater.* 147 (2018) 184–194, <https://doi.org/10.1016/j.actamat.2018.01.049>.
- [282] P. Pandey, S. Kashyap, D. Palanisamy, A. Sharma, K. Chattopadhyay, On the high temperature coarsening kinetics of γ' precipitates in a high strength Co_{37.6}Ni_{35.4}Al_{9.9}Mo_{4.9}Cr_{5.9}Ta_{2.8}Ti_{3.5} fcc-based high entropy alloy, *Acta Mater.* 177 (2019) 82–95, <https://doi.org/10.1016/j.actamat.2019.07.011>.
- [283] R. Mishra, Z. Ma, I. Charit, Friction stir processing: a novel technique for fabrication of surface composite, *Mater. Sci. Eng. A* 341 (2003) 307–310, [https://doi.org/10.1016/S0921-5093\(02\)00199-5](https://doi.org/10.1016/S0921-5093(02)00199-5).
- [284] R.S. Mishra, P.S. De, N. Kumar, *Friction Stir Welding and Processing*, Springer International Publishing, Cham, 2014, <https://doi.org/10.1007/978-3-319-07043-8>.
- [285] R.S. Mishra, Z.Y. Ma, Friction stir welding and processing, *Mater. Sci. Eng. R Reports* 50 (2005) 1–78, <https://doi.org/10.1016/j.mser.2005.07.001>.
- [286] J.Q. Su, T.W. Nelson, R. Mishra, M. Mahoney, Microstructural investigation of friction stir welded 7050-T651 aluminium, *Acta Mater.* 51 (2003) 713–729, [https://doi.org/10.1016/S1359-6454\(02\)00449-4](https://doi.org/10.1016/S1359-6454(02)00449-4).
- [287] Z. Ma, R. Mishra, M. Mahoney, Superplastic deformation behaviour of friction stir processed 7075Al alloy, *Acta Mater.* 50 (2002) 4419–4430, [https://doi.org/10.1016/S1359-6454\(02\)00278-1](https://doi.org/10.1016/S1359-6454(02)00278-1).
- [288] Z.Y. Ma, R.S. Mishra, M.W. Mahoney, Superplasticity in cast A356 induced via friction stir processing, *Scr. Mater.* 50 (2004) 931–935, <https://doi.org/10.1016/j.scriptamat.2004.01.012>.
- [289] W. Yuan, R.S. Mishra, Grain size and texture effects on deformation behavior of AZ31 magnesium alloy, *Mater. Sci. Eng. A* 558 (2012) 716–724, <https://doi.org/10.1016/j.msea.2012.08.080>.
- [290] W. Yuan, R.S. Mishra, B. Carlson, R.K. Mishra, R. Verma, R. Kubic, Effect of texture on the mechanical behavior of ultrafine grained magnesium alloy, *Scr. Mater.* 64 (2011) 580–583, <https://doi.org/10.1016/j.scriptamat.2010.11.052>.
- [291] M. Ghosh, K. Kumar, R.S. Mishra, Analysis of microstructural evolution during friction stir welding of ultrahigh-strength steel, *Scr. Mater.* 63 (2010) 851–854, <https://doi.org/10.1016/j.scriptamat.2010.06.032>.
- [292] O.O. Tinubu, S. Das, A. Dutt, J.E. Mogonye, V. Ageh, R. Xu, J. Forsdike, R. S. Mishra, T.W. Scharf, Friction stir processing of A-286 stainless steel: microstructural evolution during wear, *Wear* 356–357 (2016) 94–100, <https://doi.org/10.1016/j.wear.2016.03.018>.
- [293] J.C. Lippold, J.M. Rodelas, J.R. Rule, Friction stir processing of Ni-base alloys, in: Proc. 1st Int. Symp. Join. Weld., Elsevier, 2013, pp. 369–376, <https://doi.org/10.1533/9781-78242-164-1-369>.
- [294] A.I. Pilchak, M.C. Juhas, J.C. Williams, Microstructural changes due to friction stir processing of investment-cast Ti-6Al-4V, *Mettal. Mater. Trans. A Phys. Metall. Mater. Sci.* 38 (2007) 401–408, <https://doi.org/10.1007/s11661-006-9061-x>.
- [295] S. Mironov, Y.S. Sato, H. Kokawa, Friction-stir welding and processing of Ti-6Al-4V titanium alloy: a review, *J. Mater. Sci. Technol.* 34 (2018) 58–72, <https://doi.org/10.1016/j.jmst.2017.10.018>.
- [296] Z. Ding, Q. Fan, L. Wang, A review on friction stir processing of titanium alloy: characterization, method, microstructure, properties, *Mettal. Mater. Trans. B* 50 (2019) 2134–2162, <https://doi.org/10.1007/s11663-019-01634-9>.
- [297] M. Komarasamy, N. Kumar, Z. Tang, R.S. Mishra, P.K. Liaw, Effect of microstructure on the deformation mechanism of friction stir-processed Al 0.1 CoCrFeNi high entropy alloy, *Mater. Res. Lett.* 3 (2015) 30–34, <https://doi.org/10.1080/21663831.2014.958586>.
- [298] S. Basu, Z. Li, K.G. Pradeep, D. Raabe, Strain rate sensitivity of a TRIP-assisted dual-phase high-entropy alloy, *Front. Mater.* 5 (2018) 1–10, <https://doi.org/10.3389/fmats.2018.00030>.
- [299] S.F. Liu, Y. Wu, H.T. Wang, W.T. Lin, Y.Y. Shang, J.B. Liu, K. An, X.J. Liu, H. Wang, Z.P. Lu, Transformation-reinforced high-entropy alloys with superior mechanical properties via tailoring stacking fault energy, *J. Alloys Compd.* 792 (2019) 444–455, <https://doi.org/10.1016/j.jallcom.2019.04.035>.
- [300] S. Chen, H.S. Oh, B. Gludovatz, S.J. Kim, E.S. Park, Z. Zhang, R.O. Ritchie, Q. Yu, Real-time observations of TRIP-induced ultrahigh strain hardening in a dual-

- phase CrMnFeCoNi high-entropy alloy, *Nat. Commun.* 11 (2020) 1–8, <https://doi.org/10.1038/s41467-020-14641-1>.
- [301] T.L. Anderson, *Fracture Mechanics: Fundamentals and Applications*, Third, Taylor & Francis Group, 2005.
- [302] W. Li, P.K. Liaw, Y. Gao, Fracture resistance of high entropy alloys: a review, *Intermetallics* 99 (2018) 69–83, <https://doi.org/10.1016/j.intermet.2018.05.013>.
- [303] U. Roy, H. Roy, H. Daoud, U. Glatzel, K.K. Ray, Fracture toughness and fracture micromechanism in a cast AlCoCrCuFeNi high entropy alloy system, *Mater. Lett.* 132 (2014) 186–189, <https://doi.org/10.1016/j.matlet.2014.06.067>.
- [304] B. Gludovatz, A. Hohenwarter, K.V.S. Thurston, H. Bei, Z. Wu, E.P. George, R. O. Ritchie, Exceptional damage-tolerance of a medium-entropy alloy CrCoNi at cryogenic temperatures, *Nat. Commun.* 7 (2016) 10602, <https://doi.org/10.1038/ncomms10602>.
- [305] D. Li, Y. Zhang, The ultrahigh charpy impact toughness of forged AlxCrFeNi high entropy alloys at room and cryogenic temperatures, *Intermetallics* 70 (2016) 24–28, <https://doi.org/10.1016/j.intermet.2015.11.002>.
- [306] C. Chen, S. Pang, Y. Cheng, T. Zhang, Microstructure and mechanical properties of Al20-xCr20+0.5xFe20Co20Ni20+0.5x high entropy alloys, *J. Alloys Compd.* 659 (2016) 279–287, <https://doi.org/10.1016/j.jallcom.2015.10.258>.
- [307] N.J. Petch, The ductile-brittle transition in the fracture of α-iron: I, *Philos. Mag.* 3 (1958) 1089–1097, <https://doi.org/10.1080/14786435808237038>.
- [308] B. Tanguy, J. Besson, R. Piques, A. Pineau, Ductile to brittle transition of an A505 steel characterized by Charpy impact test, *Eng. Fract. Mech.* 72 (2005) 49–72, <https://doi.org/10.1016/j.engfractmech.2004.03.010>.
- [309] P.Y. Chen, C. Lee, S.Y. Wang, M. Seifi, J.J. Lewandowski, K.A. Dahmen, H.L. Jia, X. Xie, B.L. Chen, J.W. Yeh, C.W. Tsai, T. Yuan, P.K. Liaw, Fatigue behavior of high-entropy alloys: a review, *Sci. China Technol. Sci.* 61 (2018) 168–178, <https://doi.org/10.1007/s11431-017-9137-4>.
- [310] Z. Tang, T. Yuan, C.W. Tsai, J.W. Yeh, C.D. Lundin, P.K. Liaw, Fatigue behavior of a wrought Al0.5CoCrCuFeNi two-phase high-entropy alloy, *Acta Mater.* 99 (2015) 247–258, <https://doi.org/10.1016/j.actamat.2015.07.004>.
- [311] K.V.S. Thurston, B. Gludovatz, A. Hohenwarter, G. Laplanche, E.P. George, R. O. Ritchie, Effect of temperature on the fatigue-crack growth behavior of the high-entropy alloy CrMnFeCoNi, *Intermetallics* 88 (2017) 65–72, <https://doi.org/10.1016/j.intermet.2017.05.009>.
- [312] K. Liu, M. Komarasamy, B. Gwalani, S. Shukla, R.S. Mishra, Fatigue behavior of ultrafine grained triplex Al0.3CoCrFeNi high entropy alloy, *Scr. Mater.* 158 (2019) 116–120, <https://doi.org/10.1016/j.scriptamat.2018.08.048>.
- [313] M.Z. Ghomsheh, G. Khatibi, B. Weiss, M. Lederer, S. Schwarz, A. Steiger-Thirsfeld, M.A. Tikhonovsky, E.D. Tabachnikova, E. Schafer, High cycle fatigue deformation mechanisms of a single phase CrMnFeCoNi high entropy alloy, *Mater. Sci. Eng. A* 777 (2020), 139034, <https://doi.org/10.1016/j.msea.2020.139034>.
- [314] K. Liu, B. Gwalani, M. Komarasamy, S. Shukla, T. Wang, R.S. Mishra, Effect of nano-sized precipitates on the fatigue property of a lamellar structured high entropy alloy, *Mater. Sci. Eng. A* 760 (2019) 225–230, <https://doi.org/10.1016/j.msea.2019.06.012>.
- [315] S. Shukla, R.S. Mishra, Excellent high cyclic fatigue properties of a novel ultrafine-grained medium entropy alloy, *Mater. Sci. Eng. A* 779 (2020), 139122, <https://doi.org/10.1016/j.msea.2020.139122>.
- [316] D.H. Lee, M.Y. Seok, Y. Zhao, I.C. Choi, J. He, Z. Lu, J.Y. Suh, U. Ramamurthy, M. Kawasaki, T.G. Langdon, J. Il Jang, Spherical nanoindentation creep behavior of nanocrystalline and coarse-grained CoCrFeMnNi high-entropy alloys, *Acta Mater.* 109 (2016) 314–322, <https://doi.org/10.1016/j.actamat.2016.02.049>.
- [317] J.Y. He, C. Zhu, D.Q. Zhou, W.H. Liu, T.G. Nieh, Z.P. Lu, Steady state flow of the FeCoNiCrMn high entropy alloy at elevated temperatures, *Intermetallics* 55 (2014) 9–14, <https://doi.org/10.1016/j.intermet.2014.06.015>.
- [318] K.H. Lee, S.K. Hong, S.I. Hong, Precipitation and decomposition in CoCrFeMnNi high entropy alloy at intermediate temperatures under creep conditions, *Materialia* 8 (2019), <https://doi.org/10.1016/j.jmtla.2019.100445>.
- [319] Y. Bin Kang, S.H. Shim, K.H. Lee, S.I. Hong, Dislocation creep behavior of CoCrFeMnNi high entropy alloy at intermediate temperatures, *Mater. Res. Lett.* 6 (2018) 689–695, <https://doi.org/10.1080/21663831.2018.1543731>.
- [320] Z. Xu, H. Zhang, W. Li, A. Mao, L. Wang, G. Song, Y. He, Microstructure and nanoindentation creep behavior of CoCrFeMnNi high-entropy alloy fabricated by selective laser melting, *Addit. Manuf.* 28 (2019) 766–771, <https://doi.org/10.1016/j.addma.2019.06.012>.
- [321] Y. Ma, G.J. Peng, D.H. Wen, T.H. Zhang, Nanoindentation creep behavior in a CoCrFeCuNi high-entropy alloy film with two different structure states, *Mater. Sci. Eng. A* 621 (2015) 111–117, <https://doi.org/10.1016/j.msea.2014.10.065>.
- [322] H.T. Jeong, H.K. Park, H.S. Kang, W.J. Kim, Operation of solute-drag creep in an AlCoCrFeMnNi high-entropy alloy and enhanced hot workability, *J. Alloys Compd.* 824 (2020), 153829, <https://doi.org/10.1016/j.jallcom.2020.153829>.
- [323] S.G. Ma, Z.M. Jiao, J.W. Qiao, H.J. Yang, Y. Zhang, Z.H. Wang, Strain rate effects on the dynamic mechanical properties of the AlCrCuFeNi₂ high-entropy alloy, *Mater. Sci. Eng. A* 649 (2016) 35–38, <https://doi.org/10.1016/j.msea.2015.09.089>.
- [324] C.M. Cao, J. Xu, W. Tong, Y.X. Hao, P. Gu, L.M. Peng, Creep behaviour and microstructural evolution of AlxCrMnFeCoNi high-entropy alloys, *Mater. Sci. Technol. (United Kingdom)* 35 (2019) 1283–1290, <https://doi.org/10.1080/02670836.2019.1619306>.
- [325] T. Cao, J. Shang, J. Zhao, C. Cheng, R. Wang, H. Wang, The influence of Al elements on the structure and the creep behavior of Al_xCr_yFe_zNi high entropy alloys, *Mater. Lett.* 164 (2016) 344–347, <https://doi.org/10.1016/j.matlet.2015.11.016>.
- [326] L. Zhang, P. Yu, H. Cheng, H. Zhang, H. Diao, Y. Shi, B. Chen, P. Chen, R. Feng, J. Bai, Q. Jing, M. Ma, P.K. Liaw, G. Li, R. Liu, Nanoindentation creep behavior of an Al0.3CoCrFeNi high-entropy alloy, *Metall. Mater. Trans. A* 47 (2016) 5871–5875, <https://doi.org/10.1007/s11661-016-3469-8>.
- [327] S. Chen, W. Li, X. Xie, J. Brecht, B. Chen, P. Li, G. Zhao, F. Yang, J. Qiao, P. K. Liaw, Nanoscale serration and creep characteristics of Al0.5CoCrCuFeNi high-entropy alloys, *J. Alloys Compd.* 752 (2018) 464–475, <https://doi.org/10.1016/j.jallcom.2018.04.137>.
- [328] N. Larianovsky, A. Katz-Demyanetz, E. Eshed, M. Regev, Microstructure, tensile and creep properties of Ta20Nb20Hf20Zr20Ti20 high entropy alloy, *Materials (Basel)* 10 (2017) 883, <https://doi.org/10.3390/ma10080883>.
- [329] P. Kral, W. Blum, J. Dvorak, N. Yurchenko, N. Stepanov, S. Zherebtsov, L. Kuncicka, M. Kvapilova, V. Sklenicka, Creep behavior of an AlTiVNbZr0.25 high entropy alloy at 1073 K, *Mater. Sci. Eng. A* 783 (2020), 139291, <https://doi.org/10.1016/j.msea.2020.139291>.
- [330] W. Li, G. Wang, S. Wu, P.K. Liaw, Creep, fatigue, and fracture behavior of high-entropy alloys, *J. Mater. Res.* 33 (2018) 3011–3034, <https://doi.org/10.1557/jmr.2018.191>.
- [331] P.H. Lin, H.S. Chou, J.C. Huang, W.S. Chuang, J.S.C. Jang, T.G. Nieh, Elevated-temperature creep of high-entropy alloys via nanoindentation, *MRS Bull.* 44 (2019) 860–866, <https://doi.org/10.1557/mrs.2019.258>.
- [332] A.H. Chokshi, High temperature deformation in fine grained high entropy alloys, *Mater. Chem. Phys.* 210 (2018) 152–161, <https://doi.org/10.1016/j.matchemphys.2017.07.079>.
- [333] S. Sun, P. Gao, G. Sun, Z. Cai, J. Hu, S. Han, J. Lian, X. Liao, Nanostructuring as a route to achieve ultra-strong high- and medium-entropy alloys with high creep resistance, *J. Alloys Compd.* 830 (2020), 154656, <https://doi.org/10.1016/j.jallcom.2020.154656>.
- [334] T.K. Tsao, A.C. Yeh, C.M. Kuo, K. Kakehi, H. Murakami, J.W. Yeh, S.R. Jian, The high temperature tensile and creep behaviors of high entropy superalloy, *Sci. Rep.* 7 (2017) 1–9, <https://doi.org/10.1038/s41598-017-13026-7>.
- [335] N. Kumar, R.S. Mishra, C.S. Huskamp, K.K. Sankaran, Critical grain size for change in deformation behavior in ultrafine grained Al–Mg–Sc alloy, *Scr. Mater.* 64 (2011) 576–579, <https://doi.org/10.1016/j.scriptamat.2010.11.051>.
- [336] S.K. Panigrahi, K. Kumar, N. Kumar, W. Yuan, R.S. Mishra, R. DeLorme, B. Davis, R.A. Howell, K. Cho, Transition of deformation behavior in an ultrafine grained magnesium alloy, *Mater. Sci. Eng. A* 549 (2012) 123–127, <https://doi.org/10.1016/j.msea.2012.04.017>.
- [337] S.K. Panigrahi, R.S. Mishra, R.C. Brennan, K. Cho, Achieving extraordinary structural efficiency in a wrought magnesium rare earth alloy, *Mater. Res. Lett.* 8 (2020) 151–157, <https://doi.org/10.1080/21663831.2020.1719227>.
- [338] T.S. Byun, On the stress dependence of partial dislocation separation and deformation microstructure in austenitic stainless steels, *Acta Mater.* 51 (2003) 3063–3071, [https://doi.org/10.1016/S1359-6454\(03\)00117-4](https://doi.org/10.1016/S1359-6454(03)00117-4).
- [339] W.G. Burgers, On the process of transition of the cubic-body-centered modification into the hexagonal-close-packed modification of zirconium, *Physica* 1 (1934) 561–586, [https://doi.org/10.1016/S0031-8914\(34\)80244-3](https://doi.org/10.1016/S0031-8914(34)80244-3).
- [340] C. Cayron, Angular distortive matrices of phase transitions in the fcc–bcc–hcp system, *Acta Mater.* 111 (2016) 417–441, <https://doi.org/10.1016/j.actamat.2016.01.075>.
- [341] P. Agrawal, S. Shukla, S. Gupta, P. Agrawal, R.S. Mishra, Friction stir gradient alloying: a high-throughput method to explore the influence of V in enabling HCP to BCC transformation in a γ-FCC dominated high entropy alloy, *Appl. Mater. Today.* 21 (2020), 100853, <https://doi.org/10.1016/j.apmt.2020.100853>.
- [342] M. Wang, Z. Li, D. Raabe, In-situ SEM observation of phase transformation and twinning mechanisms in an interstitial high-entropy alloy, *Acta Mater.* 147 (2018) 236–246, <https://doi.org/10.1016/j.actamat.2018.01.036>.
- [343] T. Zhang, R.D. Zhao, F.F. Wu, S.B. Lin, S.S. Jiang, Y.J. Huang, S.H. Chen, J. Eckert, Transformation-enhanced strength and ductility in a FeCoCrNiMn dual phase high-entropy alloy, *Mater. Sci. Eng. A* 780 (2020), <https://doi.org/10.1016/j.msea.2020.139182>.
- [344] Y.H. Jo, W.M. Choi, D.G. Kim, A. Zargaran, S.S. Sohn, H.S. Kim, B.J. Lee, N. J. Kim, S. Lee, FCC to BCC transformation-induced plasticity based on thermodynamic phase stability in novel V 10 Cr 10 Fe 45 Co x Ni 35–x medium-entropy alloys, *Sci. Rep.* 9 (2019) 1–14, <https://doi.org/10.1038/s41598-019-39570-y>.
- [345] J.W. Bae, J.B. Seol, J. Moon, S.S. Sohn, M.J. Jang, H.Y. Um, B.J. Lee, H.S. Kim, Exceptional phase-transformation strengthening of ferrous medium-entropy alloys at cryogenic temperatures, *Acta Mater.* 161 (2018) 388–399, <https://doi.org/10.1016/j.actamat.2018.09.057>.
- [346] D. Wei, X. Li, J. Jiang, W. Heng, Y. Koizumi, W.M. Choi, B.J. Lee, H.S. Kim, H. Kato, A. Chiba, Novel Co-rich high performance twinning-induced plasticity (TWIP) and transformation-induced plasticity (TRIP) high-entropy alloys, *Scr. Mater.* 165 (2019) 39–43, <https://doi.org/10.1016/j.scriptamat.2019.02.018>.